NTNU

Norwegian University of
Science and Technology

Design, Fabrication and Testing of Micro-Nanoscale Thin-Film Resistance Temperature Detectors

Christian Georg Bauge Gulliksen

Master of Science in Mechanical Engineering
Submission date: July 2017
Supervisor: Carlos Alberto Dorao, EPT

Norwegian University of Science and Technology
Department of Energy and Process Engineering

NTNU
Norwegian University
of Science and Technology

Department of Energy
and Process Engineering

EPT-M-2017- 27

MASTER THESIS

For Christian Georg Bauge Gulliksen

Spring 2017

Design of Micro- Nanoscale Thin-Film Restistance Temperature Sensors.

Design av Temperatursensorer på Mikro- og Nanoskala, Basert på Elektrisk Motstand i Tynne Metalliske Filmer.

The need for high heat flux removal has been triggered by the development of new technologies ranging from computers, data centers, medical applications, electric cars, radars, satellite and lasers, to mention some applications. Today it is recognized that manufacturability is not the limiting factor with regards to the small size of the devices, and that the major challenge is the power dissipation problem, i.e. how to remove the heat from a confined space. A particular alternative is to modify the surface for enhancing heat transfer. However in order to quantify heat transfer at the small scale requires to develop new sensors in the order microns in size capable of measuring heat fluxes with high accuracy and fast response.

The main objective in this work is to design and test RTD sensors in the order of microns for measuring heat transfer.

The following tasks are to be considered:

1. Literature study on RTD sensors
2. Analysis of RTD sensors, and evaluation of alternative designs
3. Identify the procedure for fabrication
4. Suggest suggestions for RTD sensors

-- ” --

Within 14 days of receiving the written text on the master thesis, the candidate shall submit a research plan for his project to the department.

When the thesis is evaluated, emphasis is put on processing of the results, and that they are presented in tabular and/or graphic form in a clear manner, and that they are analyzed carefully.

The thesis should be formulated as a research report with summary both in English and Norwegian, conclusion, literature references, table of contents etc. During the preparation of the text, the candidate should make an effort to produce a well-structured and easily readable report.

In order to ease the evaluation of the thesis, it is important that the cross-references are correct. In the making of the report, strong emphasis should be placed on both a thorough discussion of the results and an orderly presentation.

The candidate is requested to initiate and keep close contact with his/her academic supervisor(s) throughout the working period. The candidate must follow the rules and regulations of NTNU as well as passive directions given by the Department of Energy and Process Engineering.

Risk assessment of the candidate's work shall be carried out according to the department's procedures. The risk assessment must be documented and included as part of the final report. Events related to the candidate's work adversely affecting the health, safety or security, must be documented and included as part of the final report. If the documentation on risk assessment represents a large number of pages, the full version is to be submitted electronically to the supervisor and an excerpt is included in the report.

Pursuant to "Regulations concerning the supplementary provisions to the technology study program/Master of Science" at NTNU §20, the Department reserves the permission to utilize all the results and data for teaching and research purposes as well as in future publications.

The final report is to be submitted digitally in DAIM. An executive summary of the thesis including title, student's name, supervisor's name, year, department name, and NTNU's logo and name, shall be submitted to the department as a separate pdf file. Based on an agreement with the supervisor, the final report and other material and documents may be given to the supervisor in digital format.

X Work to be done in lab (Water power lab, Fluids engineering lab, Thermal engineering lab)
☐ Field work

Department of Energy and Process Engineering, 13. January 2017

Carlos A. Dorao
Academic Supervisor

Research Advisor:
Espen Rogstad

There is nothing new to be discovered in physics now.
All that remains is more and more precise measurements.

Lord Kelvin

Acknowledgement

I am a true believer in the power of gratefulness, and so particular attention has been devoted to this part of the thesis. I hope that the people who inevitably will go unacknowledged, as I am writing this at 2:00 AM in the morning, will find that the appreciation towards all who are mentioned here will echo in your directions as well.

First of all, I would like to thank my supervisor, Professor Carlos Alberto Dorao, for giving me the opportunity to work in the exciting field of two-phase flow heat transfer, and for encouraging me to follow my curiosity and letting me form my own assignment. It has been an experience I will never forget.

Special attention is attributed to Ph.D. candidate Espen Rogstad who has served as my laboratory supervisor and research advisor through this entire process. You have been truly wonderful in providing answers when I had questions, instructions when I needed guidance, and ultimately portraying an enormous amount of patience in doing so, as I know I can be a handful. For this, I am forever grateful, and I wish you the best of luck in future endeavors.

The same goes to all of the fantastic people at the NTNU Nanolab that makes the cleanroom environment a great place to work. Mark Chiappa, Jakob Vinje, Svenn Ove Linde, Manuel Auliano, Verner Håkonsen, Jens Høvik, Einar Digernes and Carl Phillip Heimdal – thank you for sharing your knowledge and teachings, and for guiding me along the way. For making all of this possible, the Research Council of Norway is acknowledged for the support to the Norwegian Micro- and Nano-Fabrication Facility, NorFab, project number 245963/F50.

I would also like to thank my friend, and truly one of the best people I know, Håvard Dybvik, for setting up an "off the charts" Latex environment that has made the technical aspects of writing incredibly easy and fun. Also thanks to Thea Karlsen Løken, Research Assistant at the Hydro Power Laboratories, for providing me with a workstation at the best student hall in all of NTNU.

This work would not have been possible without the encouragement and support from the wonderful people I am blessed to have in my life. My mom, dad, and sister have been of enormous support, not just throughout this thesis, but for my entire studies. I can't even begin to describe how much your encouragement has done for me. All the phone calls and countless textmessages wishing me good luck on my exams, including my mothers "good vibrations sent from Oslo" which has become somewhat of a classic.

I can't wait to spend the summer with you guys. From the bottom of my heart, to all the people who do great work and enrich the lives to the people around them – thank you!

C.G.

Preface

This thesis has been conducted at the Department of Energy and Process Engineering during the spring of 2017 for earning my degree as Master of Science in mechanical engineering from the Norwegian University of Science and Technology. My supervisor during this work has been Professor Carlos A. Dorao, and my laboratory supervisors and research advisors have been Ph.D. candidates Espen Rogstad, Manuel Auliano and Il-Woong Park.

The topic of this thesis is an experimental study of design and fabrication of the worlds smallest resistance temperature detectors with the goal of using them to obtain local temperature and heat-flux recordings in two-phase flow boiling microchannel heat sink research. The aim of this research is to gain knowledge and insight into the fundamental aspects of heat transfer which will enable commercial realization of these devices, e.g. for the cooling of CPU chips.

Trondheim, 03.07.2017

Christian Georg Bauge Gulliksen
christianbgulliksen@gmail.com

Abstract

The development of the microelectronics industry has triggered a broad scientific revolution. The ever ongoing quest for miniaturization and the thermal challenges that follow have made heat transfer in confined spaces one of the most researched topics in recent time. The increasingly compact devices encountered in everyday life have motivated the need for new and efficient cooling techniques for the removal of the high heat duties produced by these systems. The two-phase flow boiling microchannel heat sink is recognized as one of the top candidates for such a task, with its promise of high heat removal capabilities through its latent heat of evaporation and favorable pressure drop with respect to its single-phase counterpart. However, the research is still in its infancy stage, requiring knowledge and insight in the fundamental mechanisms involved, as the conventional continuity assumptions valid in the macro-world may not be applicable on these smaller scales, as the contradicting results of previous studies indicate. The main causes of these dispersions are believed to be related to the intrusive nature of the metrology devices used in the research, which disturbe the flow field and yield false values. The research community is in high demand of benchmark data on localized measurements regarding both temperature and heat-flux. In this work, novel platinum thin-film resistance temperature detectors with high sensitivity are produced to meet this high demand. Four size variations of the sensors are successfully obtained, i.e. 3 μm^2, $4\mu m^2$, $5\mu m^2$, and $6\mu m^2$, with corresponding wire tracks of 60 nm, $80nm$, $100nm$, and $120nm$, respectively, and a thin-film thickness of 40 nm. Measurements show that the mean sheet resistances of these sensors exceed that of previous results found in the literature by approximately 200 Ω at a size several orders of magnitude lower. To the author's knowledge, the RTD's produced in this work are the smallest ever made.

Sammendrag

Utviklingen innen mikroelektronikkindustrien de siste årene har utløst en bred vitenskapelig revolusjon. Den stadig pågående søken etter minatyrisering og de termiske utfordringer som medfølger har gjort varmeoverføring i begrensede områder til et av de mest utforskede emner i nyere tid. Den stadig økende grad av kompakte enheter som møtes i det daglige liv har motivert behovet for nye, effektive kjølemetoder for fjerning av de store varmetapene disse systemene genererer. To-fase strømning i mikrokanaler med inkorporert koking er anerkjent som en av de mest lovende teknikker for denne oppgaven, med løfte om veldig høy varmefjerningskapasitet gjennom sin latente fordampningsenergi og gunstig trykkfall sammenliknet med mikrokanaler med kun én fase. Likevel er forskningen kun i spedbarnsfase, og kravet om kunnskap og innsikt i de fundamentale mekanismer innvolvert er enormt etterspurt. Forskningen fram til nå har produsert motsigende resultater, og de konvensjonelle kontinuitetsantakelsene, gyldig i makro-verdenen, bryter tilsynelatende sammen når de karakteristiske lengdeskalaene blir tilstrekkelig lave. Hovedårsaken for disse observasjonene er begrunnet å være relatert til de påtrengende egenskapene ved måleverktøyene brukt tidligere, som er antatt å forstyrre strømningsfeltet og dermed ha generert gale verdier. Lokale måledata av både temperaturfelt og varmegjennomstrømning er enormt etterspurt i forskermiljøet. Denne oppgaven beskriver produskjonen av sensorer basert på elektrisk motstand i tynne metalliske platina-filmer, med høy sensitivitet, for å møte denne etterspørselen. Fire vellykede størrelsesvariasjoner er presentert, hhv. 3 μm^2, 4μm^2, 5μm^2, and 6μm^2 store, bestående av 60 nm, 80nm, 100nm, og 120nm ledninger, og en filmtykkelse på 40 nm. Målinger av disse viser at den elektriske motstanden overgår tidligere resulteter funnet i litteraturen med omtrent 200 Ω, på flere størrelseordener lavere skala. Til forfatterens kunnskap er disse RTD'ene de minste som noensinne er produsert.

Contents

List of Figures

List of Tables

Part I

Background and Theory

Chapter 1

Introduction

1.1 More Moore!

In 1965, Gordon E. Moore published his iconic article; *Cramming More Components Onto Integrated Circuits*. In the article, Moore predicted that the future of the electronics industry were to be driven by the evolution of the integrated circuits industry (IC) itself, and as a result of this development he described new technologies, that at the time would seem a bit far-fetched, but today we take for granted. As Moore writes [32]: *"Integrated circuits will lead to such wonders as home computers - or at least terminals connected to a central computer - automatic controls for automobiles, and personal portable communications equipment"*. His vision is truly remarkable, looking back, concidering the power and presence of today's smart phones, and the emmergence of autonomous cars as a near future reality.

The main aspect people took away from his article, was the trend now known as *Moores's Law*, which states that the number of transistors on a microprocessor chip will double for every new generation, generally resulting in doubling the computing power [55]. For nearly three decades the development has accurately followed the predictions of Moore, elevating the law beyond the status as observational trend, into a self fulfilling prophecy, or "techno-mantra" [45]. However, this has not been by chance. Chipmakers deliberately chose to stay on the Moore's law track through a strategy often called "More Moore" [55], where the seminconductor industry, every two years since the 1990s, have released a resarch road map to coordinate what its hundreds of manufacturers are doing in order to keep up with the ever increasing demand for faster microprocessor chips. From 1971 to 2006, the number

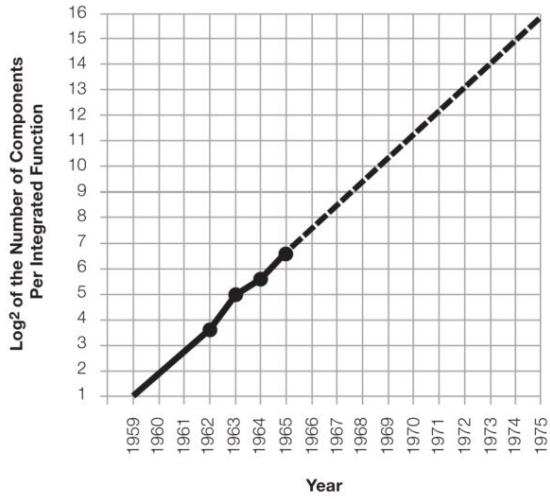

Figure 1.1: Original revision of Moore's law from his 1965 article [32], by simple extrapolation of current industry observations.

of transistors on commercially available single core chips increased from 2300 in Intels 4004, to 188 million in Intel Pentium 4 HT 661, yielding a development in clock speed from 740kHz to 3.6GHz, respectively [1, 7, 9]. Since then, the clock speed of single core units haven't increased at all due to the thermal challenges that have arised, caused by the physical size, and density distributions, of the transistors. To keep up with the demand, and increasing the computational power, the innovation that was introduced has been a complete redesign of the IC, so that each chip contained multiple processors, or *cores*. Principally, four 250MHz cores will generate the same computing output as a single 1GHz unit. This implies that the problem at hand needs to be broken down into several components, and solved through the use of parallell programming, which for complex algorithms is difficult, if not impossible [45]. To cope with the development, and aleviating the heat duties produced by ever more compact components, several cooling techniques have been suggested. One of the most promissing techniques is the *Microchannel Heat Sink*, introduced in 1981 by Tuckerman and Pease [54], who first realized that the microscopic size of the channel causes a decrease in the thermal boundary layer, resulting in a decrease in convective resistance to heat transfer, generating high cooling rates [54, 21]. However, the commercial applications of such channels requires fundamental understanding of the heat transfer processes involved in these

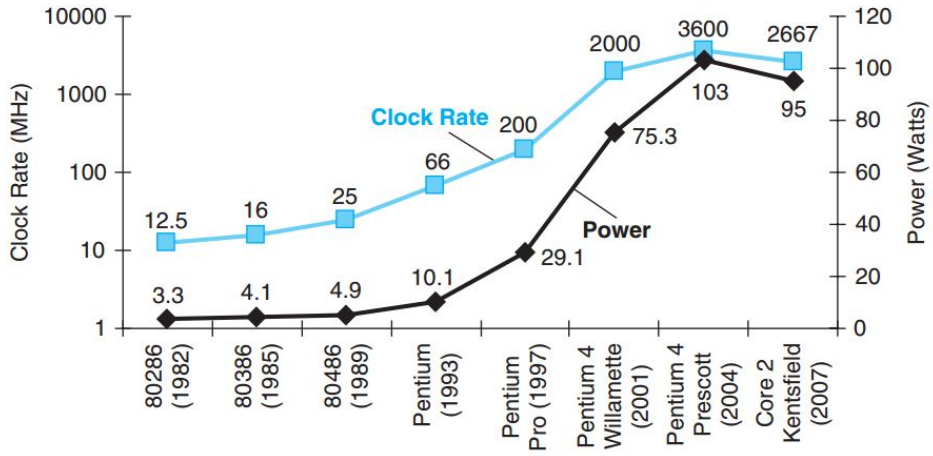

Figure 1.2: Development of processor clock rates and power consumption [5].

channels, and for this, benchmark data on localized temperature and heat-flux distributions are in high demand.

1.2 Problem Formulation

Today it is recognized that manufacturability is not the limiting factor with regards to the small size of the devices, and that the major challenge is the power dissipation problem, i.e. how to remove the heat from a confined space. A particular alternative is to modify the surface for enhancing heat transfer, or deploying microchannel heat sinks. However in order to quantify heat transfer at the small scale requires to develop new sensors in the order microns in size capable of measuring heat fluxes with high accuracy and fast response. This work aims at investigating the fabricational limits to temperature sensors utilizing the change in electrical resistance to a change in temperature, known as Resistance Temperature Detectors (RTD's), for the potential use in heat transfer research in confined spaces.

1.2.1 Goal and Objective

The long term goal in the field of research is to fabricate temperature sensors that may describe local temperature and heat flux distributions within microchannels and on micro-/nano engineered surfaces, in order for commercial realization.

The short term objective of this thesis is (I) to investigate the manufacturability

of microscale RTD's in the range of 1 μm^2 to 6 μm^2, as a potential candidate for such a task, using selected fabrication methods availiable at the NTNU Nanolab and (II) develop a scheme and guidlines for the fabrication process of RTD's. Objective (I) is solved by completing required training to operate relevant machinery used in nanofabrication and attempting to fabricate RTD's by an iterative approach combined with reviewing the literature and applying the gained knowledge in each iteration. Objective (II) is solved by experience and "Lessons Learned".

1.2.2 Scope of Work

The scope of the work is limited to RTD's using silicon as the substrate material, Electron Beam Lithography as patterning technique and Electrom Beam Thin-Film Evaporation as deposition of the thin metal films. Other temperature measurement techniques, such as Diode Temperature Sensors (DTS), utilizing the temperature dependent voltage drop across diodes, are not concidered.

1.2.3 Structure

This thesis is comprised of three parts; (I) Background and Theory, (II) Present Work and (III) Results and Discussions. Part I consists of chapters 1, 2, 3 and 4, Part II of chapters 5, 6 and 7, and Part III of chapters 8 and 9. In Chapter 2 a state of the art review of the current measurment techniques related to microchannel heat sink research is presented. Chapter 3 introduces the Resistance Temperature Detector and Chapter 4 presents fundamental aspects of sensor characteristics. In Chapter 5 the material and experimental methods used in the fabrication of the sensors is explained in detail. The design and layout of the temperature detectors is found in Chapter 6, and the fabrication procedure is outlined and discussed in Chapter 7. Finally, the results and discussions are presented in Chapter 8 with concluding remark following in chapter 9.

Chapter 2

State of the Art

Microchannel Heat Sinks (MHS) promises extremely high heat dissipating capabilities with the decrease in hydraulic diameter, D_h. Two-phase flow boiling microchannels, especially, are widely viewed in favor of their single-phase counterparts due to their increased heat carrying capabilities through the latent heat of evaporation and favorable pressure drop. However, the commercial application of these devices requires fundamental understanding of the mechanisms involved in the heat transfer process. Specifically, flow instabilities, vapor back flow and flow maldistribution and its impact need to be fully understood before implementation onto IC chips or lases diodes can be realized. Today it is recognized that the main dispersion between the contradicting results in this field of research is caused by measurement errors and estimating the parameters gouverning the convective heat transfer equations [31**?**]. In this chapter a state of the art literature review on the techniques and difficulties relating to localized measurement of temperature and heat flux is presented. The thin-film technology is identified as the most promising technique for these measurements, and a literature review on resistance temperature detectors are included. Finally, the review is summarized and discussed, and the focus of this thesis is identified with main goal and objectives, scope of work and structure of this thesis.

2.1 Motivation of the Microchannel Heat Sink

Heat transfer between fluids and solid surfaces are in general dominated by *convection*, i.e. the combination of heat transfer by bulk fluid motion, and conduction in the vicinity of the fluid–solid interphase. Convection heat transfer problems are described by Newton's Law of Cooling, as [22]

$$q = hA_s(T_w - T_{m,\infty}) \tag{2.1}$$

where h is the convection heat transfer coefficient $(W/m^2 \cdot K)$, A_s is the surface area in contact with the fluid (m^2) and $(T_w - T_{m,\infty})$ is the difference between the wall surface and mean fluid temperatures, respectively (K). The deveolpment of the early 19^{th} and 20^{th} centuries focused on increasing the overall heat transfer by maximizing the surface area, A_s, in contact with the fluid, giving rise to *shell and core* heat exchangers, which would, on the extremities, rival the size of a small family home on a single unit basis [25].

The main challenge in convection heat transfer problems is to determine the value of h, for then to revisit the basic equation (2.1) for the heat transfer evaluation. In internal flow heat transfer problems, i.e. pipes and channels,the heat transfer coefficient is determined through a dimensionless temperature gradient termed the *Nusselt number*, defined as [22]

$$Nu = \frac{hD_h}{k_f} \tag{2.2}$$

where D_h is the hydraulic diameter of the channel, and k_f is the thermal conductivity of the fluid $(W/m \cdot K)$. The Nusselt number in fully developed laminar flow in a square channel with uniform heat flux or constant surface temperature is constant and found to be 3.61 and 2.98, respectively.

Investigating and rearranging the terms of Equation (2.2), the decrease in D_h indeed promisses incresing values of the convective heat tranfer coefficient, as

$$h = \frac{Nuk_f}{D_h}. \tag{2.3}$$

This may seem counter intuitive. However, the rate of the transport process depends on the surface area, which varies with the diameter D for a circular tube, whereas the flow rate depends on the cross-sectional area, which varies linearly with D^2, and thus, the surface area to volume ratio increases as as the diameter of the channel decreases, according to $1/D$ [24]. Figure (2.1) displays these drastic enhancements in the heat transfer coefficient and pressure gradient with

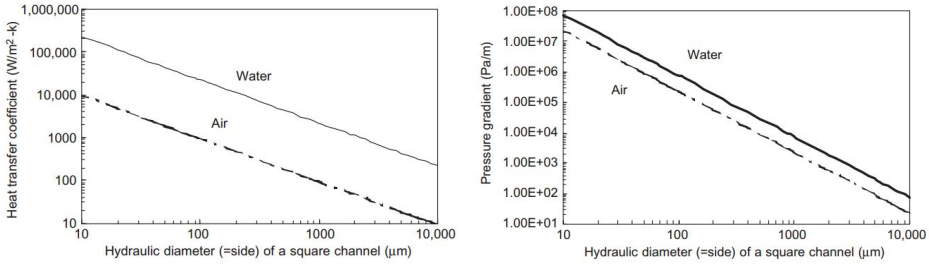

(a) **(b)**

Figure 2.1: Illustrative representations of the heat transfer coefficient, h and pressure gradient per unit length $\Delta p/L$ for variations in hydraulic diameter of channels with fully developed laminar flow of air and water [24].

the decreasing size of the channel, spanning several orders of magnitude in both axes. The characteristic length of the channel is aknowledged for this change and in order to compare research, trends and flow patterns the channels need to be classified. Several classification schemes exist. However, Kandlikar [25] defines a microchannel with having a hydraulic diameter from $10\mu m < D_h \leq 200\mu m$, and is widely adopted in the literature.

2.2 MCHS Measurement Techniques

Deployment of two-phase microcahnel heat sinks requires a comprehensive fundamental understanding of virtually all hydrodynamic and thermal aspects of phase change in small channels and the ability to accurately predict pressure-drop and flow boiling heat transfer for a given channel geometry and operating conditions is of paramount importance [40]. For this knowledge to be gained, accurate measurements of the local temperature and heat-flux distributions is required. Several measurement approaches exist, for example, Szczukiewicz et al. [49] used a high-speed infra-red (IR) camera to simoultaniously visualise the two-phase diabetic flow and heat transfer dynamics in a silicon multi-microchannel, and 90 local heat transfer coefficients were reported from inlet to outlet of the 100 $\times$ 100 μm^2 microchannel. A similar technique was reported by Xu et al. [58] who investigated the cooling applications of microchannels on a silicon chip and obtaining the local chip temperature and Nusselt number by deploying a high-resolution Infrared Radiator Imaging (IRI) system. While the use of optical systems for local measurements might be fine in single-phase microchannels, flow-boiling regimes are characterized

by the presence of bubbles which may deteriorate the view of the metrology device. In addition, the spatial resolution is limited to the working wavelength of the IR camera. In the work of Xu et al. the camera used was a ThermaCAM SC3000 with a GaAs Quantum Well Infrared Photon FPA detector with a reported spatial resolution of 8-9 μm. However, the camera needs to be callibrated, and the callibration scheme deployed by Xu et al. yielded a higher spatial resolution than advertised by the manufacturer, i.e. 17.5 μm. The measured surface temperature using IR cameras are also strongly dependent on the surface emmissivity [58] and the use of these devices for obtaining local information in the temperature field deserve special attention for proper function and useful information to be obtained. However, if bubbles are present, other approaches should be investigated.

Mokrani et al. [31] stated that the local wall temperature inside a microchannel cannot be measured directly and that they may only be estimated from temperature detectors inside of the wall through an inverse heat conduction method. In this study, three K-type thermocoulpes were placed inside the microchannel wall. Similar techniques were used by Qu et al. and Wang et al. [40, 56] who deployed 4 and 5 thermocouples, respectively, beneath selected points of the microchannel bed.

2.3 Thin-Film Technology

Thin-film technology has been recognized a favorable technology for local temperature and heat-flux measurements. The metallic films may be mounted directly onto the microchannel bed and their locations are accurately obtained as they are generally designed on a computer. In the forthcoming papers, RTD's in various applications is presented. The author has focused on extracting data relating to the RTD's themselves, who in most of the presented cases were not the main focus of the research. Substrate, resistive element, size, thickness, width and length are extracted where the data was available and summarized in Table (2.1).

Author	Substrate	Resistor	Size	Thickness	Width	Length
Andretta et al.	Plexiglass	Copper	-	50 μm	50 μm	40 mm
Epstein et al.	Kapton	Nickel	1.3 mm^2	150 nm	25 μm	20 mm
Guo et al.	Upilex	Platinum	10 mm^2	4 nm	1mm	10 mm
Rule and Kim	Quarz	Platinum	-	200 nm	5 μm	-
Piccini et al.	Upilex-s	Platinum	-	100 nm	-	-
Kim et al.	Alumina	Platinum	$\approx$ 122 mm^2	105 nm, 206 nm	0.1 - 0.4 mm	-
Myers et al.	Silicon	Platinum	0.01 mm^2	400 nm	2 m	-
Moghaddam et al.	Silicon	Nickel	0.00196 mm^2	12 nm	$\approx$ 6 μm	-
Kumar et al.	Pyrex	Platinum Ink	-	a few μm	-	-
Azerou et al.	Polymide	Copper	0.6 mm^2	9 μm	30 μm	20 mm
Hamadi et al.	Borosilicate	Gold	0.1 mm^2	85 nm	50 μm	2 mm
Ammar et al.	Borosilicate	Gold	0.0045 mm^2	85 nm	30 μm	150 μm
Zribi et al.	Borofloat 33	Platinum	3.92 mm^2	200 nm	60 μm	45.66 mm

Table 2.1: Previous work found in the literature. Substrate, Resistive Material, Size, thickness (t), width (w) and length (l).

2.3.1 Previous Work: RTD's in MCHS Applications

Hamadi et al. [20] recognized that the understanding of microcale heat transfer phenomena required highly precise and minimally intrusive temperature and heat-flux measurements on the microchannel heat sink wall. For the purpose of obtaining such local measurements, novel thin-film microsensors were developed. The design consisted of 40 thin-film resistance temperature detectors distributed evenly along the bed of a rectangular shaped, 40 mm long, 4 mm wide, and 25.4 μm high microchannel, yielding a hydraulic diameter of 50.48 μm. Three of the walls were fabricated with poly-dimethylsiloxane and the fourth wall was a borosilicate substrate containing the temperature- and heat-flux detectors. The temperature sensors were deposited on both sides of the 1.1 mm thick substrate and the heat-flux measurement was obtained by using the temperature recordings on each side

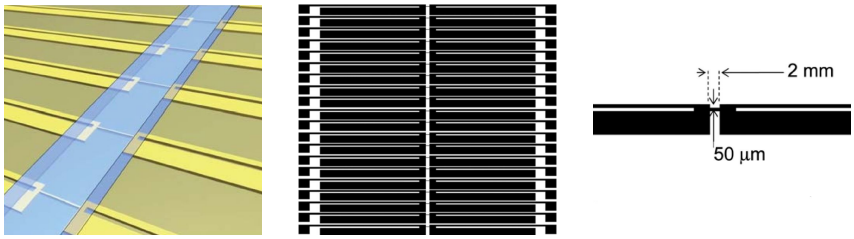

(a) **(b)** **(c)**

Figure 2.2: RTD design and implementation with the microchannel heat sink in the works of Hamadi et al. [20].

as boundary conditions for the conduction through the borosilicate material, conventionally solved through the use of Fourier's law of conduction.

The fabrication process was briefly explained with no reference to earlier, more comprehensive work. The borosilicate substrate was exposed to Chromium (Cr) vapor to create a 5 nm thick film for adhesion purposes. The thin-film resistors were constructed in a similar fashion. Gold (Au) was vapor deposited on top of the Cr until an 85 nm thick film was obtained. A positive tone photosensitive resist was then spin-coated and exposed through a mask containing the sensor pattern. The exposed portions of the resist were then dissolved through a development stage, after which the unwanted gold–chromium areas were chemically removed through an etching procedure. Lastly, the remaining resist was stripped from the surface.

Figure (2.2) illustrates the implementation of the microsensors with the microchannel heat sink (**??**) and the details of the sensor distribution (**??**) and the single sensor units (2.2c). The 40 central elements were characterized to have an average electric resistance of 16.2 Ω with a relative standard deviation of 12 %. Similarly, the connection prongs had an average resistance of 4.0 Ω and 20 % standard deviation.

Based on the work of Hamadi et al. (2012), Ammar et al. (2013) developed a similar temperature and heat-flux sensor. 85 nm thick gold thin films were deposited on a borosilicate substrate, measuring 30 μm wide and 50 μm long. [11]

2.3.2 Previous Work: RTD's in Nucleate Boiling Experiments

Rule and Kim (1999) developed an array of 96 thin-film temperature controlled resistance heaters for studying the local heat flux during pool boiling experiments of FC-72 at constant surface temperature. Platinum was sputtered onto a 500 μm thick quartz substrate to a thickness of 0.2 μm, with line widths and spacing between the lines, both equal to 5 μm. The spacing between the heaters varied with position, from about 7 μm at center locations to about 40 μm near the edges of the array [44].

Myers et al. (2005) extended the work done by Rule and Kim (1999) on nucleate boiling of FC-72 at constant surface temperature, to nucleate boiling of FC-72 at constant wall heat flux. A similar thin-film heater array was fabricated for this purpose. 96 heaters were patterned using photolithography, and an ion mill was used to form the individual heaters followed by a plasma ash. The resistive element was a 400 nm thick layer of platinum, with a 30 nm thick titanium layer underneath for adhesion purposes, deposited on a 500 μm thick silica substrate. The platinum lines were 2 μm wide and spaced 2 μm apart. 1 μm thick gold lead wires were used to power the heaters. Each heater exhibited a nominal resistance of 6 kΩ and a temperature coefficient of resistance (TCR) of 0.0019 $^{\circ}C^{-1}$. [33]

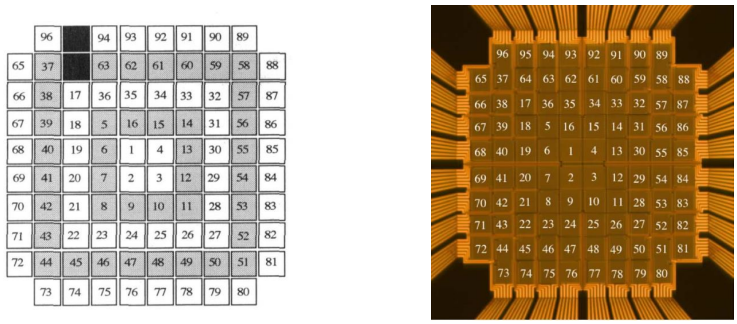

(a) **(b)**

Figure 2.3: Results from Rule adn Kim, and Myers et al. (a) Arrangement of 96 heaters in the array, with nonfunctional heaters represented by the black squares [44] (b) Photograph of heater array indicating the heater numbering. Each heater in the array is nominally 100 microns in size. [33].

Moghaddam et al. (2006) fabricated an artificial nucleation site in the center of an array of radially distributed RTD's in order to measure the temperature and heat flux underneath a bubble from initial formation through growth and eventually departure. The sensor consisted of a composite wall with embedded sensors and heaters. Only the the temperature sensors on top are presented here. The array consisted of 44 radially distributed, 12 nm thick Nickel resistors on a silicon substrate. A 3 nm thick layer of chromium was used for adhesion purposes. The Nickel wires were 6 μm wide, and the length varied depending on the sensors position. 200 nm gold lead wires were used for powering the sensors. [29]

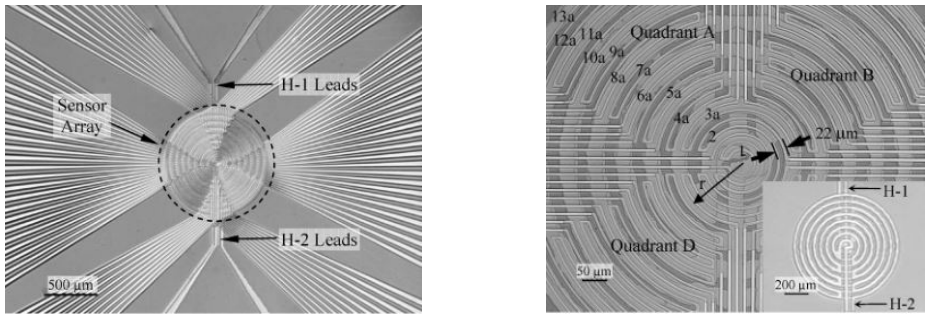

(a) **(b)**

Figure 2.4: Results from Moghaddam (a) Wide view of device showing sensor array leads and two pairs of leads for sensors H-1 and H-2 and (b) Close view of device showing sensor array on top of sensors H-1 and H-2. Sensors cover circular area of 1 mm in diameter [30].

2.3.3 Previous Work: RTD's in Various Applications

Andretta et. al. (1981) designed a heat flux meter for measuring the performance of solar collectors and natural cooling devices. The sensor consisted of two 50 μm thick copper wires glued on each side of a 60 mm diameter, 2mm thick plexiglass substrate with an epoxy resin as the adhesive component [12].

Epstein et al. (1986) developed a high frequency response heat-flux gauge designed for heat-flux magnitudes ranging from one to several hundred kW/m^2 at temperature up to 400°C, the latter of which is typical conditions found in internal combustion engines and gas turbines. The gauge consisted of 150 nm thin Nickel films, sputtered on both sides of a 25 μm thick polymide substrate (Kapton). The resistive element covered a surface area of 1.3 mm^2, with track widths of 25 μm and a total track length approximated to 20 mm (from a detailed drawing in the paper). They used gold lead wires, 1 μm thick, from the sensor to the edge of the polymide sheet, tracking a length of approximately 4-5cm [15].

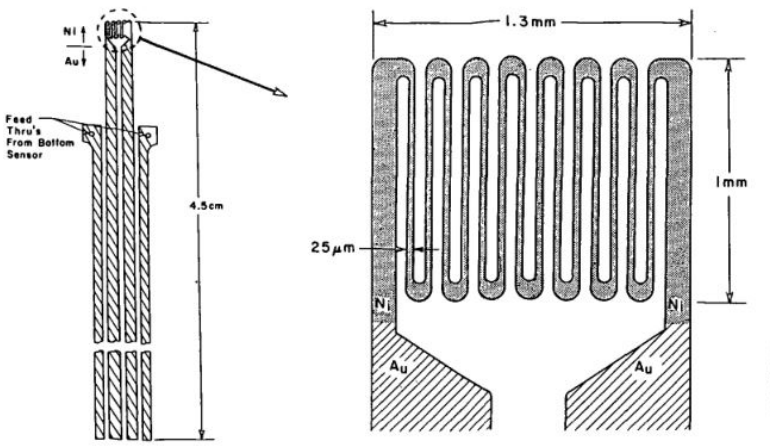

Figure 2.5: Gauge geometry showing sensor detail, sensor and thin-film gold leads, and gauges on manufacturing sheet [15] .

Guo et al. (1998) used thin film sensor technology to measure the heat transfer coefficient and cooling effectiveness over heavily cooled nozzle guide vanes. The gauge consisted of thin platinum films (<4 nm) with copper lead wires (<500 nm) deposited onto a 50 μm thick flexible polymide (Upilex) sheet, which in turn was adhesively bonded to the perspex or metal model. The platinum gauge dimensions measured 10 mm x 1mm and they were able to fit 18 gauges on both the pressure and suction side of the model surface [19].

Based on this work, Piccini et al. (2000) developed a Direct Heat Flux Gauge (DHFG) using both thin-film techniques and conventional thermocouples. The sensor was made using the sputtering technique of platinum onto a flexible polymide (Upilex-s, 50μm) substrate. The thickness of the platinum film was reported to be $<$ 100 nm thick, yielding a total gauge thickness of 50.1 μm. A conventional thermocouple was installed inside a metal model, and the sputtered film and substrate was adhesively bonded on top. They argued that, due to the high thermal conductivity of the metal model, only a small number of thermocouples were needed in order to accurately measure the temperature at the bottom surface of the gauge. [39]

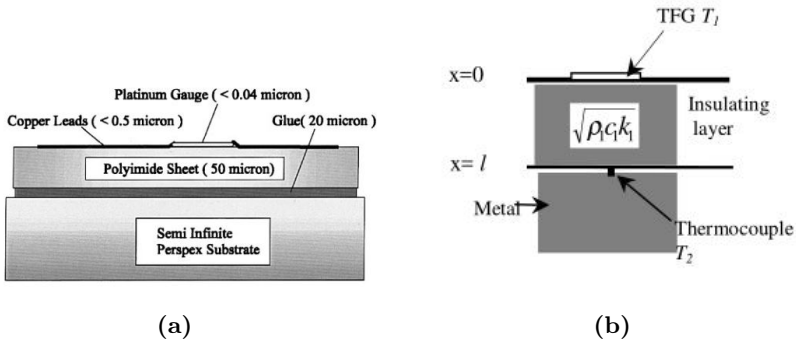

(a) **(b)**

Figure 2.6: (a) Guo et al. - Thin film gauge on polymide (upilex) sheet [19] , (b) Piccini et al. - a schematic diagram of the DHFG [39] .

Kumar er al. (2012) developed a thin film heat flux gauge for exploring the possibility of using such a device for short duration conduction based transient measurements with pure conduction mode of heat transfer. A Pyrex rod of 6 mm diameter and 10 mm length was used as the substrate material, and platinum ink as the resistive element. The reported thickness of the platinum film was determined to a few micrometers. To achieve electrical connections between the platinum thin film and external wiring, a silver paste was used. The exact thickness of the silver film is not reported, however, a much greater thickness than that of the platinum film is stated. [27]

2.3.4 Preious Work: Variations in the Temperature Coefficient

In the following papers, studies done on the variation of the Temperature Coefficient of Resistivity through dimensional variations in the RTD design and post fabrication thermal treatments are presented. The TCR values are summarized in Table (2.2) below. Values found in the aforementioned studies is included as well, where the data was available.

Author	Year	Material	T_A	TCR_B	TCR_O	[%]
Kim et al.	2001	Pt	700°C	3.297	3.927	-16
Zribi et al.	2016	Pt	(250°C, 450°C)	3.927	(1.14 - 1.35)	-71, -65.6
Kumar et al.	2012	Pt ink	650°C	3.927	2.1	-46.5
Moghaddam et al.	2006	Ni	-	6.2	1.0	-82.26
Ammar et al.	2013	Au	-	8.3	2.7	-67.47
Hamadi et al.	2012	Au	-	8.3	2.71	-67.35
Rule and Kim	1999	Pt	-	3.927	2.0	-49
Myers et al.	2005	Pt	-	3.927	1.9	-51.6

Table 2.2: Previous results found in the literature. Material, Annealing temperature (T_A [°C]), Bulk value of Temperature Coefficient of Resistivity (TCR_B [$\times 10^{-3\circ} C^{-1}$]), Observed value of Temperature Coefficient of Resistivity (TCR_O [$\times 10^{-3\circ} C^{-1}$]) and variations from the bulk value. Where multiple TCR values was observed, an averaged variation from the bulk value was noted.

In 2001, Kim et al. conducted a study on thin film platinum RTD's deposited on an alumina substrate where the sensors, after fabrication, where thermally treated at various temperatures. A serpentine pattern was transferred to the substrate using photolithography with a positive resist (AZ1518) and developer AZ351. The RTD element was then obtained by DC Sputtering and the Pt film was etched using a mixture of HCl and HNO_3. Four different dimensional variations of the RTD's were fabricated, with line width as the main variational parameter - 0.1 mm, 0.2 mm, 0.3 mm and 0.4 mm. The length and size variations between the samples is not reported, however, by a visual inspection of a detailed image in the report, the size seem to have been held approximately constant but the length to have varied between the samples.

Each of the dimensional variations of the RTD's were fabricated with two different film thicknesses – 105 nm and 206 nm. After fabrication the samples were

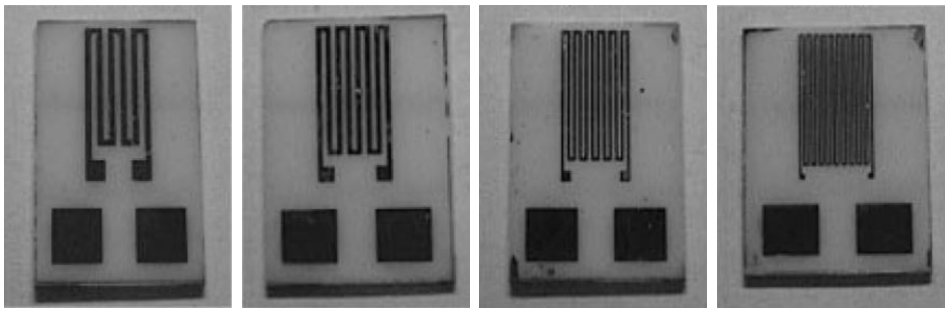

(a) **(b)** **(c)** **(d)**

Figure 2.7: RTD's of various line widths; (a) 0.4mm, (b) 0.3mm, (c) 0.2mm and (d) 0.1mm [26].

thermally treated at various temperatures in N_2 for 1 hr. before being naturally cooled to ambient temperature. The 206 nm thickness samples were used to study the effect of line width and various annealing temperatures on the TCR. Figure (2.11) show these variations, and the TCR values are observed to increase with annealing temperatures used, and decrease with increasing line width. It should be noted, however, that the impact of wire length is not documented in the study. The highest TCR value observed in the study was 3.29 $[\times 10^{-3\circ} C^{-1}]$ obtained from the 0.1 mm line width, 206 nm thickness variation, and occured after thermal treatment for 1 hr. in N_2. [26]

Zribi et al. (2016) conducted a study on the impact of annealing temperatures on thin film platinum heat flux sensors. The sensors consisted of two thin platinum films, 200 nm thick, sputtered on a 500 μm thick Borofloat 33 glass substrate. A 20 nm chromium layer was deposited between the substrate and platinum for adhesion purposes. The platinum tracks measured 45.66 mm in length and both the line width and spacing between the tracks were 60 μm. After fabrication the sensors were thermally treated at 250°C and 450°C for 6 hr. through the following scheme: (1) 10°C/min ramp up to 150°C (resp. 350°C), (2) 150°C (resp. 350°C) for 10 minutes, (3) 5°C/min ramp up to 250°C (resp. 450°C), (4) 6h at 250°C (resp. 450°C) and finally (5) free cooling to ambient temperature.

The sheet resistances were recorded before and after the thermal treatment, and the TCR values were calculated for sensors with and without annealing using different values of current in the external circuit. The values are reported in Table (2.4) and (2.5), respectively. [59]

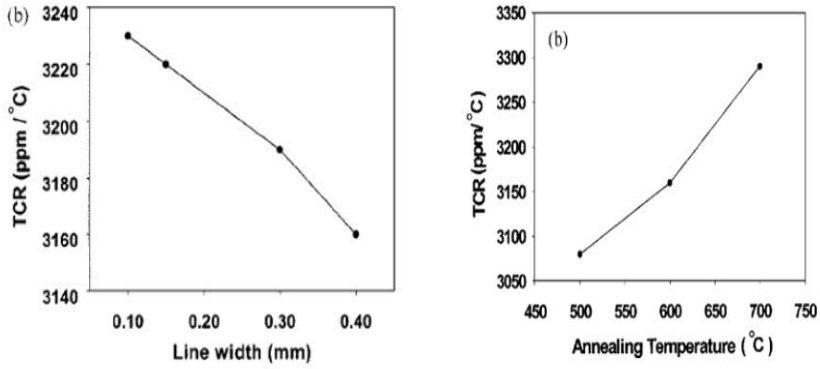

(a) **(b)**

Figure 2.8: Variation of the Temperature Coefficient with line width and annealing temperatures [26] .

	R1 [Ω]	Influence	R2 [Ω]	Influence
HS1 before annealing	575.80	-3 %	634.11	-5%
HS1 after annealing 250°C, 6hr	558.02		604.56	
HS2 before annealing	554.39	-3%	608.64	-5%
HS2 after annealing 250 °C, 6hr.	537.57		580.50	
HS3 before annealing	607.34	+21%	546.16	+25%
HS3 after annealing 450 °C, 6hr.	732.72		683.11	
HS4 before annealing	579.02	+24%	663.02	+22%
HS4 after annealing 450 °C, 6hr.	719.37		809.89	

Table 2.3: Impact of annealing on sheet resistances of thin film platinum RTD's [59] .

	TCR_{R1}	TCR_{R2}
Without annealing 1mA	1.35	1.24
Annealing 250°C, 6hr., 1mA	1.19	1.14
Annealing 250°C, 6hr., 1mA	1.24	1.25

Table 2.4: Impact of annealing on TCR value with different currents in electrical circuit. Subscripts indicates resistive films on side 1 and 2, respectively [59] .

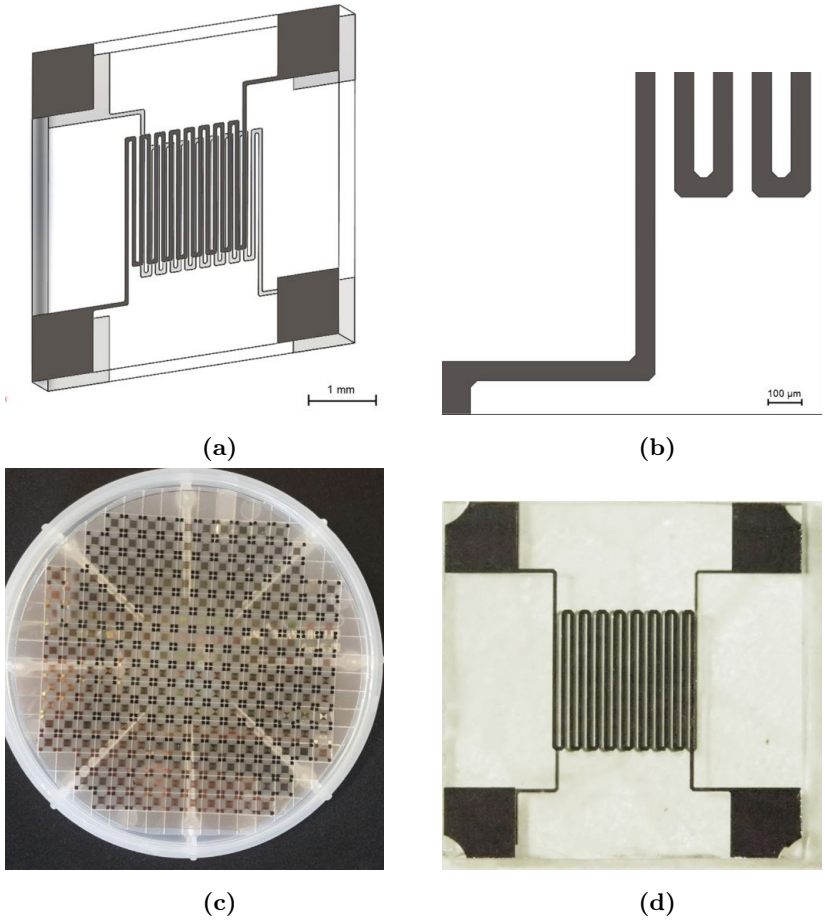

Figure 2.9: RTD's fabricated; (a) Heat flux sensor design, two RTD's shown on each side of the glass substrate, (b) RTD tracks, (c) 228 individual sensors fabricated on Borofloat 33 glass wafer and (d) individual heat flux sensor [59].

2.4 Summary and Focus of This Thesis

As may be observed from the literature presented, RTD's are extensively used and preferred due to their minimally intrusive nature and high accuracy. However, the RTD's fabricated by Hamadi et al. showed very low sheet resistances and accordingly low sensitivites. Although it may have been sufficient for their specific application, they conclude that the sensors may be adjusted according to the width of the microchannel. This might cause issues since the sheet resistance is proportional to the length of the resistor, and decreasing the length below what was reported may result in sensors with sheet resistances below what is required. Low sensitivity sensors post a huge demand on the accuracy required by the external circuit, and so special concideration should be attributed to maximizing the sheet resistance from a design perspective.

The main focus of this thesis will be to design and fabricate resistance temperature sensors with high resistance and high sensitivity. The size-variations that will be attempted is summarized in Table (2.5) and Figure (2.10) plots these variations and compares them to the RTD's encountered in this review.

Label	Size	track width	thickness
S1	1 μm^2	$20nm$	$40nm$
S2	2 μm^2	$40nm$	$40nm$
S3	3 μm^2	$60nm$	$40nm$
S4	4 μm^2	$80nm$	$40nm$
S5	5 μm^2	$100nm$	$40nm$
S6	6 μm^2	$120nm$	$40nm$

Table 2.5: Size variations of the sensors in this work.

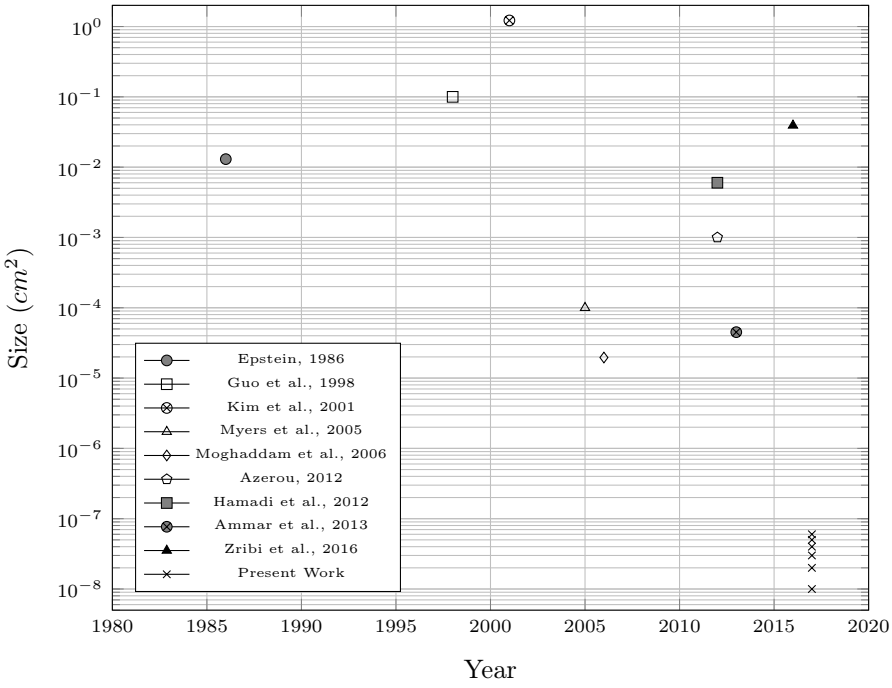

Figure 2.10: Semilogarithmic plot showing RTD sizes Vs. year. No clear trend has been unveiled based on the papers reviewed by the author. Included, in the bottom rigth corner is the focus area of the present work.

Chapter 3

Resistance Temperature Detectors

The Resistance Temperature Detector (RTD) utilizes the temperature dependence of the electrical resistance in metals to measure the temperature. Conventional applications consists of a length of metal wire that is wrapped around a ceramic or glass core [8]. The wire, i.e. the resistive element, is brought into contact with the environment in which the temperature measurement is desired and the electrical resistance is recorded using an external circuit. In commercial RTD's where the size of the resistance element exhibits bulk materialbehaviour, the electrical resistance at various temperatures is well documented. The development of micro- and nanoscale fabrication techniques, especially in relation to the microelectronics industry (now nanoelectronics industry), have made it possible to realize RTD's on much smaller scales. The thin-film RTD consists of depositing thin sheets of metal directly onto a substrate. These devices may be used as either temperature sensors or heat flux sensors, the latter of which conventionally consists of two thin-film RTD's, deposited on either side of a thermal insulator. The temperature recordings on each side serve as boundary conditions for the insulating wall, and the heat flux is modeled by conduction according to Fourier's Law. In this chapter the working principles of RTD's and RTD measurements is presented a long with common materials used for this purpose.

3.1 Working Principle

The electrons in metals are not bound to individual atoms, but are free to move randomly throughout the lattice structure. Generally, this makes metals good electrical conductors. However, all metals, in various degrees, inhibits an oposition to an electric current caused by impurities in the material structure and temperature. This oposition is conceptualized trough a a material property termed *resistivity*, ρ.

Given a metal slab of constant geometric shape, the overall resistance is given as [28]

$$R = \rho \cdot \frac{L}{A_c} \tag{3.1}$$

where R is the electrical resistance (Ω), L is the length of the metal slab (m), A_c is its cross sectional area, and ρ (Ω·m) the electrical resistivity. Equation (3.1) suggests that there are two principle ways that the resistance might change: (i) by the variations in resistivity and (ii) by the geometrical dimensions, e.g. through thermal expansion effects. Subsequently, the resistivity may change in two principle ways as well: (i) by the application of strain[1] or (ii) by the change in temperature. The fundamental mechanisms involved in the temperature dependence of resistivity are beyond the scope of this work and the reader is referred to the literature for more information. For the purpose of this thesis, the temperature dependance of resistivity is quantified through experimental observations by Equation (3.2) as

$$\rho(T) = \rho_0(1 + \alpha_R(T - T_0)) \tag{3.2}$$

where ρ_0 is the initital resistivity at some ambient temperature – usually 0°C – α_R is the temperature coefficient of resistivity (TCR) and T is the temperature (T_0 is the ambient temperature).

Combining Equations (3.1) and (3.2), and assuming the geometrical change in the slab to be negligable, the resistance may be written as

$$R(T) = R_0(1 + \alpha_R(T - T_0)) \tag{3.3}$$

where R_0 is the sheet resistance at ambient temperature.

Assuming that temperature scale is in Celsius and that the ambient temperature is taken at 0°C the resistance–temperature relationship is given by Equation (3.4) as [34]

[1] The change in resistivity to the application of strain is the general working principle of piezoresistive strain gauges.

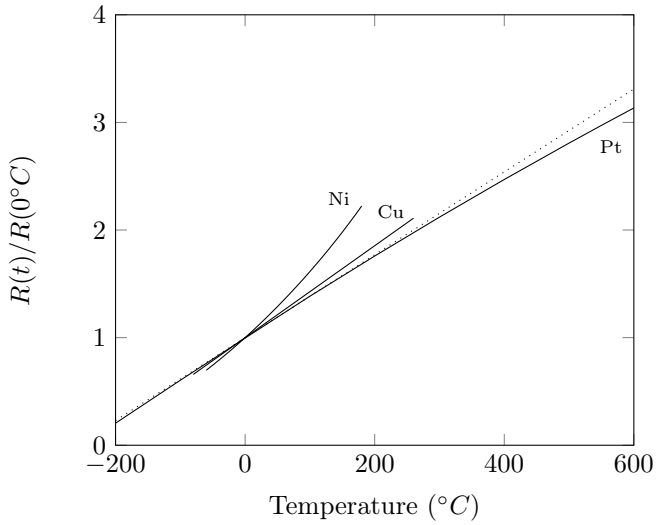

Figure 3.1: Resistance of nickel, copper and platinum as a function of temperature. Note that these plots are scaled by the sheet resistance, R_0, and the slope here is given by α_R only.

$$R(T) = R_0(1 + \alpha_R T) \tag{3.4}$$

which provides a simple linear relationship between the variables and establishes the working principle behind Resistiance Temperature Detectors (RTD's). This result is not valid for all metals, as they will exhibit various degree of linearity through their temperature range. However it is this linearity that is sought after in a good resistance thermometer. Differentiating Equation (3.4) with respect to temperature, and defining the sensitivity as the slope of the resistance–temperature relationship, the sensitivity is given by the product of the alpha-value and the sheet resistance as

$$S = \alpha_R R_0 \tag{3.5}$$

where S is the sensitivity. A high sensitivity of RTD's are desirable due to the ease of measuring large variations in resistances with only an incremental change in the temperature recording.

3.1.1 Common Materials

Figure (3.1) illustrates the relationship between resistance and temperature for copper, nickel and platinum – three of the most common materials for resistance temperature measurements. The graph is generated from the values and equations found in appendix (E) of this thesis. The dotted line illustrates the simple linear relationship from Equation (3.4) for platinum, using bulk material properties and α_R taken as 3.85 ($\times 10^{-3} \mathrm{^\circ C^{-1}}$), accordingly. The continuous platinum line is generated by the Callendar-van Dusen Equation, and corresponds very well with the simple model. As suggested by the figure, copper also exhibits a high degree of linearity, in fact, even more so than platinum. However, copper suffers from low overall sheet resistance and are susceptible to corrosion at high temperatures and therefore offers a limited measurand range (between -80°C to 260°C) [34]. Nickel is primarily chosen for its high sensitivity, with a bulk material α_R value of 6.18 ($\times 10^{-3} \mathrm{^\circ C^{-1}}$), nearly twice that of platinum [34]. However, the range is limited, only -60°C to 180°C. Platinum offers a wide temperature range, in which the resistance–temperature relationship is very linear, and an unchallenged chemical inertness even at elevated temperatures and in corrosive environments.

3.2 Resistance Measurements

For the intended knowledge of the temperature to be gained, accurate measurements of the resistance is required. This section outlines the general principle behind resistance measurements and introduces one of the most popular techniques in the field. For the purpose of this thesis only the *Wheatstone Bridge* configuration will be covered and the reader is referred to the literature for information regarding other resistance measurment techniques.

3.2.1 General Principle

According to Ohm's law, the resistance can be measured by calculating the ratio of the voltage across the resistor, to the current passing through it as [34, 35].

$$R = \frac{V}{I} \tag{3.6}$$

where V and I is the voltage and current, respectively. However, the electric current is defined as a differential change in charge to a differential change in time through Equation (3.7), as [36]

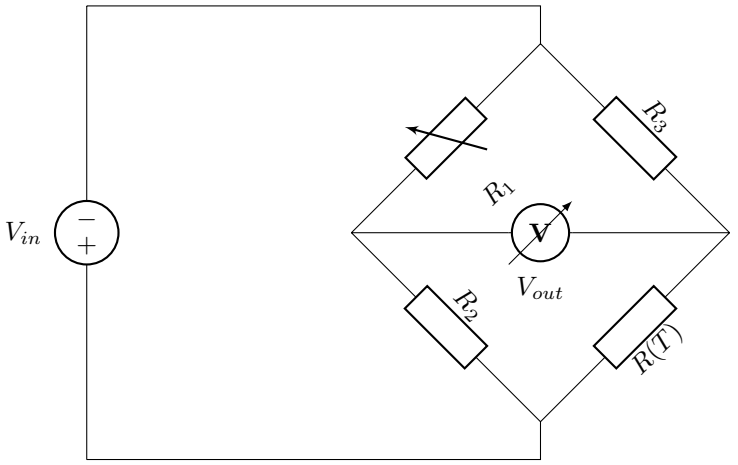

Figure 3.2: Representation of a simple Wheatstone bridge circuit configuration. Resistance of interest, $R(T)$, in series with known resistance R_3, both in parrallell with known and variable resistances R_2 and R_1, respectively. A voltagemeter measures the electric poetential between the parrallell branches, i.e. the bridge potential. V_{in} is the applied voltage to the circuit.

$$I = \frac{\delta q}{\delta t} \tag{3.7}$$

where q is the charge in coulombs (C), and t is time in seconds. This means that the electrical current is not easily measured without pre- establishing the voltage and resistance, and the direct use of ohm's law is not applicable. In practice, resistances are measured by eliminating the need for direct current measurements by configuring the resistance in circuits termed *bridges*. In a bridge configuration, the resistance is compared with other resistances to establish its value. The most adopted configuration for accurate resistance measurements is the *Wheatstone Bridge*, popularized by Sir Charles Wheatstone in 1843 [57].

3.2.2 The Wheatstone Bridge

Figure (3.1) illustrates a simple Wheatstone Bridge circuit configuration. A voltage source V_{in} is applied to a circuit where four resistances are placed in parallell, in which pairs of two are in series. One of the resistances, $R(T)$, is the unknown resistance, and one of the resistances in the other series, here R_1, is variable. A voltage detector, V_{out}, records the electric potential between the two series, i.e. the bridge potential.

Balance-mode Vs. Voltage-mode

There are two principle ways of attaining the value of the unknown resistance. In the balance-mode, the variable resistance is adjusted until there is no potential between the branches. The output voltage of the bridge is given by Equation (3.8) as [34]

$$V_{out} = \frac{R_3 R(T) - R_1 R_2}{(R_1 + R_2)(R_3 + R(T))} V_{in} \tag{3.8}$$

where R_i $(i = 1, 2, 3)$ are the known resistances, and $R(T)$ is the unknown. Since the output voltage is adjusted to null, the voltages fall out of the equation and the unknown resistance is given as

$$R(T) = \frac{R_3}{R_2} R_1. \tag{3.9}$$

In the balance mode, the voltage, V_{out}, only needs to detect a zero potential, which reduces the accuracy requirements conciderably [34]. In the voltage-mode, the variable resistor, R_1, is initially balanced at a set temperature, (T_0), and the voltage measurement becomes the direct measurement of the temperature. Thus,

$$V_{out} = \frac{R(t) - R(t_0)}{(R_3 + R(T))(R_3 + R(T_0))} R_1 V_{in} \tag{3.10}$$

and

$$V_{out} = \frac{V_{in}}{R_3} R(T_0) \alpha_R T \tag{3.11}$$

where the output voltage V_{out} is itself proprtional to the temperature. Most high-precision thermometers operate on this principle [34].

3.2.3 Errors

Measuring the resistance of an RTD introduces several sources of errors. These include self-heating errors, lag- and settling errors, thermal expansion errors and resistance errors from lead wires and external circuitry, to name a few [34]. For thin-film thermometers, the thermal time response is considered low due to the small volume of the device, and lag- and settling errors are generally low. Since the lead wire errors may be somewhat limited due to smart design, this aspect of measurment errors is included in this subsection in addition to the self-heating error due to its importance.

Lead Wire Resistances

The problem with using the simple Wheatstone Bridge configuration of Figure (**??**) is that the lead wire resistances are indistinguishable from the resistive elements, motivating the need for simoultanious lead wire resistance measurements. This can be done by deploying Wheatstone Bridges were the resistance in the lead wires are recorded simoultaniously with the sensing element by using three or four lead wires.

Smart design may also decrease this effect by ensuring that the lead wire resistances are low compared to the sensing element. Choosing low resistance materials and ensuring that the lead wires are large compared to the resistor might be enough to accomplish this. However, for high-precision thermometry, the use of four-lead measurments will completely cancel out the additional lead wire resistances, and is therefore recommended. The only main dissadvantage is the introduction of additional wires and measurement complexity.

Self-Heating Error

In order for the resistance to be measured a current is passed through the sensing element. By the introduction of this current the sensor will itself heat, yielding an error in the measurement. This error is given as [34]

$$\Delta T = \frac{R(T)I^2}{h} \tag{3.12}$$

where ΔT is the temperature error, $R(T)$ is the electrical resistance, I is the current and h is a heat dissipation factor. Since the temperature error is proportional to the squared of the current, the self-heating error may be held within apropriate limits by introducing a very low current in the external circuit.

Chapter 4

Fundamentals of Sensors

4.1 Clarifications

Transducers, sensors and actuators are terms of which there exists a vast variety of definitions, and there is often some hesitation in selecting the proper word, *sensor* or *transducer*, since the meaning of the words are somewhat overlapping in every day use [48]. This section will present a short explanation of what is meant by each of the formentioned terms with respect to this thesis.

4.1.1 Transducers, Sensors and Actuators

Sensors and actuators are collectively referred to as transducers [28]. A transducer is generally defined as a device which serves the function of transforming signals or power from one energy domain to another [38]. There are six major energy domains: (1) Radiative domain, (2) Magnetic domain, (3) Chemical domain, (4) Thermal domain, (5) Mechanical domain and (6) Electrical domain. In this regard, sensing can be broadly defined as an energy transduction process that results in perception, and actuation is an energy transduction that produces an action [28]. Sensors and actuators are thus devices which undergo the respectable transduction processes.

A more specific definition of a sensor, and the one that will be used in this thesis, is provided by Pallas, who defines a sensor as a transducer that specifically produces an output signal in the electrical energy domain [38].

4.2 Classification of Sensors

In order to compare different types of sensors and get a comprehensive overview of them, they need to be classified. In 1987, Richard M. White presented a classification scheme for sensors that has been widely adopted due to its flexibility. Six major classes were presented: (1) Measureands, defined as the input quantities, properties, or conditions that are detected or measured by sensors [50] , (2) Technological Aspects, (3) Detection Means Used in Sensors, (4) Sensor Conversion Phenomena, (5) Sensor Materials and (6) Fields of application [43].

For example, if the measureand is temperature or heat flux, it is measured by a thermal sensor.

For the purpose of this report, the second class, Technological Aspects of Sensors, are the most relevant and are therefore listed in Table (4.1) below, as given by Richard M. White in his 1987 paper. The scheme was developed by the motivation of being able to compare sensors, clarity in communication about sensors and to track sensor progress and availability [43].

Table 4.1: Technological Aspects of Sensors [43].

	Technological Aspects of Sensors
1	Sensitivity
2	Measureand Range
3	Stability (short-term, long-term)
4	Resolution
5	Selectivity
6	Speed of Response
7	Ambient Conditions Allowed
8	Overload Characteristics
9	Operating Life
10	Output Format
11	Cost, Size, Weight
12	Other

4.3 Sensor Characteristics

The focus of this report is thermal sensors, or more specifically Resistance Temperature Detectors (RTD's), which will be introduced in detail later in this chapter. In the following sections the relevant technological aspects, or characteristics, of RTD's are presented.

4.3.1 Size

In real world heat transfer phenomena, the temperature and heat flux within a system is not uniform, i.e. the respective quantities might change between locations and the spatial variations between them may be very small. It is important that the measuring device is able to detect these variations in order to gain an understanding of the distributed quantities within the system of interest. Size is therefore an important characteristic, and considerations of the system in question should be taken in order to determine the size of the sensor to be used.

In heat transfer, the physical size of the domain under investigation have been of interest to scientists for over 400 years . Even though the fundamental within a domain of microscale or nanoscale dimensions typically are the same, the effect of small length scales often make conventional, macroscopic, approaches to the analysis inappropriate, or in some cases, incorrect [48]. However, the non-agreements observed between macroscopic analytical approaches and experiments, have been argued for by the intrusive nature of the metrology devices available at the time of investigation, i.e. the presence of the sensors used (large compared to the characteristic length scales in the domain) interfere with the nature of the system and therefore generate false values.

In this report, the sensor size is defined as the footprint of the resistive element, excluding lead wires and bond pads - see Figure (4.1) - so that size, S, equals the area comprised of X and Y. Also shown, in (b), is the track width (w) and film-thickness (t). Total track length is taken as the distance covered by the resistive element between the lead wires. More detail will be covered in the chapter 4.

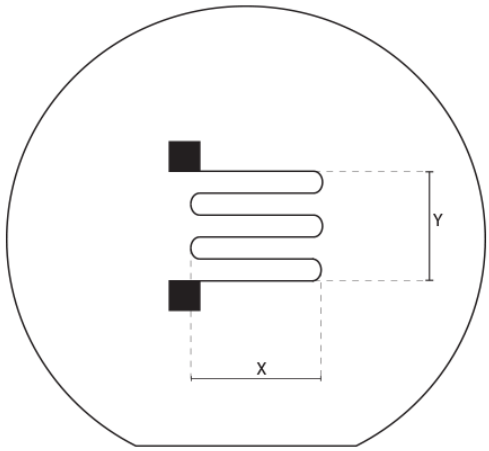

(a)

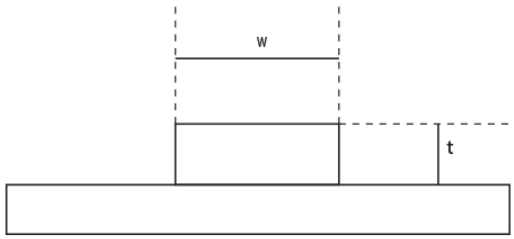

(b)

Figure 4.1: (a) Sensor size , (b) track width and film thickness .

4.3.2 Operability

Linearity

If the output signal changes proportionally with respect to the input signal, the response is said to be linear [28]. In terms of RTD's, the input signal is temperature or heat flux and the output is either a voltage, V, or a current, I.

A linear response of a sensor is desirable due to the alleviation of complex signal processing.

Linearity of a sensor is quantified through the closeness of the calibration curve and a specified straight line, and is measured as the maximum deviation of any calibration point from this line during any one of the calibration cycles [48].

Sensitivity

Sensitivity is the ratio of change in sensor output to the change in the value of a measureand. For an RTD, where the output is a voltage V that is related to the temperature, T by $V = f(T)$, the sensitivity is [48]:

$$S = \frac{\delta V}{\delta T} \tag{4.1}$$

Response Time

Response time is the amount of time elapsed between a change in the measureand of the sensor input to the resulting indication of that change in the sensor output. Often the response time of a sensor is given as the time at which the sensor output reaches 63% in its final value in response to a step change in the sensor input.

The response time results from a frequency analysis of the mathematical model of the system and can be further divided into a lag time before the sensor starts to respond, a time constant based on the natural frequency and damping of of the system, and a stabilization time before the final reading value is being approached [37].

Measureand Range

The measureand range is the upper and lower limits of the measureand values, over which the sensor is intended to operate.

Accuracy

Accuracy is the ability of a sensor to exactly hit the true value of a measurand. Bias is often used to quantify accuracy and is given as [23]:

$$Bias = \mu_{measurement} - \mu_{true} \tag{4.2}$$

Precision

Precision may be defined as the consistency between measurements and is comprised of repeatability and reproducibility through the following relationship:

$$\sigma^2_{measurementsystem} = \sigma^2_{repeatability} + \sigma^2_{reproducibility} \tag{4.3}$$

where reproducibility is the cumulative measurment variation that arises due to different conditions that may exist during measurements, and repeatability is the variation of measurments conducted under the same operational conditions [23].

The difference between accuracy and precision is graphically represented in Figure (4.2) below.

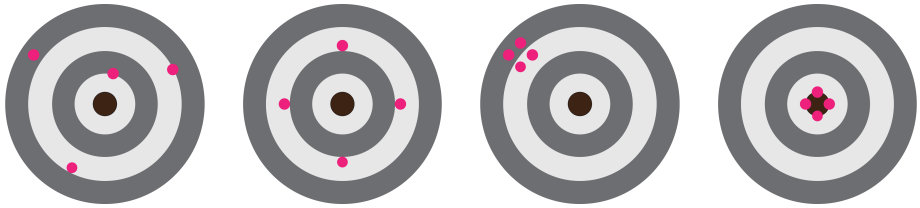

Figure 4.2: Accuracy and Precision - (a) Neither accurate or precise, (b) Accurate, (c) Precise, (d) Accurate and Precise.

Noise

Sensing noise is defined as anything that obscures a desired signal [28], and can itself be another signal (interference). Most often, however, the term random noise is used to describe noise of physical origin.

Hysteresis

Hysteresis comes into play when a sensor fails to return to the same output values when cycling up or down though values on the measurand range. In this regard, hysteresis may be viewed as a condition where, in addition to the current sensor environment, the previous sensor environment also affects the sensor readings. For temperature sensors, hysteresis becomes apparent during temperature cycling. Figure (2.3) below provides a graphical interpretation of hysteresis, where a sensor measures two different temperatures for the same resistance recording during a temperature cycle:

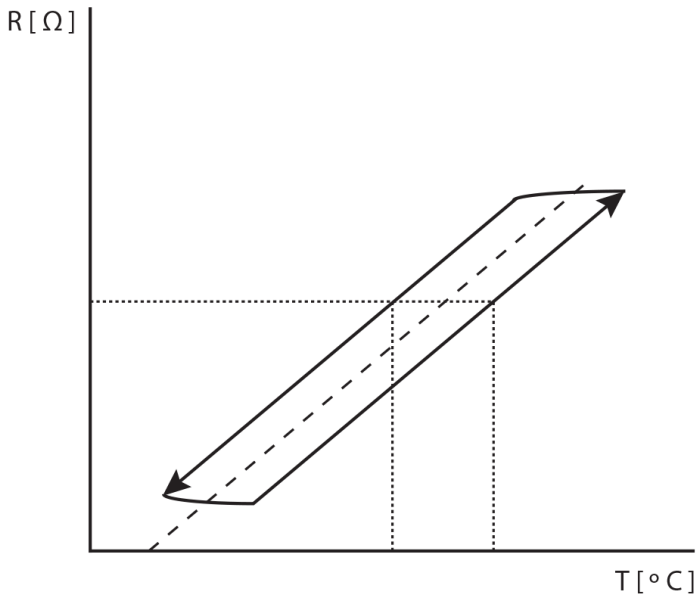

Figure 4.3: Hysteresis. The dotted line represents the relaxed state, i.e. the state of the sensor in which it has "forgotten" the previous operational environment.

The dotted line represents the relaxed state, i.e. the state of the sensor in which it has "forgotten" the previous operational environment.

Part II

Present Work

Chapter 5

Materials and Methods

5.1 Materials

The thin-film RTD's were realized using a silicon substrate, with platinum wires as the resistive element, and gold lead wires and bond pads as connections with the external circuit. Titanium was used in the silicon–platinum, and silicon–gold interfaces for adhesion purposes. Thus, the structural layers were silicon–titanium–platinum for the resistive elements, and silicon–titanium–gold for the lead wires and bond pads. In the following subsections, the material considerations will be explained.

5.1.1 Silicon

Silicon is the second most abundant element on earth, making up about 25% of the earth's crust in the form of silica (S_iO_2) or other silicates [41]. In 1956, Gordon K. Teal demonstrated a method in which single silicon crystals could be grown in commercial quantities [16]. Therefore, silicon is both cheap and available.

Silicon belongs to a class of materials known as *semiconductors*. A semiconductor is special because it can function as either a conductor or an insulator, i.e. when energy is applied to the material, e.g. due to heating, the electrons are excited and jump from the valence band to the conduction band where electrical conduction may occur if a voltage is applied. Silicon has four valence shell electrons, which places it midway between the valence-shell conditions for a good conductor (one valence electron), and a good insulator (eight valence electrons), and thus inhibits material properties of both metals and non-metals [41].

With a melting point of 1412°C, silicon is ideally suited for a wide process range [41]. This high-temperature tolerance is desired in semiconductor devices due to the increase in both variety of applications and reliability.

Finally, silicon exhibits the ability to grow silicon dioxide (S_iO_2) on the surface naturally. S_iO_2 is known to be a high-quality electrical insulator, which also serves the purpose of protection against contaminants [47].

Concerning the present work, silicon serves yet another advantage. In the investigation of future trends within electron beam lithography technology, Tennant and Bleier (2010) ran a series of electron scattering simulations for various substrates using the Monte Carlo method. The simulations were run at different beam energy levels – 25 keV to 200 keV, and the forward- and backscattering parameters, α and β, respectively, as well as the ratio of the energy deposited from the backscattered electrons to that of the incident electrons, η, were recorded [51]. The results are tabulated in Table (**??**) and plotted in Figure (5.1). The investigation of the plot in Figure (5.1) reveals that silicon has a near minimum η value at 100 keV, which makes it ideally suited for the system used in this work. More about this system and electron scattering in Section (5.3).

Table 5.1: Simulation of point spread function dependence on energy [51].

Material	Energy (keV)	(μm)	β (μm)	η
GaAs	25	0.0086	1.18	1.13
GaAs	50	0.0078	3.65	0.98
GaAs	100	0.0071	12.78	0.94
GaAs	150	0.0067	25.11	0.94
GaAs	200	0.0066	40.12	0.97
InP	25	0.0087	1.20	1.21
InP	50	0.0078	3.64	1.06
InP	100	0.0071	12.65	1.04
InP	150	0.0068	27.62	0.98
Inp	200	0.0067	40.09	1.04
Si	25	0.0086	2.85	0.67
Si	50	0.0077	10.18	0.65
Si	100	0.0070	34.14	0.59
Si	150	0.0067	72.91	0.65
Si	200	0.0065	123.40	0.77

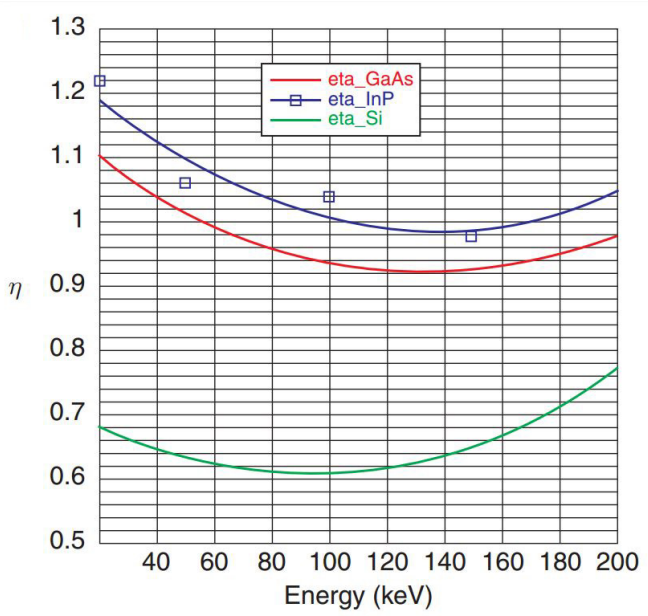

Figure 5.1: Plots showing the ratio of the energy deposited from the backscattered electrons to that of the incident electrons. As may be seen from the graph, Si (green) has a near minimum at 100keV, suggesting Si as an ideal substrate material for systems of these voltages [51].

Molecular Structure and Crystal Orientation

In the periodic table of elements, Silicon is located in group IVA and period II. It has 14 protons and 14 neutrons in the nucleus, two electrons in the orbital shell and 12 electrons in the valence shells – eight in the L-shell and four in the M-shell. When silicon atoms form crystals, they are regularly arranged in a lattice structure with different orientation. Material properties and fabrication techniques, such as *etching*, may exhibit an orientation dependence. To keep track of the orientations, a set of standard notations called *the Miller Index* have been developed for the identification and visualisation of the planes and directions in a crystal lattice [28]. Since the fabrication of the present work is not dependent on the variations in the crystal structure of silicon, it is not further discussed here, and the reader is referred to the literature for more information.

(a) Platinum

(b) Gold

(c) Titanium

5.1.2 Platinum, Gold and Titanium

Platinum was used as material for the resistive element due to its highly linear behavior through a wide range of temperatures and relatively high temperature coefficient of resistivity. To ensure that the measured resistance actually stems from the resistive elements and not the lead wires and bond pads, gold was found suitible for this purpose since the bulk resistivity of gold is approximately one order of magnitude lower than platinum yielding a lower sheet resistance for geometrically similar constructions. Finally, Titanium was used as an adhesion layer between the silicon – platinum and silicon – gold interfases. Specific information regarding this interaction is hard to come by in the literature. However, the use of titanium for this purpose is widely adopted.

Table 5.2: Sensitivity factors for various film thermometer materials (for excitation at constant dissipation) [15].

Metal	T [°C]	ρ	α_R	Sensitivity, $\alpha_R\sqrt{\rho}$	Rank
Zirconium	20	40.0	4.4	27.8	1
Iron	20	9.71	6.51	20.2	2
Nickel	20	6.84	6.9	18.0	3
Tin	0	11.0	4.7	15.5	4
Tantalum	25	12.45	3.83	13.5	5
Platinum	20	10.6	3.927	12.7	6
Gold	20	2.24	8.3	12.4	7
Palladium	20	10.54	3.74	12.1	8
Cadmium	0	6.83	4.2	10.9	9
Chromium	0	12.9	3.0	10.7	10
Zinc	20	5.916	4.19	10.1	11
Copper	20	1.678	6.8	8.8	12
Aluminium	20	2.6548	4.29	6.9	13

5.2 Wafer Cleaning and Surface Conditioning

The importance of wafer cleaning has been recognized since the emergence of the solid state device technology in the 1950s. Performance, reliability and product batch yield are critically affected by chemical contaminations and particle impurities on the substrate or the device surface. With device sizes now on the scale of nanometers, extreme sensitivity to these contaminants are critical, and clean wafers are more important than ever. The manufacturing of an integrated circuit consists of 500-800 steps, in which 15-25% are cleaning processes, and 50% of yield losses are estimated to be caused by micro contamination. In this regard, wafer and substrate cleaning is a whole industry on its own, and its importance should be recognized by both researcher and manufacturer in micro-/nano technology. Each new step in a fabrication process may contribute to impurities which need to be removed before continuation can occur. Additionally, cleaning steps may also function as surface conditioning, i.e. prepare the wafer surface chemically for the next manufacturing process.

In this section, the cleaning considerations of the present work are presented. A *solvent clean* was deployed as the primary cleaning procedure, in addition to dry-cleaning processes such as *Plasma Stripping and Cleaning*, both of which will be explained in detail. The cleaning resources at the NTNU Nanolab are somewhat limited. However, consistent results may be obtained for single wafer cleaning. The primary source used in this section is the 2^{nd} edition of the book *Handbook of Silicon Wafer Cleaning Technology* from 2008 [42] and additional references are cited throughout the section.

5.2.1 Liquid Cleaning Process

Liquid cleaning processes are based on the use of aqueous chemicals, organic solvents or mixtures of the two. The mechanism of liquid cleaning may be either physical dissolution, chemical reaction dissolution, or both. Advantages of liquid cleaning processes include high solubility of chemical reagents and contaminants, the aid of drag forces to remove solid contaminations, and the avoidance of particle deposition after cleaning due to electrostatic forces. In this work, a solvent clean was deployed, with a combination of acetone, ethanol, isopropyl alcohol (IPA) and De-Ionized Water (DIW), in the respectable order. The order of the solvents are important. IPA is considered purer than ethanol and acetone, with ethanol cleaner than acetone. However, rinsing with DIW was found to leave watermarks on the wafer, which happens consistently if the DIW is left to evaporate on its own. Dry-

ing in an N_2 gas environment will help to prevent this. However, the gas should be provided immediately and at an elevated temperature , which is tricky for a single operator and, and not available at the NTNU Nanolab, respectively [kilde 190,191]. It was found that IPA is used as a drying agent in the industry, through a mechanism called *Marangoni Drying*. After removal from a DIW rinse, the wafer is exposed to an H_2O miscible tensioactive organic solvent vapor, usually IPA [42]. Surface tension effects cause the H_2O to sheer off a planar wafer surface, leaving a clean and dry hydrophilic surface [**?** , 198] This effect was imperfectly recreated and combined with forced N_2 drying, by rinsing the wafer with IPA after DIW rinse and permitting the IPA to dry in an N_2 environment at ambient temperature. The results were satisfactory, and this technique was used as primary cleaning procedure.

5.2.2 Plasma Stripping and Cleaning

After liquid cleaning, organic residues may be left on the wafer surface. To remove these, a dry-cleaning technique with an O_2 Plasma was used, which produce free radical oxygen particles that react with, and remove, the organic contaminants left on the surface. The Plasma will remove all organic material at a fixed rate, and was also used as a post development step to remove resist residuals that may inhibit adhesion with the silicon substrate. This technique is termed *Plasma Ashing*. A Femto Diener Electronics Plasma Cleaner was used in this work. Generator and O_2 values were consistently 50/50. Cleaning and ashing were done for 3min, and 60s intervals, respectively.

Wafer Storing

Ideally, the wafers should be stored in chemically cleaned glass or stainless steel enclosures, immersed in the continuos flow of N_2 gas. Such an environment does not exist in the NTNU Nanolab, so a conventional plastic container was used for wafer

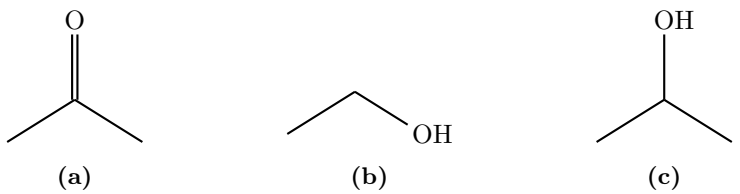

Figure 5.3: Molecular structures of (a) acetone, (b) ethanol and (c) isopropyl alcohol (IPA).

storage, with a plastic spring keeping the wafer in place. During the fabrication process, this was also used as a wafer carrier between the various steps. It was noticed that the continuos opening and closing of the container attracted a lot of particles that eventually was introduced to the wafer itself. However, the bottom of the container interior is concave, allowing the wafer to be stored upside down, protecting the front surface from contaminations from the lid and spring, and this considerably improved the situation.

Plastic containers are sources of organic contamination, so care was taken in order to keep the container clean. To further avoid contamination from storage, the fabrication processes were completed in single sessions when possible, so that only the finished devices were stored.

5.3 Fabrication Methods

In this section, the fabrication techniques used will be presented. When working with nanoscale fabrication, there is no single method that dominates concering importance. All steps must compliment each other for the fabrication to be successful. However, the techniques vary significantly in complexity. The most complex process in this work is electron beam lithography. Therefore, most of this section is devoted to EBL, spanning from the electron sensitive resist to post-exposure development – three highly sophisticated, and equally critical components of the nanofabrication process.

5.3.1 Electron Beam Lithography

Electron Beam Lithography is a fabrication technique which allows a pattern to be transferred from a CAD-file onto a substrate. Unlike conventional photolithography, where the pattern is transferred by the change in chemical structure of a photo-sensitive resist, allowing selective removal through development, the resists used in EBL are sensitive to accelerated electrons, instead of photons. The developed resist produce binary patterns which act as masks for subsequent fabrication steps, such as etching or metalization through deposition. An Elionix ELS G-100 was used in the fabrication process in the present work. The ELS G-100 is a high speed, ultra high precision thermal field emission (TFE) EBL system with an acceleration voltage of 100 kV and 100 MHz pattern generator [6]. Beam currents may be varied between 100 pA and 100 nA, where the actual beam spot size varies from 1.8 nm to 100 nm, respectively. A small current is used when a high resolution is desired, i.e. small patterns or sharp corners in larger ones, and large currents are used for large pattern exposure to decrease the throughput time.

Gaussian Beam

Even though the beam spot diameter is given as a function of the beam current, it is important to note that the beam is not a perfect spot. In fact, the Elionix system has a near Gaussian shape, and the beam diameter is taken as the spatial extension in a set interval of the entire exposure density distribution (EID) [53]. The induced effect may be that, leaving the beam spot in the same position over time, will expose areas that may not have been intended. This is especially important for small, dense patterns, where this can cause the patterns to bleed into each other, resulting in no pattern at all. Therefore, care should be taken when selecting a proper beam current and write field size, dot number and pitch.

Electron Scattering and Proximity Effects

The problem with using electrons in lithography is the fact that they are charged particles. When electrons enter a new medium, they scatter due to interactions with the particle charges present in the resist and substrate material. When the incident electrons enter the resist, they experience elastic and inelastic collisions with the resist atoms.

The inelastic collisions are characterized by a small scattering angle and the elastic collisions are characterized by a large scattering angle [17], with negligible transfer of energy.

For the incident electrons entering the resist, the collisions are dominated by inelastic collisions and results in the energy transfer which alters the resist chemically, allowing selective removal through development. The scattering they experience is termed *forward-scattering* and is small for high voltage systems. When the electrons enter the substrate, however, which has much more densely packed atoms, the collisions are dominantly elastic. This means that the electrons are deflected away from their path, possibly back into undesired areas of the resist where they deposit their energies. This form of scattering is called *back-scattering*. The exposure of unintended areas through forward- and back-scattering is called the *proximity effect*. The proximity effect is particularly present when writing patterns containing both small and large features, or for small patterns of high density. Figure (5.5) plots the result of a scattering simulation, and show the trajectories of a million electrons in 100nm layer of PMMA resist on a 250 μm Si substrate. The backscattering is seen by the lateral spread of electrons, some of which find their way back into the resist layer (invisible here due to scaling difference between the resist layer and the substrate thickness). Proximity effects may be corrected for by alterations of the dose explained in the subsequent section.

Area Dose

When a focused beam of electrons is scanned over the substrate in the desired pattern for a given amount of time, a certain amount of electrons is delivered. This amount is called an *area dose* (μC cm^{-2}), and is given by Equation (5.1) as

$$D_{area} = \frac{I_{beam} \cdot t_{exposure}}{A_{exposure}} \tag{5.1}$$

where I_{beam} is the current of the beam measured in amps (A), $t_{exposure}$ is the exposure time (s) and $A_{exposure}$ is the exposure area (cm^2). EBL resists have different area dose requirements, termed *base dose*. Exposures below and above the

base dose, will result in an incomplete exposure, or expose everything, respectively. A *dose test* is performed to establish this threshold, where a pattern is exposed numerous of times, at different doses. The remaining resist after development is measured, and the base dose is established by the first pattern in which no resist is left. However, the dose requirement is dependent on various parameters such as minimum structure size, the developer used after exposure, resist, acceleration voltage and the thickness of the resist film. The area dose is, therefore, a value that varies between applications and needs to be experimentally determined by changing the parameters to arrive at a suitable value. The system deployed at the NTNU Nanolab is a dedicated 100 kV system.

Write Fields

In the ELS G-100 system, an exposure area is called a *field*, and the size of this field is defined as a single side of a simple square area with equal side lengths, i.e. a 500 μm $\times$ 500 μm field is said to have a size of 500 μm. The field is divided into *dots*, which may be thought of as analogous to pixels in a digital photograph. A field comprised of these dots is termed a *write field*. The number of dots represents the number of positions in the field that can be exposed accurately by the electron beam. A field of size 500 μm and a dot number of 50,000 dots gives the following write field resolution:

$$\frac{500\ \mu m}{50,000\ dots} = 10nm/dot. \tag{5.2}$$

This setting allows the beam position to be controlled with a resolution of 10nm.

The beam will only translate between the centers of each write field, and deflect towards the other pixels. This means that the beam exposes pixels near the edges and corners at an angle and it is, therefore, desireable to place critical parts of the pattern near the center due to increased accuracy and resolution. Additionally, using appropriate sized write fields and dot number settings is important since this sets the optics[1] of the beam to optimally expose all the pixels in the write field. The G-100 system is designed in a way to minimize the difference between centered and cornered pixels. However, this effect increases for small and dense patterns. Decreasing the beam current will decrease the actual beam spot sizes which ultimately gives an upper bound for the resolution possible. The pitch between neighboring positions in the write field should, therefore, be about the

[1] Due to similarities in working principle with optical systems, the magnetic and electrical fields that deflect and focus the beam in EBL is also termed optics

same as the actual beam spot size diameter, or slightly less (80% is a trade rule), to ensure a uniform exposure. To find the time the beam has to be positioned over each spot in the write field, Equation 5.1 is rearranged on a per spot basis as

$$t_{base} = \frac{D_{base} \cdot A_{base}}{I_{beam}} \tag{5.3}$$

where t_{base} is the exposure time of a single base/pixel in the write field, D_{base} is the desired dose, A_{base} is the area of a single base/pixel and I_{beam} is the beam current.

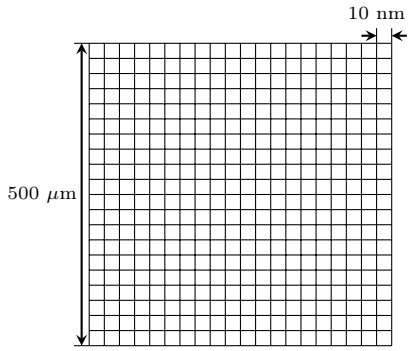

Figure 5.4: 500 μm size write field with a dot number setting of 50,000 dots resulting in a 10nm pixel/base size.

5.3.2 Electron Beam Lithography Software

The NTNU Nanolab recently acquired licenses for two EBL software packages, BEAMER and TRACER, both made by GenISys GmbH. They are powereful tools, and aid the EBL operator to optimize exposure sequencing and to choose correct parameter settings in advance of the exposure. Preparations are done outside the lab and allows the user to spend less time in the cleanroom environment, minimizing the contamination due to human presence.

TRACER – Energy and Point Spread Distribution Simulation

TRACER is an electron energy and trajectory simulation engine based on the Monte Carlo principle. The material layers, number of electrons, acceleration voltage and beam diameter, is chosen, and the software simulates the Point Spread (PID)- and energy distributions within the resist and substrate material. Figure (5.5) shows the electron trajectories of a million electrons on 100 kV system with

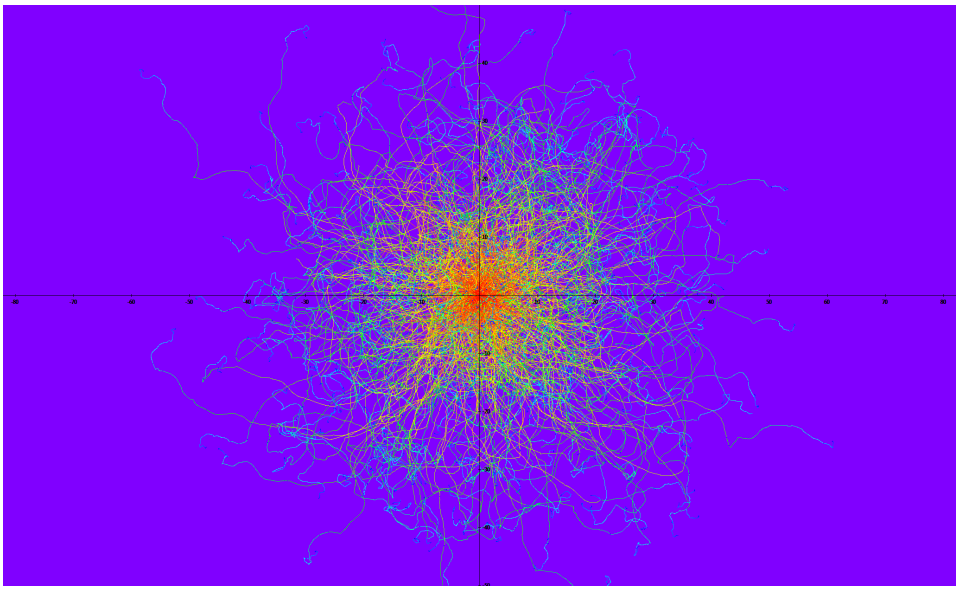

Figure 5.5: Electron trajectories resulting from TRACER simulation of 250 μm Si substrate with 100 nm PMMA resist. Elastic collisions with the substrate material increases the lateral distribution of the electrons, in which some are deflected up into the resist layer where they may deposit their energy and expose the resist in unintended areas.

a beam diameter of 1.8 nm, corresponding to a beam current of 100 pA. The substrate material chosen was a 250 μm Si substrate with 100 nm thick layer of resist from the PMMA series. CSAR62 is currently not available in the material archives, and the required parameters were not obtainable from the manufacturer Allresist GmbH. However, PMMA and CSAR are considered to be of similar nature when it comes to scattering, and it is assumed that the results obtained with PMMA simulations are transferrable to CSAR62. For 100 kV system, the forward scattering is negligible compared to the backscattering, so the substrate material is the most critical parameter of the simulation. The backscattering is visible in the figure. Elastic collisions with the substrate material increase the lateral distribution of the electrons, in which some are deflected up into the resist layer where they may deposit their energy and expose the resist in unintended areas. The results from the simulation are transferred to BEAMER, presented in the following subsection, for accurate proximity effect correction (PEC), on the pattern to be written.

BEAMER – EBL Exposure Optimization

The primary use of the software is to make exposures more efficient and to mitigate the proximity effects, mentioned in section (), related to EBL. This is a powerful tool with many capabilities, however, only a selected few where used in this work – proximity effect correction (PEC), HEAL, Multipass and separating the interior and exterior parts of large structures into bulk and sleeve regions. To correct for the proximity effects, the software runs a simulation model of the structure to be written, with parameters such as resist type, resist thickness and acceleration voltage, and uses this result to correct the dose in critical areas. No simulation for CSAR62 exist at this stage, and a simulation of PMMA was utilized due to the similarities between these resists. The HEAL function corrects the design by removing any overlaps between structures. This removal is important, because the system will interpret the overlaps as different structures, leading to a double exposure. Multipass is a function where the pattern is exposed multiple times at correspondingly lower doses for each pass. This reduces the effect of scattering and betters the resolution. To increase exposure efficiency, without compromising the resolution, a bulk and sleeve configuration was constructed within the software. In practice, this works by separating the outline of a structure (sleeve), and the interior region (bulk), and exposing them separately, usually with different doses and beam currents. The interior part of a structure doesn't require the same resolution (or dose) as the outline, and deploying this bulk and sleeve configuration may save the user little or enormous amounts of time. To avoid underexposed areas in the proximity of the bulk and sleeve interface, a small overlap between the regions was used. Figure (5.6) shows how this configuration appears in BEAMER for a bond pad and lead wire configuration.

5.3.3 Electron Sensitive Resist

A common component of all micro-/nano lithography techniques is the resist. The resists are usually polymer deposits which undergo a chemical altering upon exposure. Depending on whether the exposed areas remain or are removed after development, the resists are classified as either *negative tone* or *positive tone*, respectively. In a positive tone resist, the energy from the beam breaks down long polymer chains into smaller chains, which become soluble to a developing chemical. In a negative tone resist, the opposite occurs – short polymer chains bonds to form long, insoluble chains.

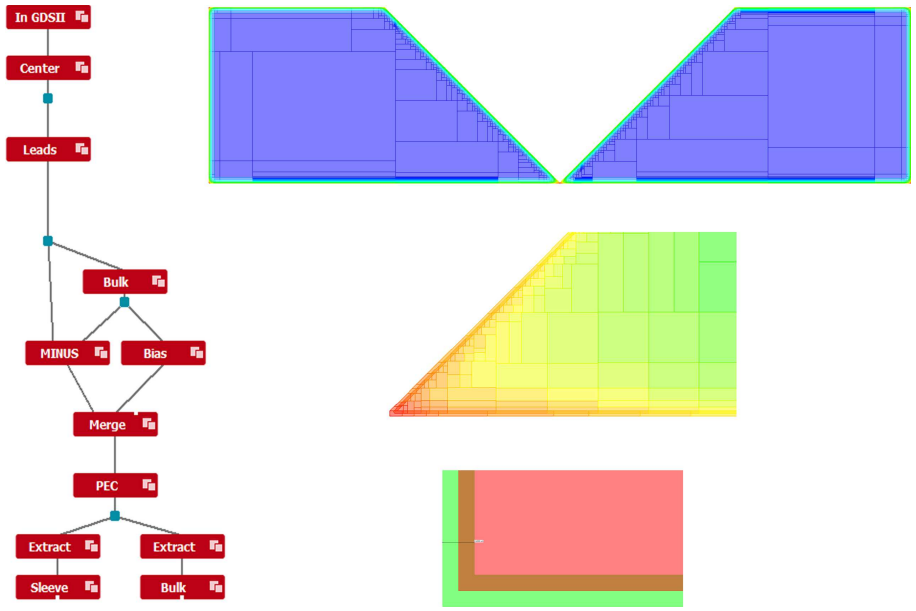

Figure 5.6: BEAMER flow diagram **Left:** Flow diagram within the BEAMER workspace where the CAD file is loaded, centered on a 2" Si wafer, split into bulk and sleeve regions, merged for performing the PEC and finally the dose-corrected bulk and sleeve are extracted and exported as separate files for exposure. **Right:** Top: View of the exposure area after PEC, different doses are differentiated by color, i.e. warm colors indicate a higher dose than cooler colors. Middle: Zoomed in view of the small scale region in the center of the lead wires where the RTD's are to be located. Bottom: Bulk and sleeve interface, with the overlap region clearly visible.

Contrast and Sensitivity

The primary characterization factors of resists are the *contrast* and *sensitivity*. Contrast may be defined as the resists ability to differentiate between exposed and unexposed areas, whereas sensitivity defines the extent of alteration in the resist material with respect to the electron beam dose [18]. To further explain contrast and sensitivity, arbitrary development curves are given in Figure (5.7) for two positive tone resists. The curves show the relationship between the exposure dose (x-axis) and the remaining resist after development (y-axis). The contrast is quantified through Equation (5.4) as

$$\gamma = \frac{1}{\log_{10} \frac{D_{100}}{D_0}} \tag{5.4}$$

where D_0 is the maximum dose value upon which the resist is unaffected, and D_{100} is the minimum dose at which all resist is removed [51]. Thus, contrast may be interpreted as the steepness of the development curve – also known as contrast curve – with D_0 and D_{100} as boundary dose values. The resist sensitivity is tightly connected with the D_0 value. It should be noted that the contrast curves illustrated in Figure (5.7) are highly simplified, and the reader is referred to Figure (5.8) for more detail. It can also be seen from this figure that the D_0 value is taken at 60% of the remaining resist thickness, so there exist some parameter variations within the industry.

High contrast resists are desirable in high-resolution patterning, because it enables developed profiles to have near vertical sidewalls and high feature aspect ratios (width to height), which facillitates pattern transfer and high-density patterns [13].

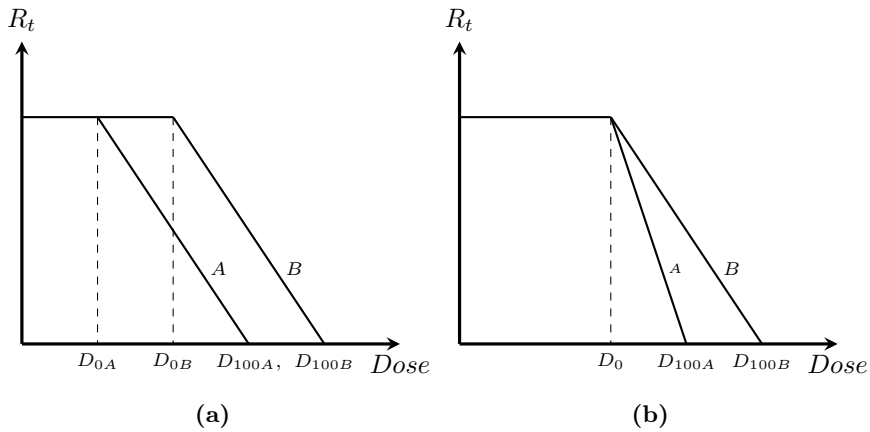

Figure 5.7: Graphical representation of the contrast and sensitivity. **(a)** Resist A and B is of the same contrast,however A is more sesitive. **(b)** Resist A is of higher contrast than B.

Resistance to Etching

Many nanofabrication techniques involve etching, i.e. selective removal of material through a mask. For a resist to function as a mask for etching steps, a high resistance to etching is desired. Etching resistance allows selective removal of material, without etching the resist, i.e. removing the mask. As previously mentioned this work does not involve etching step, and is not further discussed here.

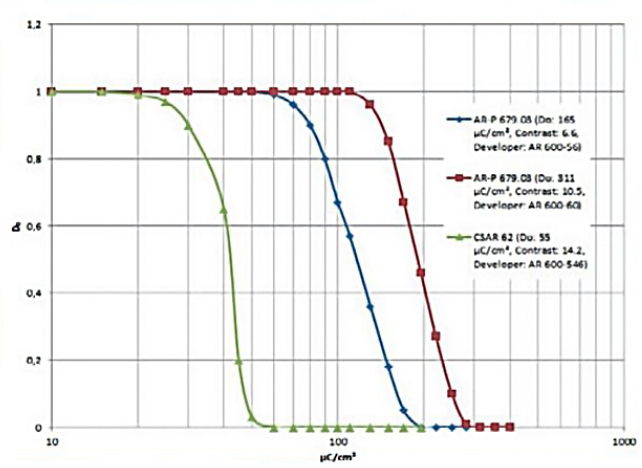

Figure 5.8: Contrast curve of CSAR62 (green), compared with two other resists from the PMMA series. As shown, CSAR62 exhibits a slightly better contrast and remarkably higher sensitivity [3].

CSAR62 – AR-P 600.13

The resist used in this work was AR-P 600.13 – popularly known as CSAR62 – produced by Allresist GmbH. It is a positive tone, high contrast, highly sensitive resist, capable of producing patterns with a resolution down to 6 nm [3]. Figure (5.8) shows the contrast curve of CSAR62 (green) compared with two positive tone resists from the PMMA series. The versatile PMMA resist is considered the most popular resist for high-resolution patterning, with desirable properties including high sensitivity, high contrast and a wide process range [46].

5.3.4 Development Using AR 600.546

Removal of the exposed areas after EBL requires a developing chemical and an additional chemical to stop the process. The developer used in this work was AR 600.546 by Allresist GmbH and IPA was used as stopper. The literature reports significant resist residue left on the wafer after conventional development with these chemicals [52], and an intermittant dip in a mixture of MIBK:IPA (3:1) was used between the developing substeps [18].

5.4 Physical Deposition Techniques

5.4.1 Spin Coating of Resist and Thickness Measurements

Spin coating is a deposition technique which allows very thin, highly controlled layers of resist to be deposited on a substrate surface. The substrate is loaded onto a stage connected to an electric motor and kept in place by pre-mounted metal pins, and vacuum suction. The resist is then deposited onto the substrate by a pipette. The operator starts a pre-created spinning recipe, where spin-time, revolutions per minute (rpm) and acceleration are the parameters. These variables affect the final thickness of the film, and *spin-curves* are provided by the resist manufacturer for tuning the parameters to produce a film of desired thickness. Spin curves for the AR-P 6200 (CSAR62) series is included in Figure (5.9).

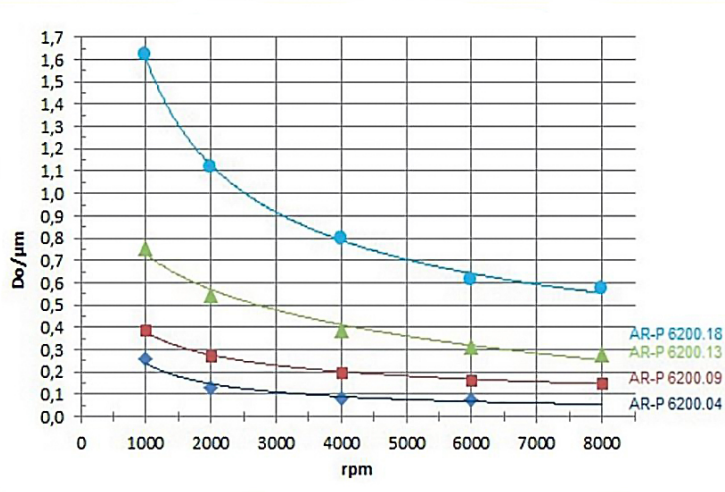

Figure 5.9: Spin curves for AR-P 6200 (CSAR62) series [3]. For AR-P 6200.13 a 4000 rpm speed setting will result in a resit layer thickness of approximately 410 nm, depending on the accelleration and time.

5.4.2 Electron Beam Evaporation

Electron Beam Evaporation (e-beam evaporation) refers to the process of boiling or sublimation of an evaporant material and the subsequent condensation of that vaporized material onto a substrate [10]. The substrate is loaded into a vacuum chamber, upside down, where various pockets, containing the deposition metals, are located at the bottom. The pockets are connected to a movable arm so that any

one of the pockets may be put into position, with the substrate located right above. An electron beam *gun* is then focused onto the pocket containing the crucible until evaporation occurs. The rising metal vapor is deposited onto the substrate, which rotates for an even distribution of the metal film. The thickness of the film is highly controlled, usually measured in kilo ångstroms (kÅ).

The *deposition rate* is defined as the time rate of change of the material deposited onto the substrate surface as

$$D_R = \frac{\Delta n}{\Delta t} \tag{5.5}$$

where D_R is the deporition rate (k/s) is the deposition thickness (kÅ) and t is time (s).

5.4.3 Resist Removal – Lift-Off

Resist removal was accomplished through the *Lift-Off*-technique. The wafer was immerged in a glass dish containing resist stripper AR-P 6200.71, which removes all the resist that is remaining after previous fabrication steps. After deposition, a uniform metal layer is covering the entire disc. In the patterned parts where the resist is developed and removed after exposure, the metal is deposited directly onto the wafer surface, however, in the un-patterned parts, the metal and wafer is separated by the resist layer. Therefore, removing all resist remaining, will leave the patterned metal device on the surface. Lift-Off with thin resist films is difficult because metal will deposit on the sidewalls of the resist remaining in the patterned parts after development. When the wafer is loaded into the deposition champer, it will never be perfectly level, resulting in a deposition on the sidewalls. If the resist layer is too thin, a continous film will cover the wafer, and lift-off will not yield a good result. However, if the patterned trench is thin enough, good results are obtainable. An aspect ratio of (1:5) is advisable for successful lift-off.

5.5 Characterization Techniques

5.5.1 Yellow Ligth Microscope

For intermediate inspections of wafer surface and patterned EBL resist a simple yellow light microscope was used. The microscope has a magnification range from $5 - 100\times$.

5.5.2 Scanning Electron Microscopy

Characterization of the RTD's was performed with a Field Emission Scanning Electron Microscope (SEM). The equipment used was an FEI APREO, which has a material dependent resolution down to 1nm at 1kV acceleration voltage. It obtains excellent contrast-to-noise ratio using its biased in-lens deflectors which pull both Secondary Electrons (SE) and Backscattered Electrons (BSE) signals in [2]. There are two mains sensors, T1 and T2, measuring BSE and SE, respectively. BSE signals are great when elemental contrasts are desired, and SE are used when topographical features, usually with a greater resolution than BSE.

5.5.3 Reflectometer

For accurate film thickness measurments after spin coating of EBL resist, a Filmmetrics F20 Flyer was used. A reflectometer uses a technique called spectral reflectance in which light reflected is analyzed, giving the film thickness and optical constants (n and k) of semiconductor and dielectric thin films [4]. The film thicknesses were found to correspond well with the spin curves provided by the manufacturer of the resists.

Chapter 6

Sample Design and Layout

In this chapter the design and layout of the test wafer is presented. The chapter begins with a brief explanation of the design conciderations utilized for smart sensor design with the main focus on maximizing the sheet resistance for high sensitivity and ends with a presentation of the final design and layout. This design will be fabricated in the NTNU Nanolab.

6.1 Design Conciderations

6.1.1 Sensitivity

The sensitivity of the RTD was presented in Chapter (TK) and may be interpreted as the slope of the resistance – temperature curve. For clarity, Equation (4.6) is restated here as

$$S = \alpha_R R_0. \tag{6.1}$$

where α_R is the Temperature Coefficient of Resistivity (TCR) and R_0 is the sheet resistance. To ensure a high sensitivity the sheet resistance should be maximized. According to Equation (3.1), the resistance is proportional to the track length, L, and inversely proportional to the crossectional area. Thus, for maximizing the sheet resistance, long and narrow wire tracks should be incorporated in the design. The thickness is deposited in the fabrication process and may therefore be controlled later. The TCR value is strictly a material property and does not apply to the design conciderations. However, De Vries [14] showed that the temperature coefficient decreased with decreasing film thicknesses, so in order to gain high

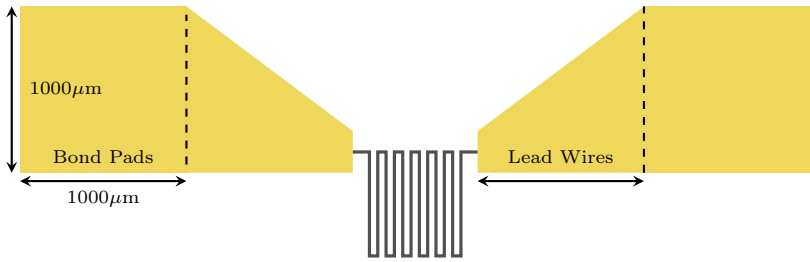

Figure 6.1: Basic configuration of a generic RTD, connected to gold lead wires and bond pads.

sensitivity sensors, maximizing the sheet resistance from a design perspective is of utmost importance.

6.1.2 Pattern

A serpentine pattern ensures a maximum track length, i.e. sheet resistance, within a specified area and is therefore the most dominant pattern in thin-film RTD designs unless the application of the sensor suggests otherwise. Recall from Chapter 2 (Section 2.3.2), where Moghaddam et al. fabricated RTD's of circular patterns in order to track the temperature and heat flux beneath expanding vapor bubbles from artificial nucleation sites. The nature of a bubble, from initial formation to departure from the surface, is radial in nature, and the use of square serpentine patterns for this purpose would have been insufficient. However, even within the radially expanding RTD array, the serpentine pattern is found. In this work, a circular serpentine pattern was designed and evaluated by the track length obtainable within a given area at a given pich between wire tracks, and compared to a square serpentine pattern. The square pattern yielded the longest track length, and is therefore concidered as a favorable pattern to ensure a maximal sheet resistance, i.e. sensitivity.

Thermal Hot Spot Mitigation

In their 2016 study, Zribi et al. [59] initially designed RTD's in a serpentine pattern with 90° bends. In order to minimize thermal hot spots within the film that would generate thermal stresses and risk of fatigue, they conducted a numerical study on the geometry of the tracks using COMSOL Multiphysics. On the basis of their analysis, they decided to reduce the angle of the bends from 90° to 45°. In the present design, smooth circular turns are deployed instead of the 45° bends used

by Zribi et al. However, no numerical study was conducted to back this up. Given that the main objective of this thesis is in regard of the fabricational aspect of RTD's, the thermal aspect of the sensor performance is not concidered any further.

6.1.3 Lead Wires and Bond Pads

The lead wires and bond pads serve as connections to the external circuit. In order for a successful connection to be made the bond pads need to be sufficiently large. For this purpose, bond pad sizes of $1mm^2$ is found to be sufficient. The lead wires serve as connections to the RTD's from the macroscale to the nanoscale. In order to minimize the lead wire resistances they are designed to be as wide as possible for as long as possible, i.e. smooth transition between the scales. For additional minimization of the lead wire and bond pad resistances, a thicker layer of gold is used. Figure (**??**) displays a crossectional view of the complete structure.

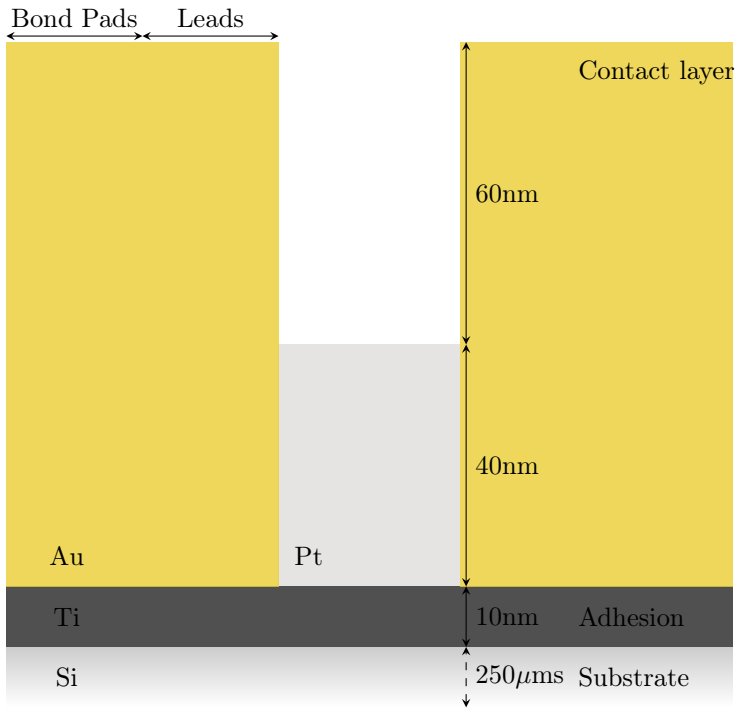

Figure 6.2: Crossectional structure of sensor on Si substrate. 10 nm Ti adhesion layer between the Si–Pt and Si–Au interphases. This figure serves only to illustrate the crossectional structure of the RTD's. Specific geometries are therefore excluded, and latteral distances are not to scale.

6.2 Design and Layout

In this section the design and layout is presented. Based on the conciderations presented so fra, six sensor variations were designed using CleWin4, a Computer Aided Design (CAD) program suitible for designing integrated circuits in the file-format required by the Elionix G-100 machine. The design of the RTD's are generic, i.e. the geometry is the same for all sizes. The 1 μm size variations were designed first, and the 2μm – 6μm variations were scaled up versions of this, i.e. by 200% - 600%, respectively. The sensors were then distributed in a 3 $\times$ 6 array, where the sizes vary between each row and the sensors are labeled according to position in this array. Table (6.1) summarizes the sensors designed with the dimensional variations approximated. In addition, the resistances are calculated from bulk material properties for comparison with later measurements.

6.2.1 Resistive Elements

The resistive elements are designed with the track width equal to the pitch between neighbouring tracks within the the pre-established sizes. This allows long wires to be fabricated, ensuring maximum sheet resistance for high sensitivity. This produces an RTD with 25 turns, equal for all sizes. Figure (6.3) displays details for the resistive elements as presented in CleWin4, and Figure (6.1) displays the generic sensor configuration including lead wires and bond pads.

(a) **(b)**

Figure 6.3: Detailed view of the resistive elements and overlap region.

(a) (b)

Figure 6.4: Layout of the test wafer as displayed in CleWin4 showing the 18 sensors in a 3 × 6 array.

6.2.2 Leads and Bond Pads

All of the bond pads are equal, measuring 1000μm × 1000μm to ensure enough space for succesful connections with the external circuit. The leads are designed in a transitional manner, collapsing from the macro- to the nanoscale. Since these components are fabricated separately from the resistive elements and have to be aligned, the lead wire widths are 20 × greater than the track width of the RTD, and an overlap of 70-80% of the corresponding sensor size is established to ensure enough margin for this purpose.

Table 6.1: Dimensions of the various designs. It should be noted that the dimensions presented here are approximated only, as the built-in functions of CleWin was found not to be reliable at this scale. Resistances are calculated for the resistive elements only using $\rho = 10.6\mu\Omega cm$ and Equation 3.1.

Label	Size	Width	Picth	Thickness	Length	A_c	Resistance
S1-S3	1 μm^2	20 nm	20 nm	40 nm	26.6 μm	800 nm^2	3525 Ω
S4-S6	2 μm^2	40 nm	40 nm	40 nm	53.2 μm	1600 nm^2	3525 Ω
S7-S9	3 μm^2	60 nm	60 nm	40 nm	79.8 μm	0.0024 m^2	3524 Ω
S10-S12	4 μm^2	80 nm	80 nm	40 nm	106.4 μm	0.0032 m^2	3525 Ω
S13-S15	5 μm^2	100 nm	100 nm	40 nm	133 μm	0.004 m^2	3524
S16-S18	6 μm^2	120 nm	120 nm	40 nm	159.6 μm	0.0048 m^2	3524

Chapter 7

RTD Fabrication

In this chapter, the RTD fabrication is presented. The final sequence of steps is summarized in section (7.1) and is the result of an iterative approach based on "Lessons learned," technological insights found in the literature and interdisciplinary collaboration and Knowledge-Sharing with the students and staff at the NTNU Nanolab where the work was done. The remainder of the chapter is dedicated to describing and discussing the challenges that were confronted, and how they were solved. When fabricating on the nanoscale, the individual steps and choices involved are not only subjectively impacting the results of that particular process but may affect the fabrication as a whole. The EBL process, for example, is not restricted to the step involving the exposure of the pattern but is part of an overall process starting with the choice of electron sensitive resist and ending with development. Three major processes are identified; (i) Wafer Cleaning, (ii) EBL and (iii) Metalization. This chapter is structured around these central processes, and will hopefully convey the content in a clear way, providing the reader with insight and appreciation to the complexity and interconnectivity of the steps which comprise the micro- and nanofabrication process.

7.1 Final Fabrication Sequence

As can be observed from the list below, the fabrication of the RTD's involves a significant number of steps. Theses may seem somewhat repetitive since the fabrication of the resistive elements, and the lead wires and bond pads have to be fabricated separately. The thin-film deposition technique used cannot differentiate between the gold and platinum areas, i.e. a thin film of uniform thickness is

deposited, and separate masks need to be utilized for the different components. Additionally, it was found that the resistive elements required a thinner layer of resist than the connective components due to significant forward scattering of the electrons in a thicker film. Figures (7.1 and **??**) display graphical representations of the steps involved in the fabrication. Only the processes which evoke a distinct difference to the substrate appearance wrt. preceding steps are included for simplicity, e.g. solvent cleaning and dry cleaning are excluded since they would graphically yield the same result. Below is a detailed list of the final fabrication sequence. Details regarding each step will be given later in the chapter. The resistive elements are numbered from 1–12, and the lead wires and bond pads from 13–23. The steps are as follows:

1. **Liquid cleaning:** 2 min ultrasonic bath in acetone, 2 min immersion bath in ethanol, rinse in IPA, blow dry in N_2 gas.

2. **Dry Cleaning:** 3 min O_2 plasma, 50% oxygen, 50% ambient air and 50% generator power.

3. **Soft Bake:** 3 min on a hot plate at 180°C.

4. **Spin Coating:** Spin coating of 100nm layer EBL resist, diluted AR-P 6200.13 in anisole.

5. **Hard Bake:** Hard baking the resist on a hot plate, 3 min at 150°C.

6. **Exposure:** Direct patterning of the resistive elements with EBL at 100kV. 100pA current and actual beam spot size of 1.8nm, write field size is 100μm with 500,000 dots and a pitch of 3.

7. **Development:** 90s development in AR 600.546, 10s immersion in MIBK:IPA, 60s immersion in IPA. Blow dry with N_2 gas.

8. **Plasma ashing:** Post development O_2 plasma ashing, 50% oxygen, 50% ambient air, 50% generator power and 30sec duration.

9. **Titanium Deposition:** Deposition of 10nm Titanium adhesion layer, 5 Å/s deposition rate.

10. **Platinum Deposition:** Deposition of 40nm Platinum resistive layer with a deposition rate of 8 Å/s.

11. **Lift-Off:** The remaining resist and excess metal is removed through immersion in resist stripper AR 600.71 until silicon surface is clear. Substrate is then rinsed with acetone, ethanol and IPA, and then blown dry using N_2 gas. This step also serves as cleaning for subsequent fabrication steps.

12. **Characterization:** Inspection of resistive elements using yellow light microscope and SEM for more detail.

13. **Dry Cleaning:** 3 min O_2 plasma, 50% oxygen, 50% ambient air and 50% generator power.

14. **Soft Baking:** 3 min on a hot plate at 180°C.

15. **Spin Coating:** Spin coating of 410 nm layer of EBL resist AR-P 6200.13.

16. **Hard Bake:** Hard baking the resist on a hot plate, 3min at 150°C.

17. **Exposure:** Direct patterning with EBL at 100kV using the bulk and sleeve configuration for lower throughput time. Sleeve was written with 5nA beam current, yielding a actual beam spot size of 3nm. Bulk was written with 50nA beam current and actual beam spot size of 25nm.

18. **Development:** 90s development in AR 600.546, 10s dip in MIBK:IPA, and immersion in IPA for 60s. Sample was blown dry usin N_2 gas.

19. **Plasma Ashing:** Post development plasma ashing for removal of any resist residue and preparing the surface for metalization. 30s O_2 plasma with 50% oxygen, 50% ambient air and 50% generator power.

20. **Titanium Deposition:** Deposition of 10nm adhesion layer, 5Å/s deposition rate.

21. **Gold Deposition:** Deposition of 100nm gold layer, for connection with the external circuit, with a deposition rate of 8 Å/s.

22. **Lift-Off:** The remaining resist and excess metal is removed through immersion in resist stripper AR 600.71 until silicon surface is clear. Substrate is then rinsed with acetone, ethanol and IPA, and then blown dry using N_2 gas.

23. **Characterization:** Inspection using optical microscope and characterization using SEM.

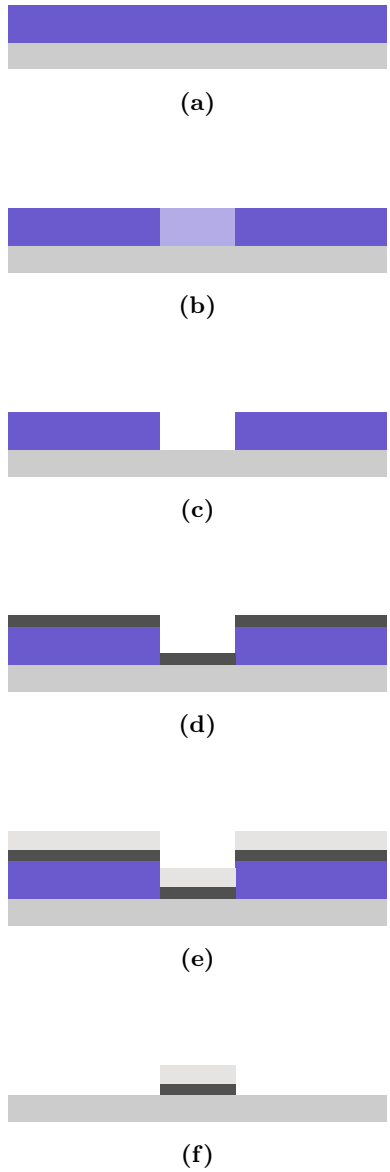

Figure 7.1: Schematic representation of the fabrication of the resistive elements. Only major steps are included, i.e. cleaning steps are excluded here since they do not contribute any visual distinction wrt. the preceding steps. **(a)** Spin coating of 100nm EBL resist on a clean Si wafer, **(b)** EBL Exposure, **(c)** Development, **(d)** Ti deposition, **(e)** Pt deposition and **(f)** Lift-Off.

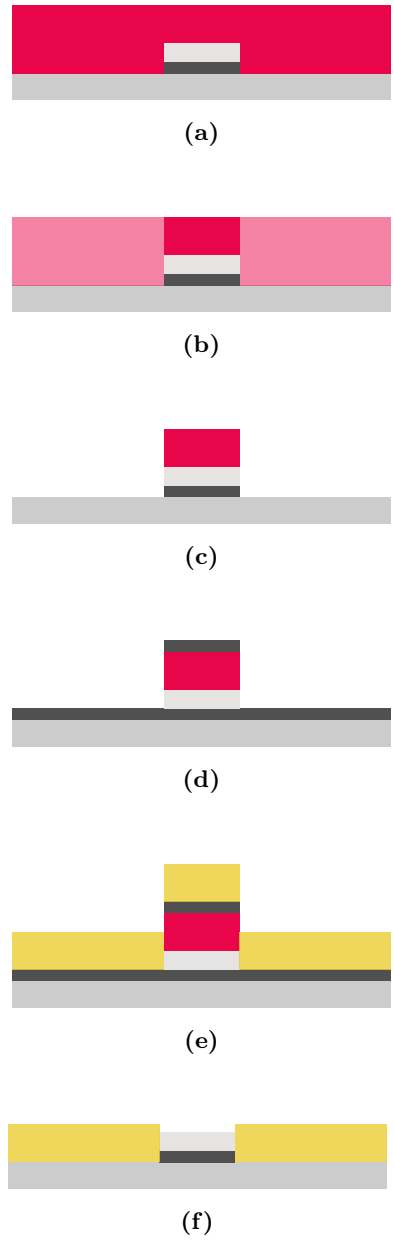

Figure 7.2: Schematic representation of the fabrication processes. Only major steps are included, i.e. cleaning steps are excluded here since they do not contribute any visual difference before and after completion. **(a)** Spin coating 410nm EBL resist on clean substrate, **(b)** EBL Exposure, **(c)** Development, **(d)** Ti deposition, **(e)** Au deposition and **(f)** Lift-Off.

7.2 Process I - Wafer Cleaning

The first step of fabrication of the RTD's is cleaning of the substrate. The cleaning setup and the equipment used, includes glass containers, solvents, HSE equipment (protective goggles), a timer, microfiber wipes and tray-holder for submerging the glass into an ultrasonic bath. The solvents are filled into the glass containers where the wafer is later introduced, and the timer tracks the time in each container. Manipulation of the wafer between containers is done with a simple plastic tweezer. Metal tweezers were very early on abandoned as these may scratch the surface and introduce metal residues. Drying was performed by laying the wafer flat on a microfiber wipe to increase friction so that the wafer doesn't blow away by the forced flow of N_2 gas. After the cleaning was complete, the remaining solvents were disposed of in appropriate waste containers.

7.2.1 Solvent Cleaning

The initial cleaning procedure consisted of a ten-second soak in acetone and continuing with acetone rinsing after removing the wafer from one of the glass containers. Immediately afterward, the wafer was rinsed with ethanol, without allowing the acetone to evaporate, before rinsing with IPA followed by De-Ionized Water. The wafer was then blown dry using room tempered N_2 gas until droplets were no longer visible. This cleaning procedure resulted in unsatisfactory results, which became evident after spin coating of the EBL resist, revealing small imperfections and particulate contaminations between the wafer and resist film. Defects in the resist film may cause problems in the EBL patterning if the pattern coincides with a contaminated area. Considering that the RTD designs are small, it is highly unlikely that this will happen if the number of these areas are low. However, they were found to be severe enough to investigate alternative cleaning procedures. The sequence of the solvents was not the issue, as they are introduced according to chemical purity considerations. IPA is considered purer than ethanol, and ethanol, in turn, more purified than acetone. However, the literature revealed that IPA is used as a drying agent in the industry (see Chapter (5.2.1)), as allowing the water rinsed wafer to dry by its own will leave watermarks. The use of N_2 gas in the wafer drying is a preferred technique which inhibits the formation of these marks, with less chance of recontamination. However, hot gas is required [42]. An attempt of combining the *Marangoni drying* technique with blow drying in N_2 gas was tried with satisfactory results. Experiments with ultrasonication were also tested, and after completely abandoning the DIW, excellent results were obtained with a combina-

tion of ultrasonic acetone bath for two minutes, two-minute immersion in ethanol and N_2-assisted IPA rinsing and drying. The function of the DIW is to remove any organic material from the solvents, but considering that an O_2 plasma dry cleaning is used as an additional cleaning step; the DIW was deemed unnecessary. Table (7.1) summarizes the cleaning iterations, where the bottom one is the final one. It should be noted that all cleaning was done with room tempered solvents ($\sim 21°C$), and no experimentation at elevated temperatures was performed.

Table 7.1: Different cleaning procedure iterations during the fabrication process. Best results was obtained with the two minute ultrasonic bath in acetone, followed by a two minute immersion in ethanol and finally IPA rinsing with N_2-assisted drying. DIW was completely abandoned in the final cleaning procedure.

Acetone	Ethanol	IPA	DIW	N_2
10 s soak and rinse	rinse	rinse	rinse	blow until dry
2 min immersion	2 min immersion	rinse	rinse	blow until dry
2 min immersion	2 min immersion	rinse	-	blow until dry
2 min ultrasonic immersion	2 min immersion	rinse	-	blow until dry

7.2.2 O_2 Plasma Dry Cleaning

An O_2 Plasma Dry cleaning procedure was deployed for the removal of any organic material that might be remaining on the wafer surface after the solvent cleaning. A standard setting of 50% O_2 gas and 50% generator power was used throughout the entire process. The removal rate of the organic material of the plasma cleaner used was not available. However, a rough estimate was calculated by etching EBL resist CSAR62 and measuring the resist thickness before and after. An etch rate of $\sim 20nm/s$ was estimated, and therefore a plasma cleaning duration of 3 min was considered to be satisfactory.

7.3 Process II - Electron Beam Lithography

The second process of the fabrication is the Electron Beam Lithography. This process covers the EBL resist, spin coating, curing, exposure, and development. These steps are highly interconnected. The choice of resist, through its sensitivity and contrast, decides the dose that needs to be delivered by the electron gun. However, the sensitivity of the resist may be profoundly altered by the developing chemical. In this work, no alternative resists or developers were considered, and the scope of the results pertain only to the chemicals covered. Figure (7.4) displays the sub-steps of the EBL process for both resistive elements (a to c) and the lead wires and bond pads (d to f). Layers are indicative only, i.e. not to scale.

7.3.1 Electron Sensitive Resist

The resist used in this work was AR-P 6200.13 (CSAR62). However, the viscosity of this polymer allows for a minimum thickness of approximately 275 nm (see Figure 5.9), and for the desired thickness of ∼100 nm, a diluted version of CSAR62 in anisole was used. Diluted CSAR62 was generously provided by Ph.D. Student Einar Digernes, who encountered the need for thinner resist layers in his work. For the lead wires and bond pads, conventional CSAR62 was used.

7.3.2 Spin Coating

Coating of the EBL resist was performed with a spin coater under a fume hood. Table (7.2) summarizes the spin-programs for the designated thicknesses. Before spin coating, the cleaned wafer was baselined in a reflectometer for film thickness measurements. The recipes consistently produced the expected film thicknesses, with a marginal error of approximately $+/- 2\ nm$. After the spin coating program was completed the wafer was removed, and the back side of the wafer was inspected for unwanted resist. It was found that resist consistently, to som degree, found its way to the backside, mostly on the edges. Resist on the back side of wafers may introduce contamination to machines that are used later in the fabrication process. Also, this residue might result in a slight wafer tilt when loaded into a machine, which may cause issues when high precision on the nanoscale is desired. It is, therefore, highly beneficial for all users of nano lab equipment to remove resist residue that would otherwise be in direct contact with stage surfaces in the various equipment. A resist stripper, AR 6200.71, was used for removal of this residue. A small amount of the stripper was filled into a glass container, and a pointed swab was used for the resist removal at the back edges. Immediately after, the resist

coated wafer is placed on a hot plate at $150°C$ for three minutes for curing and evaporating solvents present in the resist mixture.

Table 7.2: Each spin program is divided into two stages, a three second aceleration stage up to 1000 rpm, and then a 60 second stage which ensures the desired film thickness.

Thickness	Time	rpm	Acceleration
100 nm	3 sec	1000	1000
	60 sec	2000	1000
410 nm	3 sec	1000	1000
	60 sec	4000	1000

7.3.3 EBL Exposure

The EBL exposure is divided into two subsections: (i) pre-exposure preparations and (ii) exposure procedure. The preparations are done outside the laboratory to ensure that the machine is solely used for writing during booking hours and to lower contamination due to human presence in the cleanroom environment.

Pre-Exposure Preparations

To increase throughput time and maintain resolution for the lead wires and bond pads, BEAMER was used to separate the interior and exterior part of these components into bulk and sleeve regions. These were then exported as individual files and written separately with different beam currents. The write field size and resolution are also determined here. This is important since it here the machine is set up for maximal patterning resolution. A rule of thumb is that the resolution of the write-field should be 80-100% of the actual beam spot size. Table (7.3) summarizes the Write Field Resolution (WFR) requirements according to the 80% rule for each corresponding beam current and the WFR obtainable. The dot number setting is limited by default which restricts an ideal setup. However, the pitch may be adjusted so that the resolution becomes acceptable. Figure (7.3) displays the write fields used corresponding to the resistors, sleeve, and bulk, respectively. The dark shaded areas indicate where the beam is pointed, and the lightly shaded areas are the contribution of the pitch to the WFR. For the resistors, a pitch of three was used, but for the sleeve and the bulk, this was not necessary. The bulk resolution was readily obtainable according to the 80% rule and the sleeve resolution coincided with the beam spot diameter, which was considered sufficient.

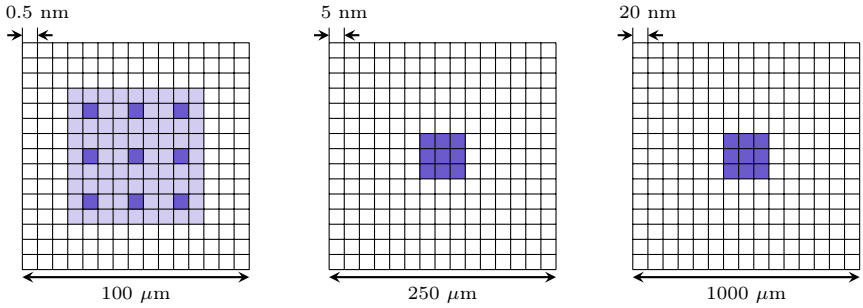

(a) Resistors. **(b)** Sleeve. **(c)** Bulk.

Figure 7.3: Write field resolutions with 200,000 and 50,000 dots (b and c), respectively.

Exposure Procedure

The Elionix G-100 machine is separated from the rest of the cleanroom by a glass enclosure for additional protection against contamination and maintaining a stable environment. Before loading the wafer into the machine, the predetermined beam current was recalled from a beam-memory for it to stabilize. Depending on the beam used by the previous operator, this takes approximately five to 20 minutes. In the meantime, the wafer was loaded into the machine as instructed during training, after which the separate enclosure was exited, as the main work is done remotely from a computer on the outside. Usually, the loading time is enough for the beam to stabilize. The beam current was then measured by moving the beam to a Faraday cup where a pico ampermeter is available. After the beam current is satisfactory, the beam needs to be focused and astigmatism corrected. Astigmatism may be thought of as distortions in the roundness of shapes. To correct for these parameters the beam is translated to a reference containing grains of various sizes and rounded shapes. After adjusting the focus and astigmatism, the beam current may have drifted, so a new beam current recording is needed. The process of adjusting the

Table 7.3: Beam currents and corresponding diameters, WFR's according to the 80% rule, obtainable and effective, respectively.

Component	Beam Current	Beam Diameter	Dose	$WFR_{80\%}$	WFR_o	Pitch	WFR_e
Resistors	100pA	1.8nm	300	1.44nm	0.5nm	3	1.5nm
Sleeve	5nA	5nm	300	4nm	5nm	1	5nm
Bulk	50nA	25nm	300	20nm	20nm	1	20nm

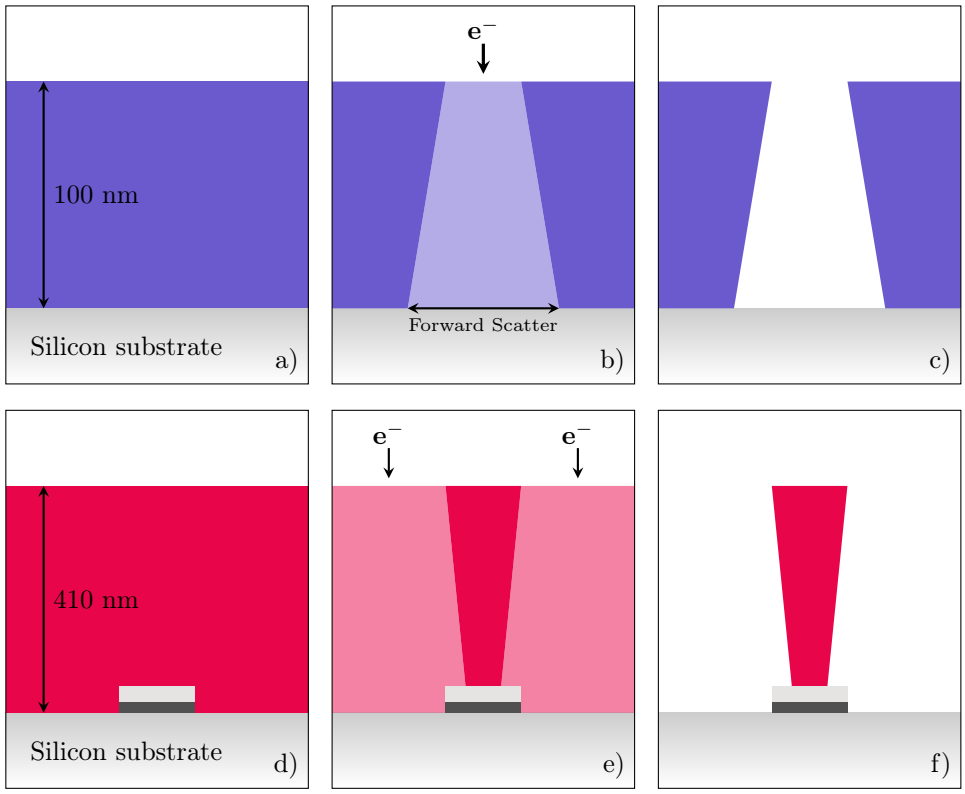

Figure 7.4: Schematics of the EBL process, starting with the spin coated wafer at the left, exposure in the middle and development at the right. The top row illustrates the EBL process for the resistive elements, using 100nm resist film thickness, and the EBL process for the lead wires and bond pads, with 410nm resist film, at the bottom.

beam current, focus and astigmatism take a few iterations.

When the beam settings are satisfactory, the writing schedule file is created from the externally prepared files and the exposure is executed.

7.3.4 Development

The patterned wafer was developed using developer AR 600.546 (by Allresist GmbH), with an intermediate dip in MIBK:IPA for resist residue removal, and stopping the development in IPA. The developer and development time may severely alter the resist sensitivity, and, therefore, there exists an optimal development procedure, pertaining to the specified pattern produced by an EBL exposure at a given acceleration voltage, beam current and area dose. The development procedure may vary

from the choice of developing chemicals, temperature and development time. In this work, only AR 600.546 was used, and development iterations were only varied by changing the development time. Table (7.4) summarizes the development iterations. No significant differences between the development schemes was found, and a 90-second development was used as it was easier to control the development at the longer time intervals, however, with AR 600.546, small variations in development time cause minor differences.

Table 7.4: Development iterations. No significant difference, as AR 600.546 provides a wide operating range. Different result might be obtained by using other developers, e.g. AR 600.548, or different development temperatures, however, this was not attempted.

AR 600.546	MIBK:IPA	IPA
30 seconds	10 seconds	30 seconds
60 seconds	10 seconds	60 seconds
90 seconds	10 seconds	90 seconds

7.4 Process III - Metalization

The metalization process consists of three sub-steps; (i) O_2 Plasma Decumming, (ii) Thin-Film Deposition and (iii) Lift-Off.

7.4.1 O_2 Plasma De-scumming

Even though the ten-second dip in MIBK:IPA considerably removes resist residues of CSAR62, any remaining resist will contribute to poor adhesion in the metal deposition stage. Therefore, an O_2 plasma de-scumming process is deployed. The de-scumming is done with 50% O_2 value and 50% generator power for 30 seconds, which etches approximately 10 nm of organic material. This is considered sufficient for removal of resist residues and small enough for keeping the resist thickness intact.

7.4.2 E-Beam Thin-Film Deposition

The deposition of the thin metallic films is performed through an e-beam evaporation. The wafer is mounted onto a sample holder which is loaded upside down into a load-lock. The load-lock is separated from the main chamber which is kept at a vacuum below 1.5e^{-6} Torr. Before loading into the vacuum chamber, the load-lock, which is at atmospheric pressure when the wafer is mounted, is pumped down to equalize the pressure differences. When the pressure is sufficiently low, a gate valve is opened which connects the two chambers. The sample holder is attached to an arm which is driven into the main chamber by a magnetic slider. Once inside, the sample holder is picked up by a designated suspender which is lowered into position from the outside. When the stage is properly detached from the sample holder, the arm is retracted, the gate valve closed and the sample is ready for deposition.

The desired cruicible pocket is manually put into place, and the corresponding material is selected on a control panel. This ensures that apropriate power is delivered to the cruicible for efficient sublimation. The deposition recipe is also manually entered in the control panel, which consists of the final desired thickness and the deposition rate. A 5 Å/s deposition rate is recommended by default.

During the fabrication process there was a great deal of issues with this particular step. After deposition of the platinum thin-films, an uneaven surface was experienced, indicating that the resist had boiled during the procedure. To avoid these issues it is recommended that the substrate is loaded on top of a highly conducting material wich act as a heat sink, driving heat away from the substrate.

This material may either be a metal plate, such as alluminium or a thermal paste. Another approach is to increase the deposition rate, ultimately lowering the deposition time and inhibiting boiling from initiating. The second approace was attempted and found satisfactory.

Table 7.5: Thin-Film Deposition Parameters. Deposition times are calculated from the thickness and rates. In practice, deposition times will vary slightly, as the deposition rates are not perfectly stable, i.e. they fluctuate throughout the process.

Component	Target	Power	Voltage	time	thickness [kÅ]	rate [Å/s]
RTD	Ti	-	8.90	20s	0.100	5
	Pt	-	8.90	41s	0.400	8.5
Contacts	Ti	-	8.90	20s	0.100	5
	Au	-	8.90	125s	1.000	8

7.4.3 Lift-Off

The remaining resist after deposition was stripped through a Lift-Off procedure using resist stripper AR 600.71 (by Allresist GmbH) poured into a glass container. Initially, the wafer was submerged and left overnight to dissolve all of the resist. A significant amount of resist remained between the tracks of the resistive elements, and a ultrasonically assisted Lift-Off procedure was introduced with great success. This also eliminated the risk of the stripper to evaporate during the night, if not sealed properly, as the ultrasonication considerably reduces the Lift-Off duration.

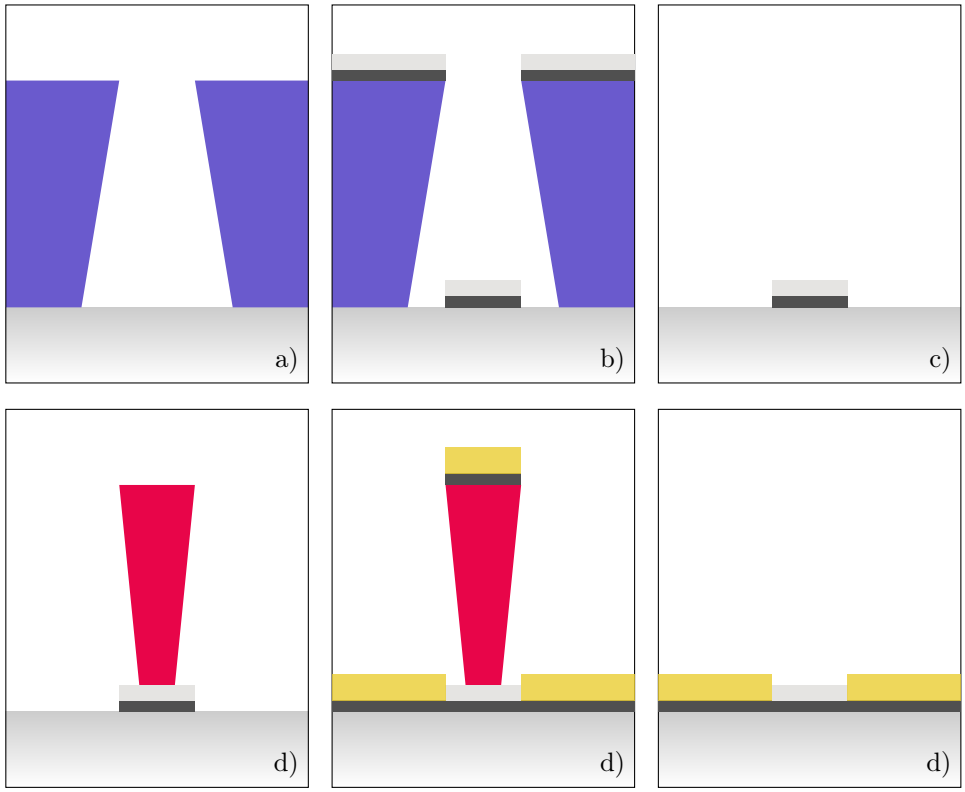

Figure 7.5: Schematic representation of the metalization process, starting with the developed mask at the left, thin-film deposition in the middle and Lift-Off on the right. The top row illustrates the metalization process for the resistive elements, and the bottom displays this process for the lead wires and bond pads.

Part III

Results and Discussions

Chapter 8

Results and Discussions

In this chapter the results from the fabrication is presented and discussed. The results may be divided into three parts; (i) the fabrication process, (ii) the RTD's and (iii) the sensor resistance measurements. The fabrication process is given in detail in Chapter (7).

8.1 Results: Fabrication Overview

Figure (8.1) displays an overview of the RTD's obtained with the fabrication process presented in Chapter 7. The images are captured with a FEI APREO electron microscope at 10.00 kV acceleration voltage and 0.10 nA beam current. Since the sensors are indistinguishable when properly magnified, the overview images are all taken at a fixed 5000× magnification for the display of the sensors true differences – their sizes. The final batch of sensors consisted of 18 individual RTD's, including lead wires and bond pads, in six different size variations.

The dark areas in the images are caused by the SEM. Small particles found on the structure surfaces was used as focus points for obtaining the high resolution images, and as a result the beam made the these areas so negatively charged that there were significant accumulation of carbon. However, these dissappear after a while, leaving only a visual impact in the images.

In the following sections detailed images of each RTD is presented. In the final stages of this thesis, it was found that the detailed images of the 1 μm size variation were missing and due to the loss of access in the cleanroom, no detailed image was obtained. Therefore, a preliminary image, before the bond pads and lead wires had been deposited, is included.

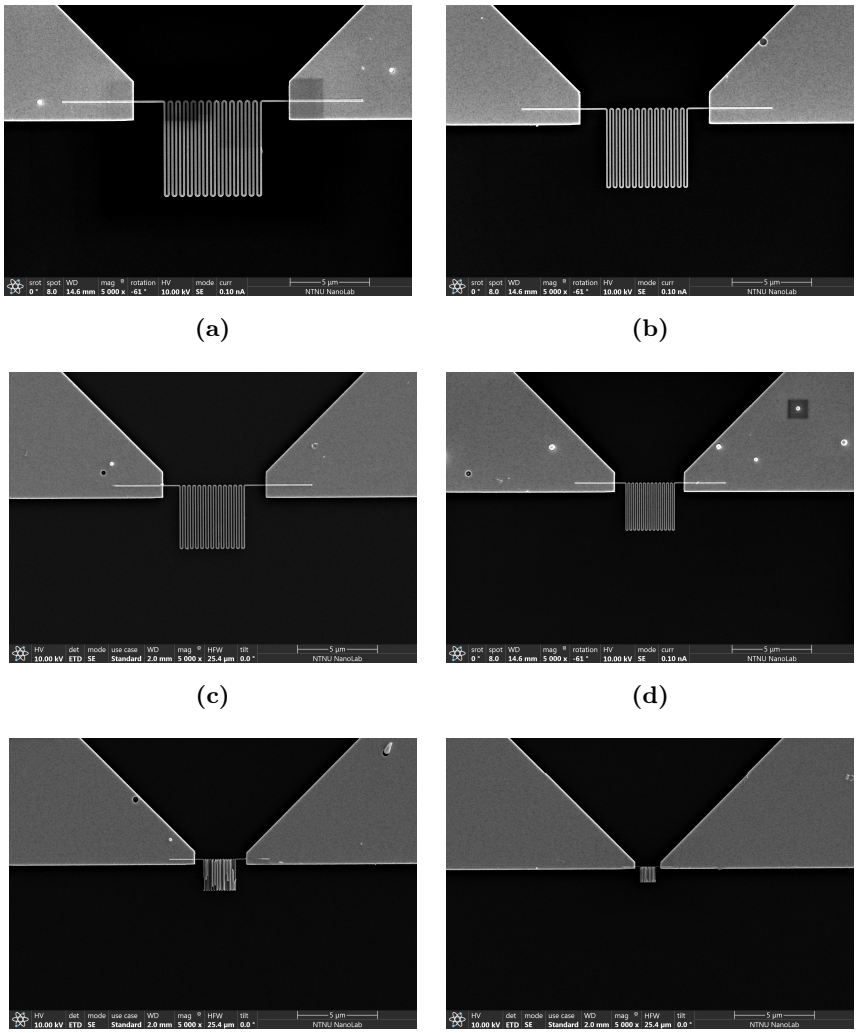

(a) **(b)**

(c) **(d)**

(e) **(f)**

Figure 8.1: Overview of the results - (a) to (f) from $6\mu m^2$ to $1\mu m^2$, respectively. Photos are taken with a FEI APREO at 10.00 kV, 0.10nA beam current and 5000× magnification for displaying the size variations.

8.2 Results: 6 μm Details

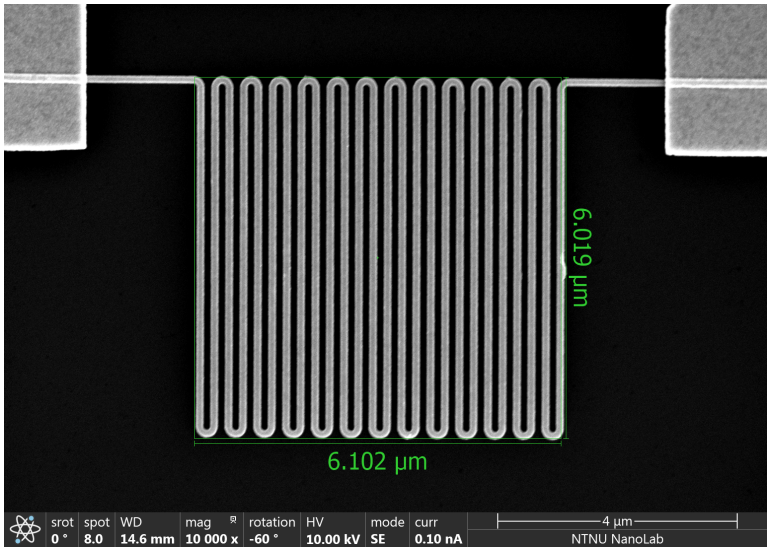

Figure 8.2: S17 – 6$\mu m\times$ 6μm – 120nm track width.

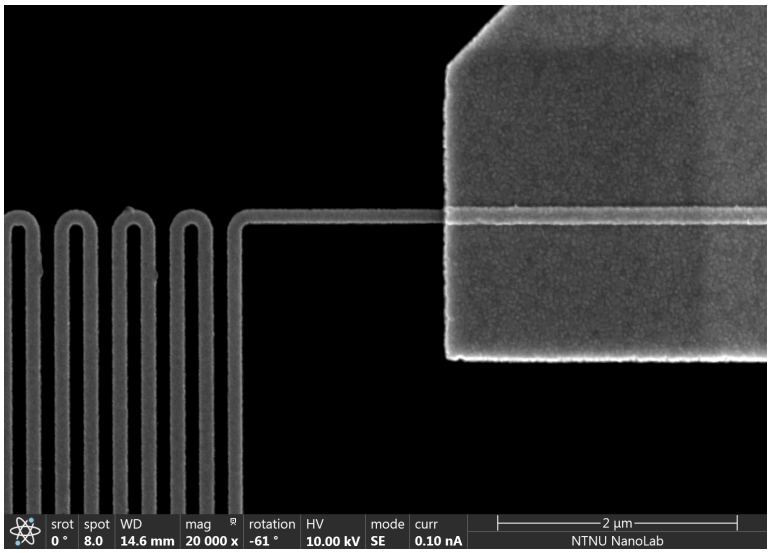

Figure 8.3: S18 connection to the lead wire. Shaded area showing carbonization from the e-beam.

8.3 Results: 5 μm Details

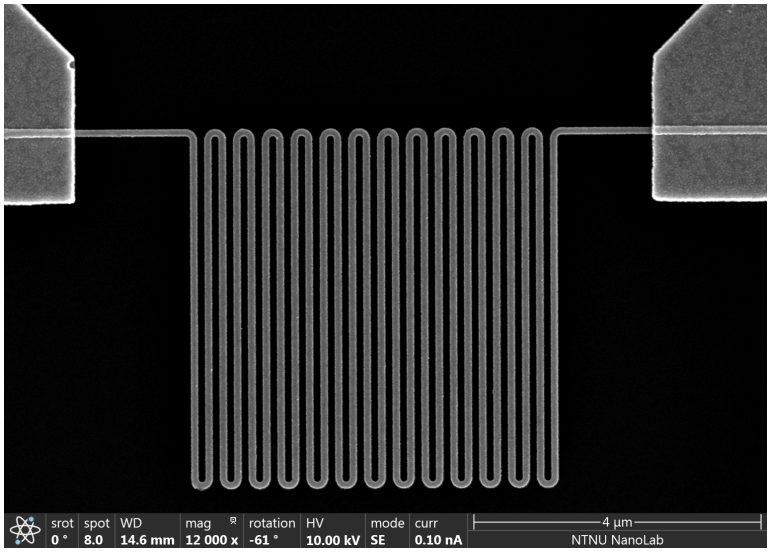

Figure 8.4: S15 – $5\mu m\times$ 6μm – $100nm$ track width.

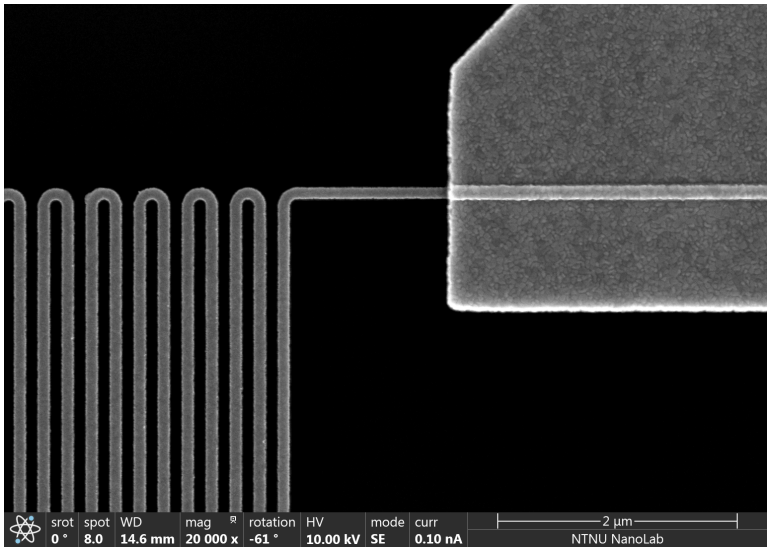

Figure 8.5: S15 connection to the lead wire.

8.4 Results: 4 μm Details

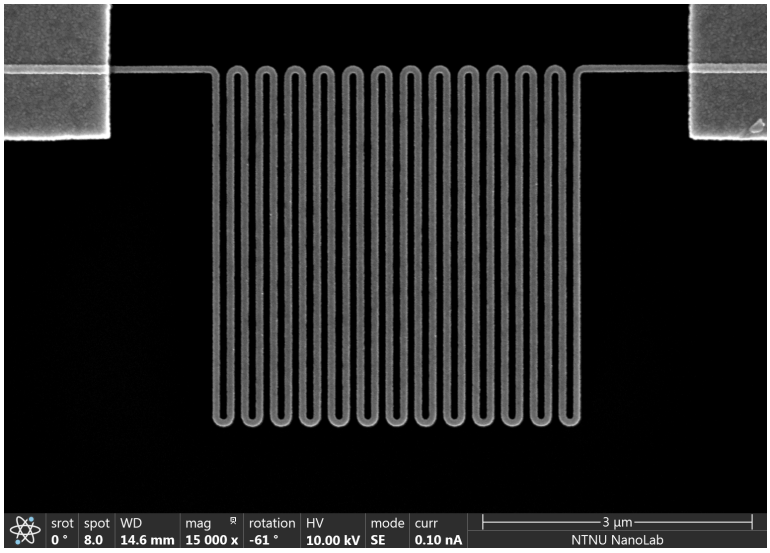

Figure 8.6: S12 – $4\mu m\times$ 4μm – 80nm track width.

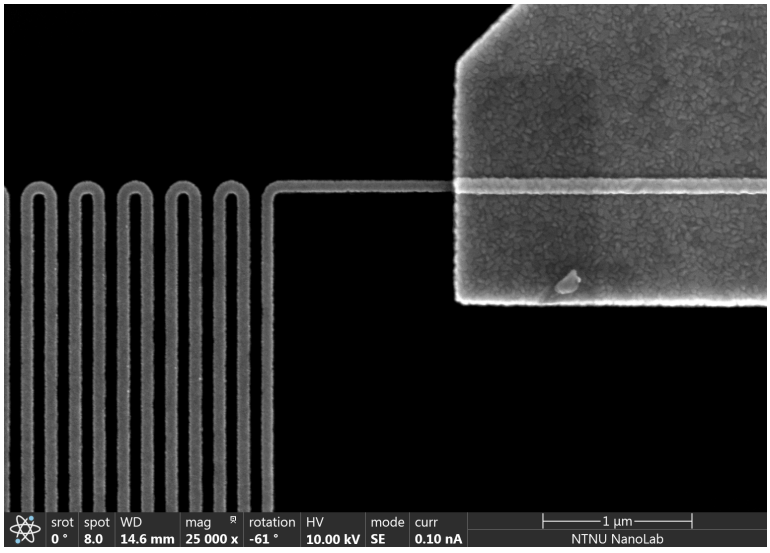

Figure 8.7: S12 connection to the lead wire.

8.5 Results: 3 μm Details

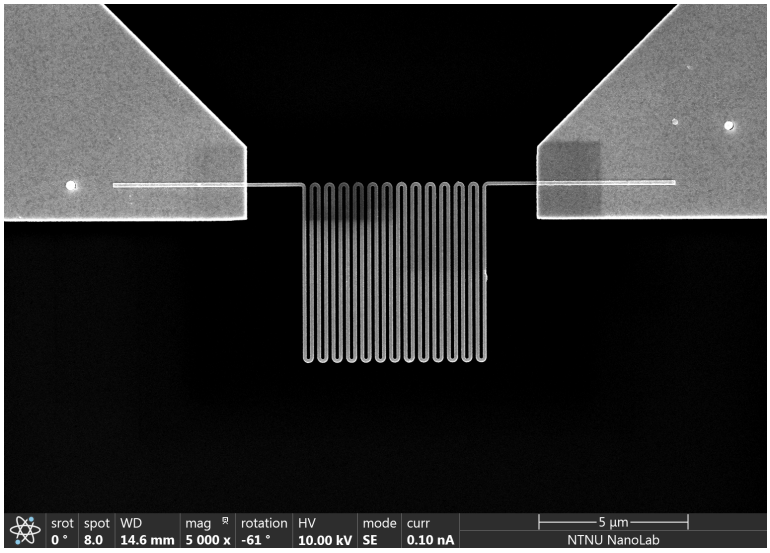

Figure 8.8: S8 – $3\mu m\times$ 3μm – $60nm$ track width.

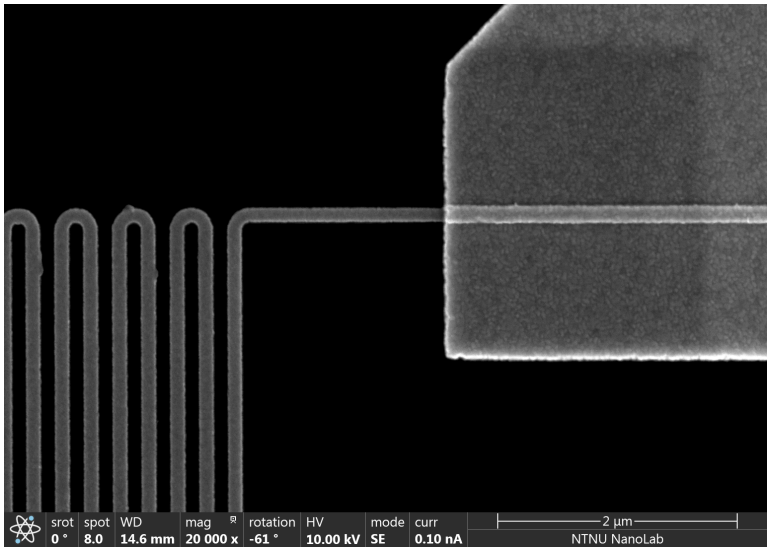

Figure 8.9: S8 connection to the lead wire.

8.6 Results: 2 μm Details

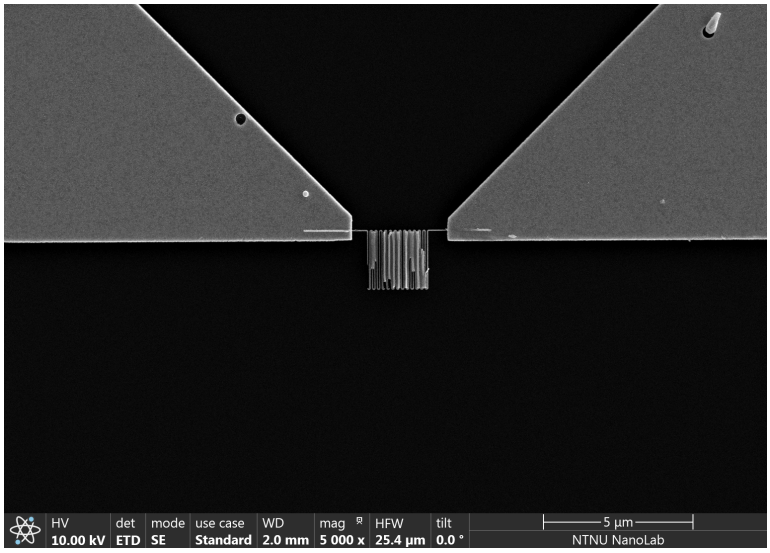

Figure 8.10: S5 suspended between the lead wires.

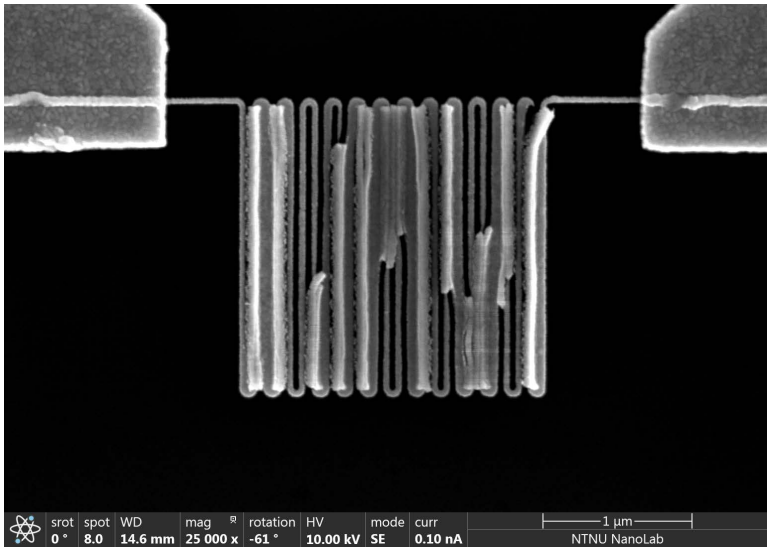

Figure 8.11: S5 – 2$\mu m\times$ 2μm – 40nm track width.

8.7 Results: 1 μm Details

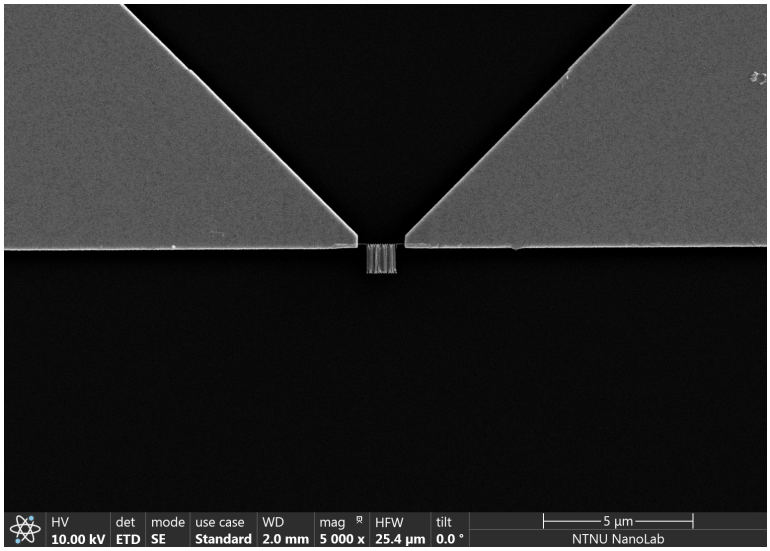

Figure 8.12: S2 – suspended between the lead wires.

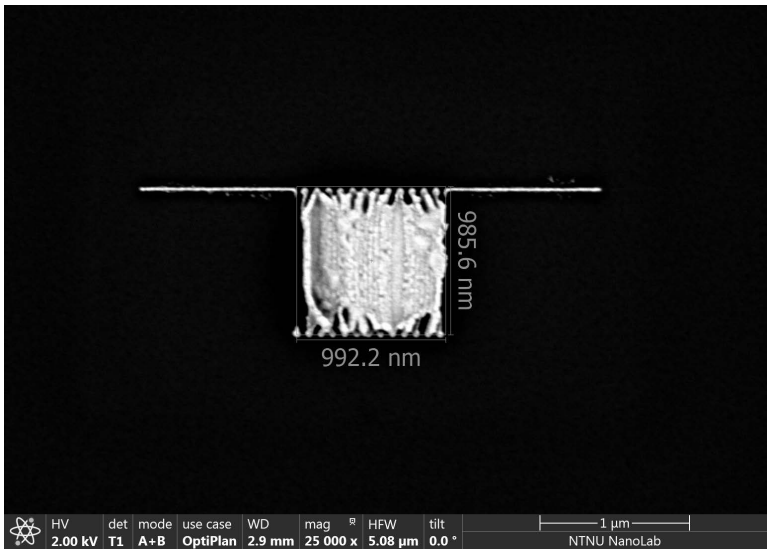

Figure 8.13: Detailed view of the 1 $\mu m \times 1$ μm variation, here without lead wires and bond pads.

8.8 Discussion: Fabrication

8.8.1 Validity of the Beam Currents and Their Spot Sizes

During the fabrication, it was found that the correspondance between the beam currents and the actual beam spot sizes was inconsistent between the various tool documentations. For example, the 50nA current had a reported beam spot diameter of both 25nm and 90nm in two different manuals. It was reported to the senior engineer who determined that the 25nm beam was correct. However, other inconsistencies was uncovered and the whole beam diameter – beam current relationship needs to be re-evaluated. The beam spot size is highly important when fabricating on the nanoscale since it needs to correspond with the write field and pre-exposure setup.

8.8.2 Alternative Fabrication Procedure

The fabrication procedure presented in this work can be viewed as a bottom-up approach, i.e. a mask is initially constructed and the metallic thin-films are deposited directly on the substrate in the desired pattern. A top-down approach, involving the deposition of the metallic thin films as an initial step, and then deploying a negative tone resist for the construction of an etching mask, might be an alternative. This procedure would involve the introduction of additional substrate layers into the EBL, and for this the impact regarding backscattering have to be examined. Since these layers are thin compared to the Silicon substrate it is expected that these effects are negligible. However, due to the significantly higher atomic number of platinum and gold over silicon, these effects should be investigated before an attempt is made. Gold, especially, is considered a contaminent in many nanofabrication procedures and the effects of these should be verified in advance of any attempt.

The main advantage by concidereing both apporaches is the wider range of EBL resists available. By being able to use both negative and positive tone resists, the chance of selecting the most beneficial one with respect to contrast and sensitivity is the greatest.

8.9 Results: Resistance Measurements

After fabrication the resistances of the RTD's were measured with a simple multimeter inside the cleanroom environment. The results are summarized in Table (8.1) and show that the measured resistances differ by 79.4% from the calculated resistances using bulk material behaviour for platinum, i.e. $\rho = 10.6\mu\Omega cm$. The lead wire resistances are not taken into account here, and the measuring current in the multimeter is unknown. The 1 μm and 2 μm size variations were unsuccessfully fabricated and no measurments were obtained.

Table 8.1: Resistance measurments compared with the calculated values using bulk material properties.

Size	Label	Measurement [Ω]	Calculation [Ω]	Δ
1 μm	S1	-	3525 Ω	-
	S2	-	3525 Ω	-
	S3	-	3525 Ω	-
2 μm	S4	-	3525 Ω	-
	S5	-	3525 Ω	-
	S6	-	3525 Ω	-
3 μm	S7	718 Ω	3524 Ω	-79.6%
	S8	791 Ω	3524 Ω	-77.6%
	S9	737 Ω	3524 Ω	-79.1%
4 μm	S10	704 Ω	3525 Ω	-80.0%
	S11	705 Ω	3525 Ω	-80.0%
	S12	729 Ω	3525 Ω	-79.3%
5 μm	S13	716 Ω	3524 Ω	-79.7%
	S14	723 Ω	3524 Ω	-79.5%
	S15	726 Ω	3524 Ω	-79.4%
6 μm	S16	0.26 Ω	3524 Ω	-99.99%
	S17	724 Ω	3524 Ω	-79.4%
	S18	724 Ω	3524 Ω	-79.4%

8.9.1 Discussion: Resistance Measurements

The resistance measurements reported in Table (8.1) and the deviations from the calculated resistances based on the design and bulk material behaviour is expected and in accordance with previous results found in the literature. Even so, sufficiently high resistances have been obtained, exceeding the results by Zribi et al. [59] by approximitaly 200 Ω at several orders of magnitude lower sizes.

The mean sheet resistance and standard deviation are calculated to be 727 Ω and 3.2%, respectively. The high sheet resistance is highly desirable as it aleviates the accuracy required by the measuring circuit. The low standard deviations suggests that the sensors may be calibrated in bulk, eliminating significant amount of time by calibrating the sensors one by one.

8.10 Future Work

The work in this thesis have mainly been devoted to the investigation of the fabricational limits regarding RTD's. Proposal for future work is summarized in this section.

1. **Electrical Characterization:** The RTD's have to be electrically characterized. This involves calibrating the sensors and establishing the measurment errors caused by lead wire resistances and self-heating errors.

2. **Sensor Characteristics:** Sensor characteristics such as thermal response time, accuracy and precision needs to be established.

3. **Implementation of four-lead wires:** To fully eliminate the measurement error caused by the lead wire resistances, two additional wires has to be incorporated in the design.

4. **Construction of heat-flux sensors:** Heat-flux sensors may easily be obtained by depositing the temperature sensors on each side of a thermal insulator.

Chapter 9

Conclusion

This work has been motivated by the urgent need for localized temperature and heat-flux measurements in microchannel heat sinks, with special emphasis on channels utilizing two-phase flow boiling heat transfer. For this purpose, the smallest RTD's in the world have been obtained. The main objectives of this thesis was to investigate the manufacturability of resistance temperature detectors in the range of 1 m^2 – 6 μm^2 and (II) develop a method for the fabrication of these sensors.

Sensor designs of six sizes, i.e. 1 μm^2 – 6 μm^2, have been presented and fabricated, in which the 3 μm^2 – 6μm^2 variations were obtained with great results. The mean resistance and standard deviation has been calculated to 727 Ω and 3.2%, respectively. The resistances indicate that high sensor sensitivites are obtainable, alieviating the accuracy requirements in the external measuring circuit. The low standard deviation suggests that the sensors may be calibrated in batches, which simplifies this precedure enormously when a large amount of sensors are to be used.

The size and shape of the sensors can be modiefied according to the specific need, i.e. width of the channel, and may be distributed in both axial and latteral directions, thoughout the entire range of the microchannel class. The RTD's may readily be turned into heat-flux sensors by depositing the devices on each side of a thermal insulator.

Future work has been identified, including electrical and operability characteristics, four-lead wire implementation and the construction of heat-flux sensors.

Bibliography

[1] Intel 4004. https://en.wikipedia.org/wiki/Intel_4004. Accessed (2017-06-22).

[2] Sem apreo (1341). http://ntnu.norfab.no/WebForms/Equipment/EquipmentView.aspx?toolId=96. Accessed (2017-06-07).

[3] Positive e-beam resists ar-p 6200 (csar 62). http://www.allresist.com/wp-content/uploads/sites/2/2016/12/allresist_produktinfos_ar-p6200_englisch.pdf. Accessed (2017-06-02).

[4] Reflectometer (1500). http://ntnu.norfab.no/WebForms/Equipment/EquipmentView.aspx?toolId=10. Accessed (2017-06-07).

[5] History of processor performance. http://www.cs.columbia.edu/~sedwards/classes/2012/3827-spring/advanced-arch-2011.pdf. Accessed (2017-06-22).

[6] Elsg-100. http://www.sts-elionix.com/node/23. Accessed: 2017-06-05.

[7] The story of the intel® 4004. https://www.intel.com/content/www/us/en/history/museum-story-of-intel-4004.html. Accessed (2016-06-22).

[8] Rtd - introduction to resistance temperature detectors. URL http://www.omega.com/prodinfo/rtd.html.

[9] Intel® pentium® 4 processor 661 supporting ht technology. http://ark.intel.com/products/27485/Intel-Pentium-4-Processor-661-supporting-HT-Technology-2M-Cache-3_60-GHz-800-MHz-FSB. Accessed (2017-06-22).

[10] Thomas M. Adams. *Introductory MEMS*. Springer, 2010.

[11] Houssein Ammar, Bertrand Garnier, Ahmed Ould el Moctar, Hervé Willaime, Fabrice Monti, and Hassan Peerhossaini. Thermal analysis of chemical reactions in microchannels using highly sensitive thin-film heat-flux microsensor. *Chemical Engineering Science*, 94:150–155, 2013.

[12] A Andretta, B Bartoli, B Coluzzi, V Cuomo, and S De Stefano. Simple heat flux meter. *Review of Scientific Instruments*, 52(2):233–234, 1981.

[13] Zheng Cui. *Nanofabrication*. Springer International Publishing, 2017.

[14] JWC De Vries. Temperature-dependent resistivity measurements on polycrystalline sio2-covered thin nickel films. *Thin Solid Films*, 150(2-3):209–215, 1987.

[15] AH Epstein, GR Guenette, RJG Norton, and Cao Yuzhang. High-frequency response heat-flux gauge. *Review of Scientific Instruments*, 57(4):639–649, 1986.

[16] Buehler Ernest and Gordon K Teal. Process for producing semiconductive crystals of uniform resistivity, October 30 1956. US Patent 2,768,914.

[17] Martin Feldman. *Nanolithography: the art of fabricating nanoelectronic and nanophotonic devices and systems*. Woodhead publishing, 2014.

[18] Anushka S Gangnaik, Yordan M Georgiev, and Justin D Holmes. New generation electron beam resists: A review. 2017.

[19] SM Guo, CC Lai, TV Jones, MLG Oldfield, GD Lock, and AJ Rawlinson. The application of thin-film technology to measure turbine-vane heat transfer and effectiveness in a film-cooled, engine-simulated environment. *International Journal of Heat and Fluid Flow*, 19(6):594–600, 1998.

[20] David Hamadi, Bertrand Garnier, Herve Willaime, Fabrice Monti, and Hassan Peerhossaini. A novel thin-film temperature and heat-flux microsensor for heat transfer measurements in microchannels. *Lab on a Chip*, 12(3):652–658, 2012.

[21] I Hassan, P Phutthavong, and M1 Abdelgawad. Microchannel heat sinks: an overview of the state-of-the-art. *Microscale thermophysical engineering*, 8(3): 183–205, 2004.

[22] Frank P Incropera, Adrienne S Lavine, Theodore L Bergman, and David P DeWitt. *Principles of heat and mass transfer*. Wiley, 2013.

[23] Chandra Jha. *Thermal Sensors: Principles and Applications for Semiconductor Industries*. Springer, 2015.

[24] Satish Kandlikar, Srinivas Garimella, Dongqing Li, Stephane Colin, and Michael R King. *Heat transfer and fluid flow in minichannels and microchannels*. elsevier, 2005.

[25] Satish G Kandlikar and William J Grande. Evolution of microchannel flow passages–thermohydraulic performance and fabrication technology. *Heat transfer engineering*, 24(1):3–17, 2003.

[26] Jikwang Kim, Jongsung Kim, Younghwa Shin, and Youngsoo Yoon. A study on the fabrication of an rtd (resistance temperature detector) by using pt thin film. *Korean Journal of Chemical Engineering*, 18(1):61–66, 2001.

[27] Rakesh Kumar, Niranjan Sahoo, and Vinayak Kulkarni. Conduction based calibration of handmade platinum thin film heat transfer gauges for transient measurements. *International Journal of Heat and Mass Transfer*, 55(9):2707–2713, 2012.

[28] Chang Liu. *Foundations of MEMS*. Pearson Education Limited, 2012.

[29] Saeed Moghaddam. Microscale study of nucleation process in boiling of low-surface-tension liquids. *University of Maryland*, 2006.

[30] Saeed Moghaddam, Kenneth T Kiger, Alireza Modafe, and Reza Ghodssi. A novel benzocyclobutene-based device for studying the dynamics of heat transfer during the nucleation process. *Journal of Microelectromechanical systems*, 16(6):1355–1366, 2007.

[31] Omar Mokrani, Brahim Bourouga, Cathy Castelain, and Hassan Peerhossaini. Fluid flow and convective heat transfer in flat microchannels. *International Journal of Heat and Mass Transfer*, 52(5):1337–1352, 2009.

[32] Gordon E Moore. Cramming more components onto integrated circuits, reprinted from electronics, volume 38, number 8, april 19, 1965, pp. 114 ff. *IEEE Solid-State Circuits Society Newsletter*, 20(3):33–35, 2006.

[33] Jerry G Myers, Vamsee K Yerramilli, Sam W Hussey, Glenda F Yee, and Jungho Kim. Time and space resolved wall temperature and heat flux measurements during nucleate boiling with constant heat flux boundary conditions. *International Journal of Heat and Mass Transfer*, 48(12):2429–2442, 2005.

[34] J.V. Nicholas and D. R. White. *Traceable Temperatures: An Introduction To Temperature Measurement and Calibration.* John Wiley & Sons, 2001. doi: 9780471492917.

[35] James William Nilsson and Susan A Riedel. *Electric circuits.* Pearson, 2008.

[36] James William Nilsson and Susan A Riedel. *Electric circuits.* Pearson, 2008.

[37] David S. Nyce. *Linear Position Sensors.* Wiley Interscience, 2004.

[38] Pallàs and Webster. *Sensors and Signal Conditioning.* John Wiley & Sons, 2001.

[39] E Piccini, SM Guo, and TV Jones. The development of a new direct-heat-flux gauge for heat-transfer facilities. *Measurement Science and Technology*, 11(4): 342, 2000.

[40] Weilin Qu and Issam Mudawar. Flow boiling heat transfer in two-phase microchannel heat sinks—i. experimental investigation and assessment of correlation methods. *International Journal of Heat and Mass Transfer*, 46(15): 2755–2771, 2003.

[41] Michael Quirk and Julian Serda. *Semiconductor manufacturing technology*, volume 1. Prentice Hall Upper Saddle River, NJ, 2001.

[42] Karen Reinhardt and Werner Kern. *Handbook of silicon wafer cleaning technology.* William Andrew, 2008.

[43] WM Richard. A sensor classification scheme. *IEEE Trans. Ultrason. Ferroelectr. Freq. Control*, 34(2):124–126, 1987.

[44] TD Rule and J Kim. Heat transfer behavior on small horizontal heaters during pool boiling of fc-72. *Journal of Heat Transfer*, 121(2):386–393, 1999.

[45] Robert R Schaller. Moore's law: past, present and future. *IEEE spectrum*, 34 (6):52–59, 1997.

[46] M Schirmer, B Büttner, F Syrowatka, G Schmidt, T Köpnick, and C Kaiser. Chemical semi-amplified positive e-beam resist (csar 62) for highest resolution. In *29th European Mask and Lithography Conference*, pages 88860D–88860D. International Society for Optics and Photonics, 2013.

[47] Frederick Seitz and Norman G Einspruch. *Electronic genie: The tangled history of silicon.* University of Illinois Press, 1998.

[48] Choondal B Sobhan and George P Peterson. *Microscale and nanoscale heat transfer: fundamentals and engineering applications*. CRC Press, 2008.

[49] Sylwia Szczukiewicz, Navid Borhani, and John Richard Thome. Fine-resolution two-phase flow heat transfer coefficient measurements of refrigerants in multi-microchannel evaporators. *International Journal of Heat and Mass Transfer*, 67:913–929, 2013.

[50] Simon M. Sze. *Semiconductor sensors*, volume 55. Wiley New York, 1994.

[51] DM Tennant and AR Bleier. Electron beam lithography of nanostructures. *Handbook of Nanofabrication (Elsevier, Amsterdam 2010) Chap*, 4:121–148, 2010.

[52] Stephen Thoms and Douglas S Macintyre. Investigation of csar 62, a new resist for electron beam lithography. *Journal of Vacuum Science & Technology B*, 32(6):06FJ01, 2014.

[53] Ampere A Tseng. *Nanofabrication: fundamentals and applications*. World Scientific, 2008.

[54] David B Tuckerman and RFW Pease. High-performance heat sinking for vlsi. *IEEE Electron device letters*, 2(5):126–129, 1981.

[55] M Mitchell Waldrop. The chips are down for moore's law. *Nature*, 530(7589): 144–147, 2016.

[56] Guodong Wang, Ping Cheng, and AE Bergles. Effects of inlet/outlet configurations on flow boiling instability in parallel microchannels. *International Journal of Heat and Mass Transfer*, 51(9):2267–2281, 2008.

[57] Charles Wheatstone. The bakerian lecture: An account of several new instruments and processes for determining the constants of a voltaic circuit. *Philosophical Transactions of the Royal Society of London*, 133:303–327, 1843.

[58] JL Xu, YH Gan, DC Zhang, and XH Li. Microscale heat transfer enhancement using thermal boundary layer redeveloping concept. *International Journal of Heat and Mass Transfer*, 48(9):1662–1674, 2005.

[59] Aymen Zribi, Magali Barthès, Sylvie Bégot, François Lanzetta, Jean Yves Rauch, and Virginie Moutarlier. Design, fabrication and characterization of thin film resistances for heat flux sensing application. *Sensors and Actuators A: Physical*, 245:26–39, 2016.

Part IV

APPENDIX

Appendix A

Preliminary Designs and Results

This appendix contains images from preliminiary fabrication cycles when the scope of the design was broader than what has been presented in the main part of this thesis. These earlier iterations revealed that the main fabrication challenge was for the designs where the pitch between neighbouring tracks was the lowest, and thus, these design became the focus of the thesis.

Originally, 36 RTD's were designed and arranged in an array, where each row contained sensors of equal size and track width, w, and the pitch between neighbouring tracks were varied between each column, ultimately differentiating the track length, l. As may be seen in the following images, the high pitch RTD's were easily obtained since the large distance between the track mitigated the risk of back-scattering and exposure of neighbouring lines, but the low pitch RTD's suffered ramarkably from the scattering effects, resulting in RTD's where the tracks have bled into each other, causing an open circuit and deeming the RTD's uncapable of detecting changes in resistance.

In the following pages a selection the preliminary results are presented in a gallery format for comparison with the final results of the main thesis. The results originate from two different batches, apropriately labeled by the month of fabrication in the captions below each image. The lead wires and bond pads are identical to the ones introduced in the main part of this thesis. As mentioned above, the sensors scope was broader in these earlier iterations, with additional variations of windings and trak length within each size. However, the design approach is identical to the final design, and the six variations within each size is briefly introduced

in the first pages of this appendix.

A.1 Preliminary Design, Layout and Results

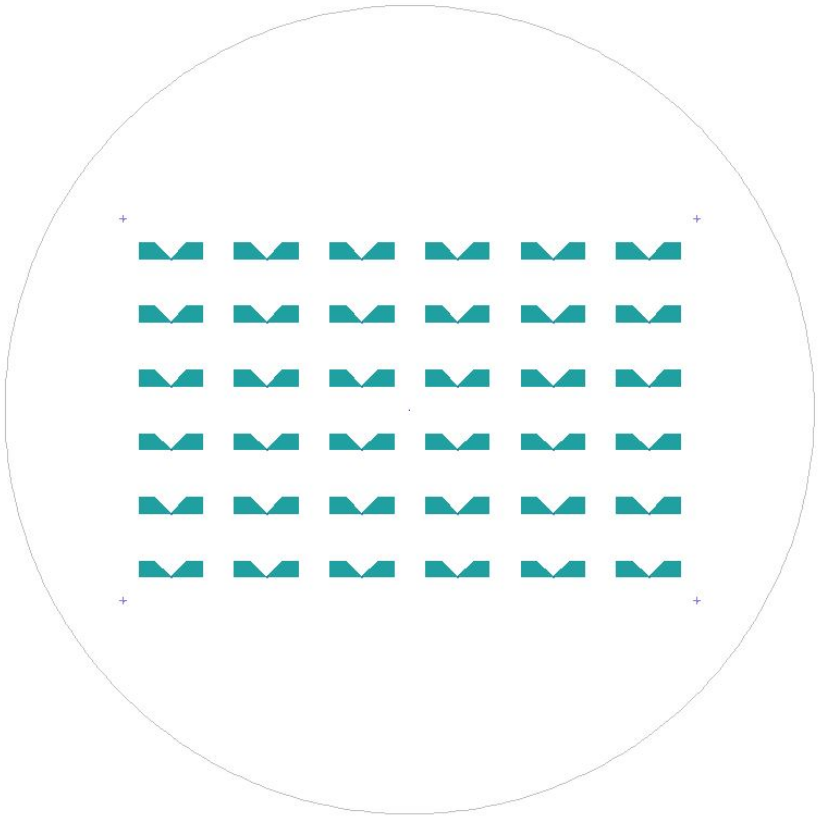

Figure A.1: Preliminary design. 36 sensors labeled in the same manner as the design presented in the main part of this thesis, i.e. S1 – S36.

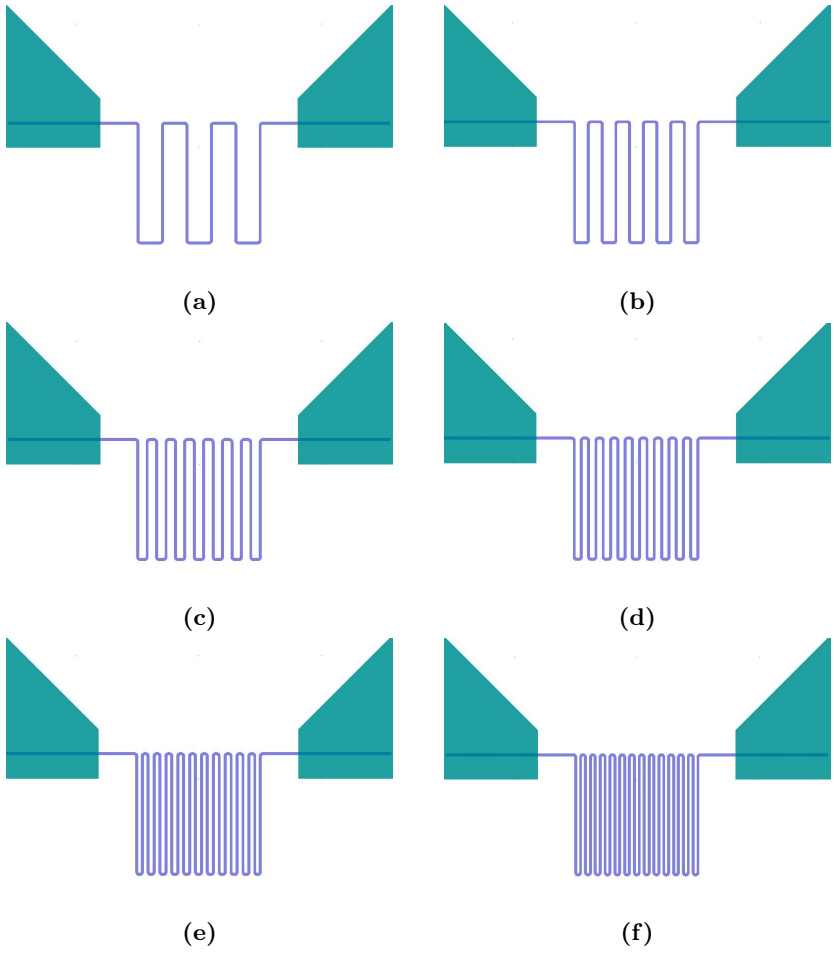

Figure A.2: Preliminary design showing the additional track length variations within each size by decreasing the pitch between neighboring tracks.

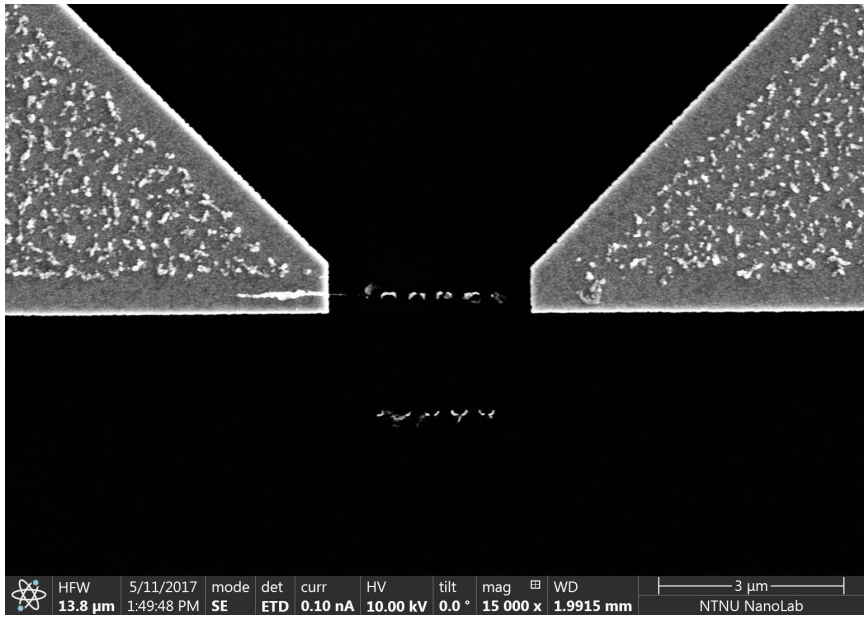

Figure A.3: S8 – $2\mu m \times 2\mu$m – April 2017.

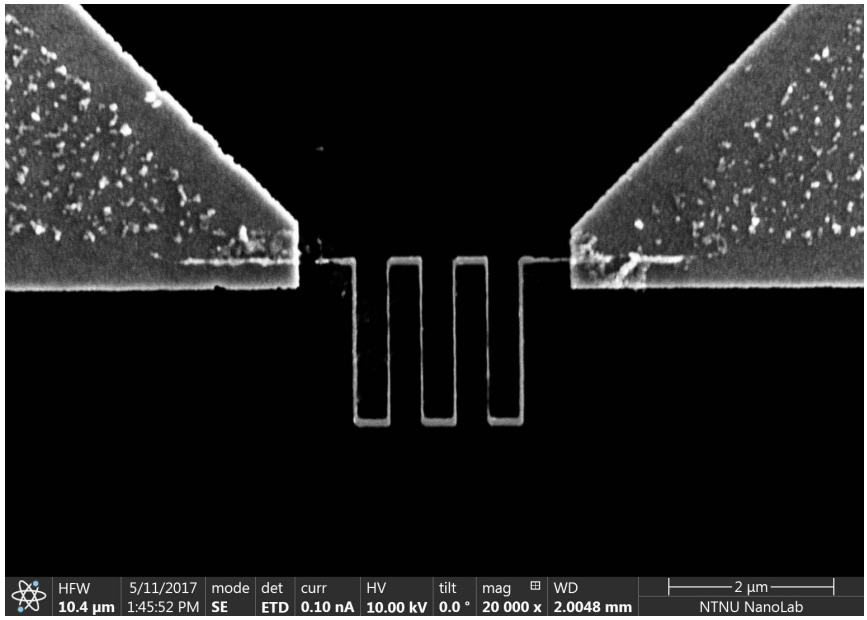

Figure A.4: S7 – $2\mu m \times 2\mu$m – April 2017.

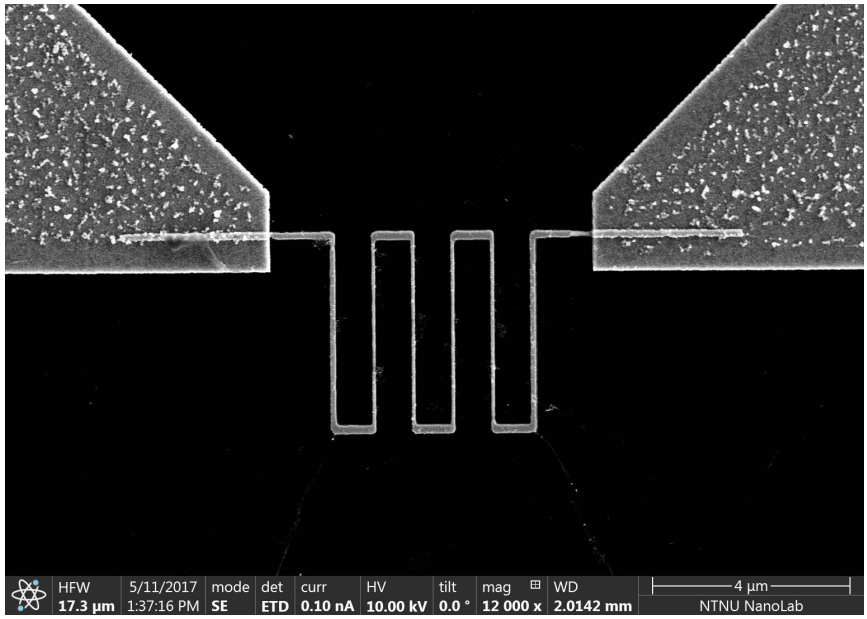

Figure A.5: S19 – $4\mu m \times 4\mu$m – April 2017.

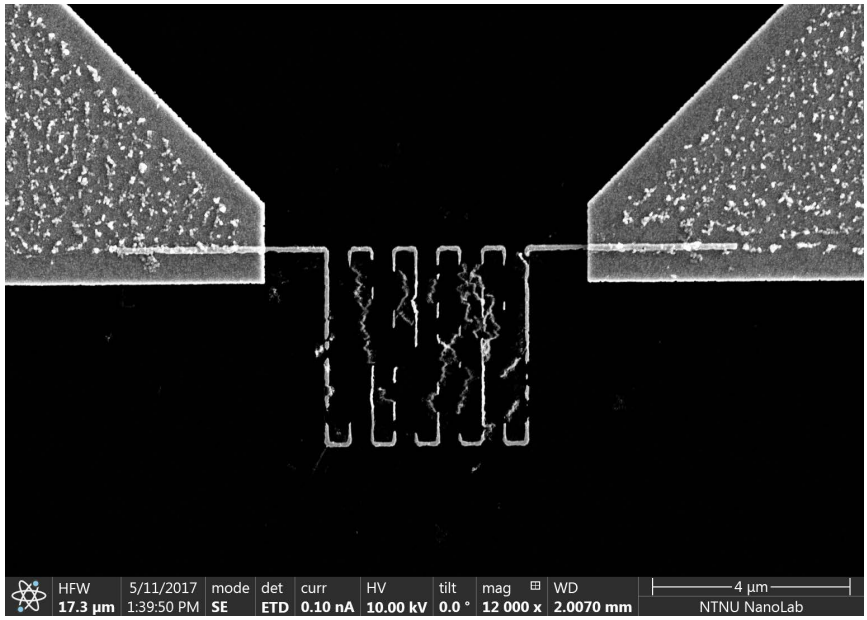

Figure A.6: S20 – $4\mu m \times 4\mu$m – April 2017.

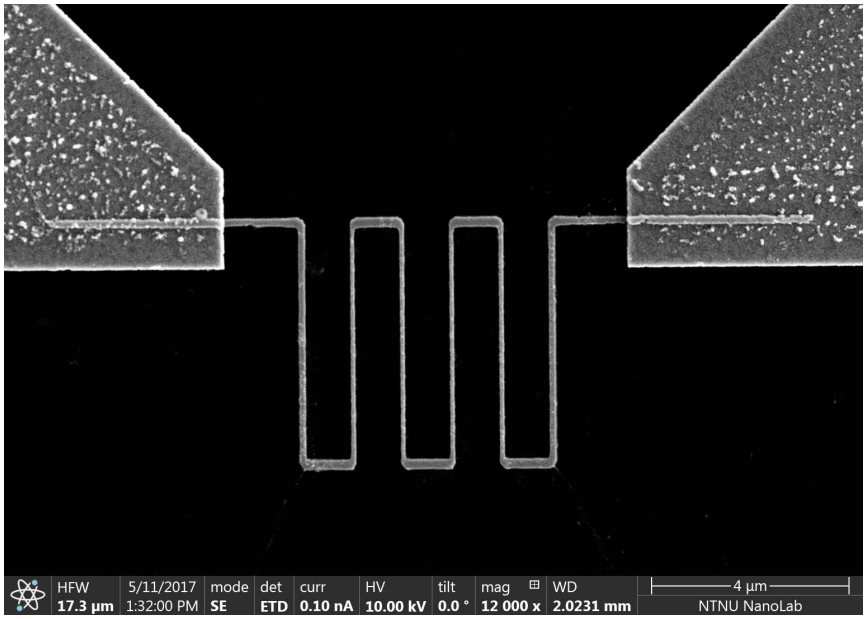

Figure A.7: S25 – $5\mu m \times 5\mu$m – April 2017.

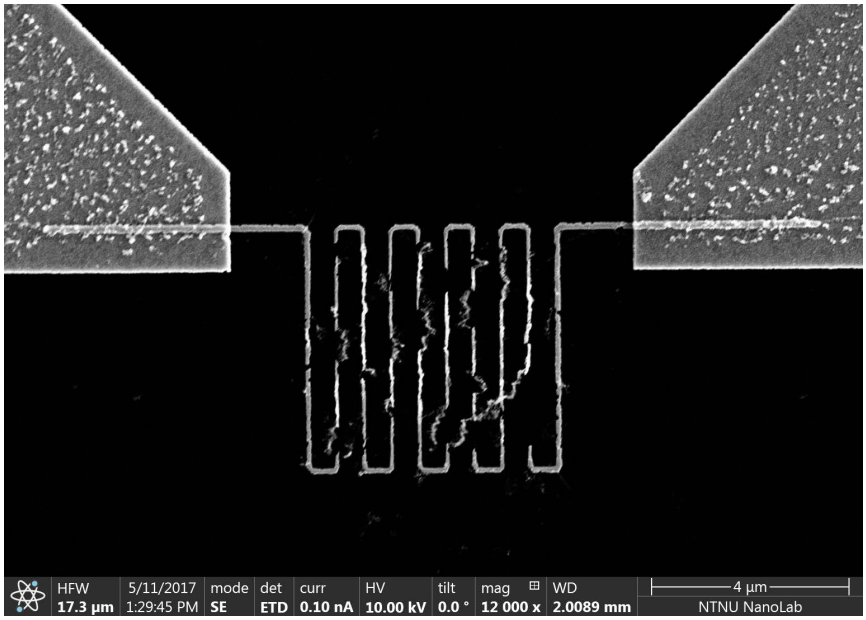

Figure A.8: S26 – $5\mu m \times 5\mu$m – April 2017.

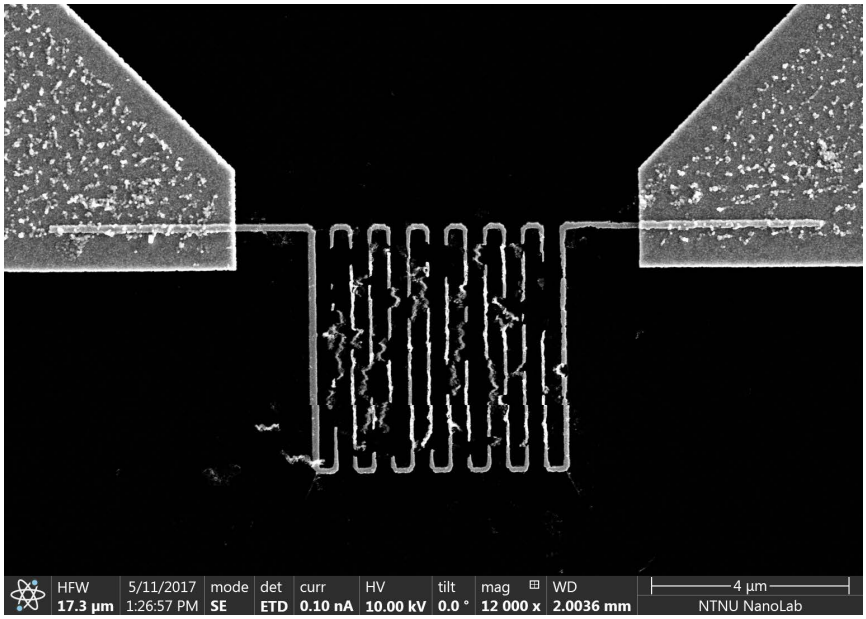

Figure A.9: S27 – $5\mu m \times 5\mu$m – April 2017.

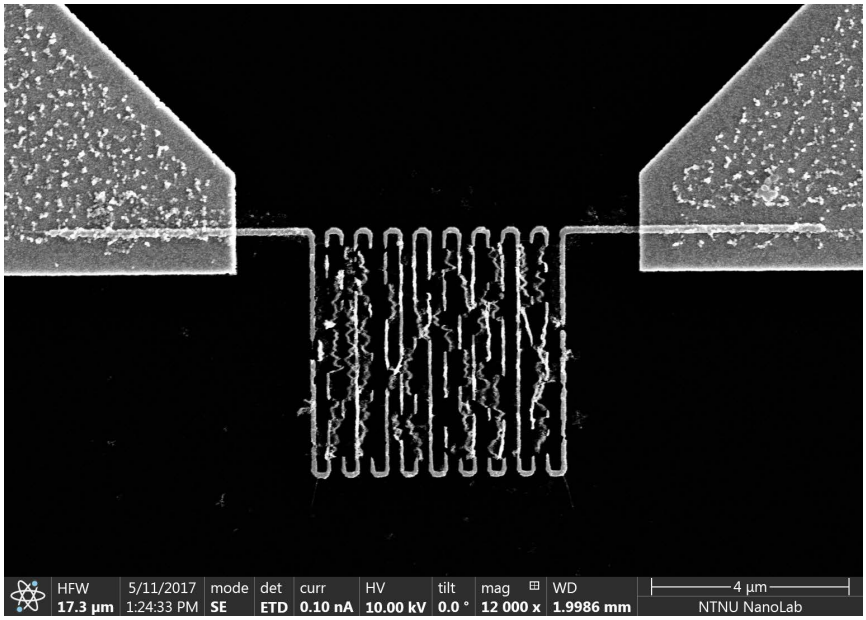

Figure A.10: S28 – $5\mu m \times 5\mu$m – April 2017.

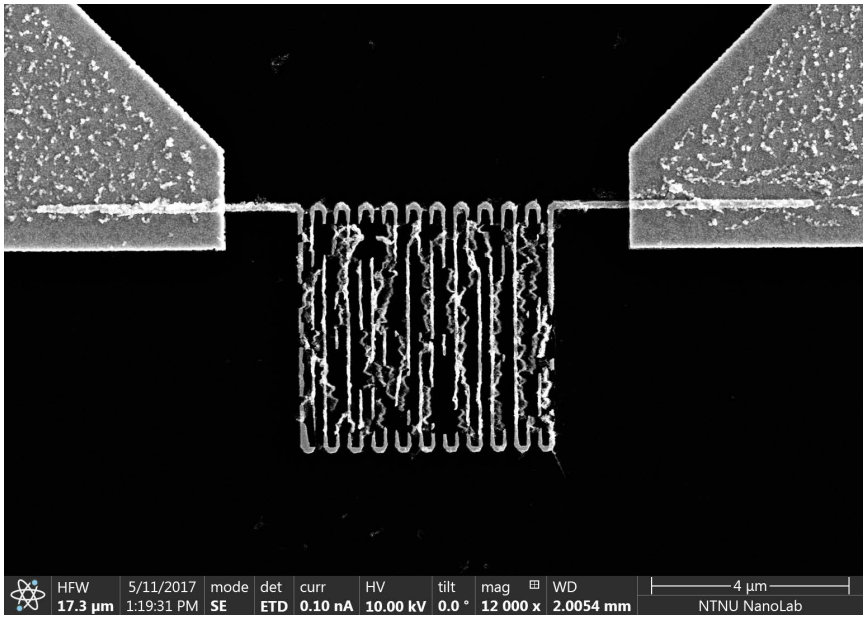

Figure A.11: S29 – $5\mu m \times 5\mu$m – April 2017.

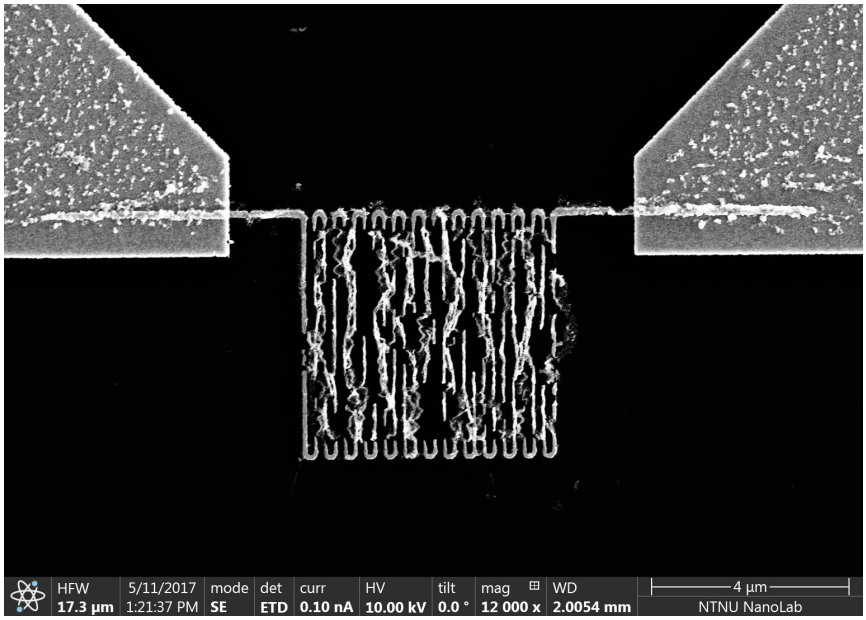

Figure A.12: S30 – $5\mu m \times 5\mu$m – April 2017.

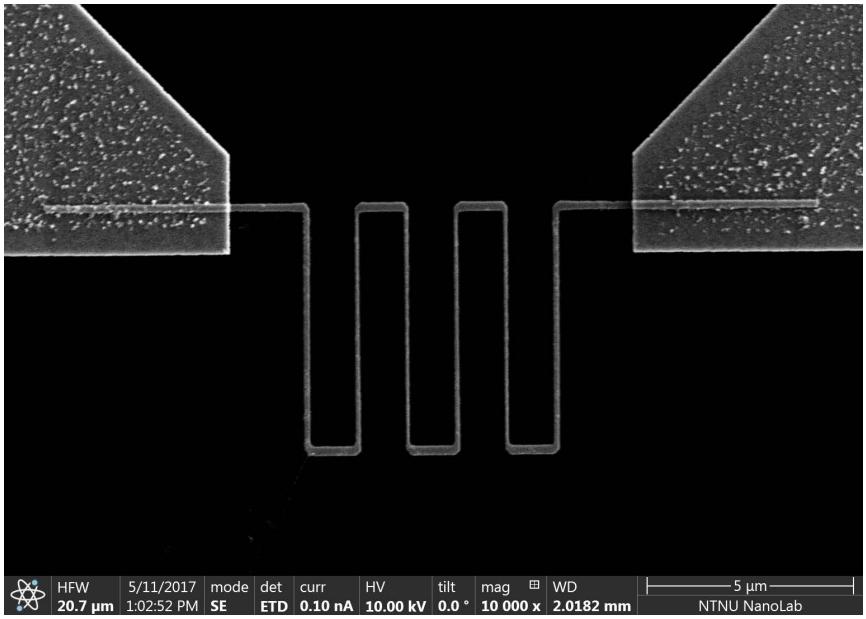

Figure A.13: S31 – $6\mu m \times 6\mu$m – April 2017.

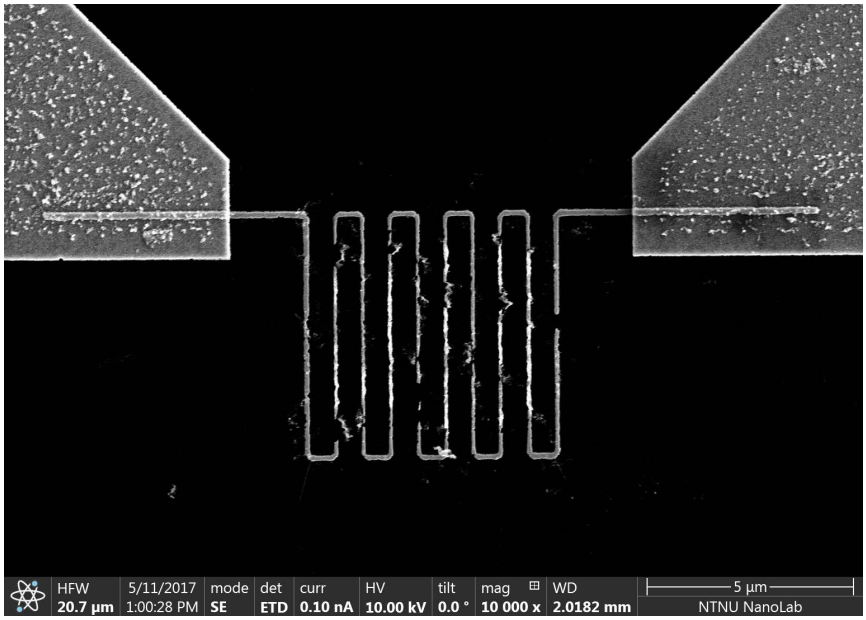

Figure A.14: S32 – $6\mu m \times 6\mu$m – April 2017.

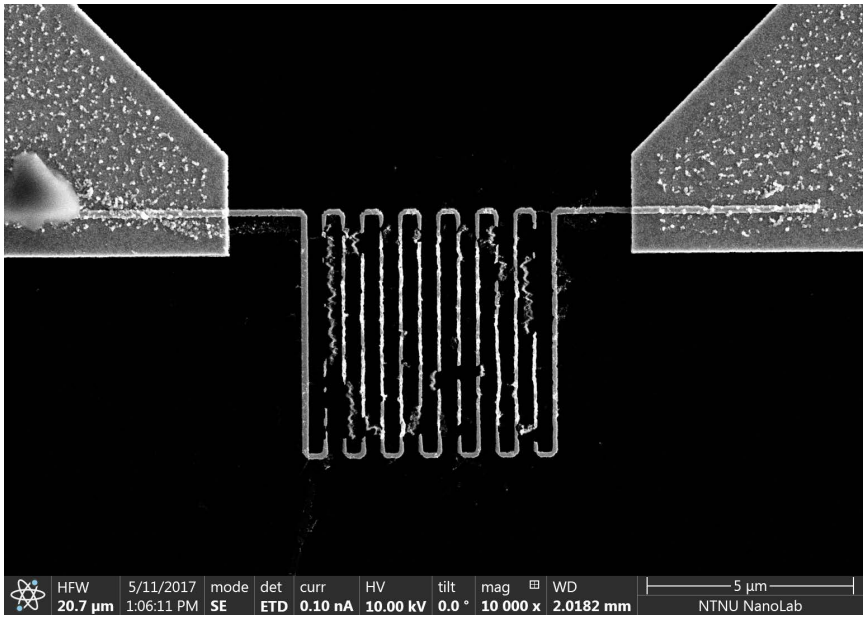

Figure A.15: S33 – $6\mu m \times 6\mu$m – April 2017.

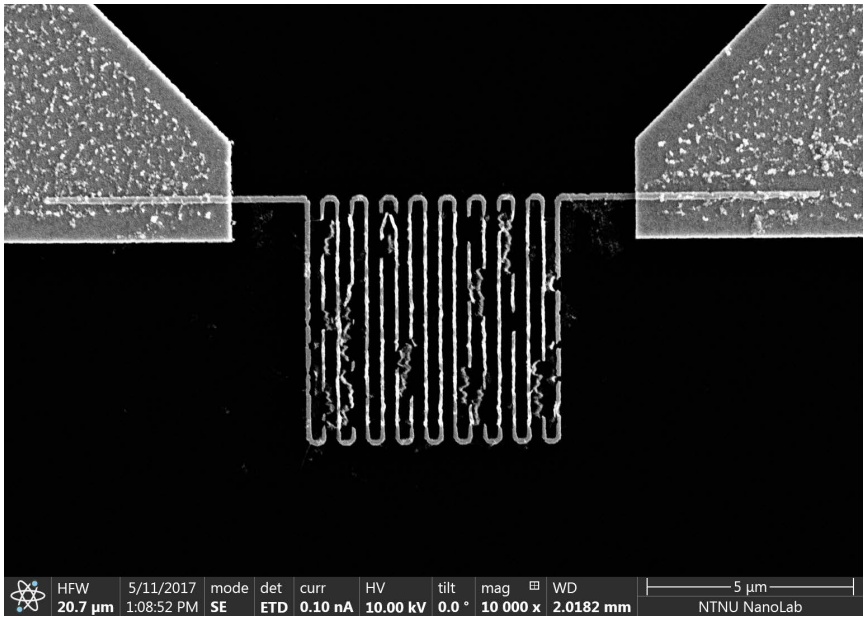

Figure A.16: S34 – $6\mu m \times 6\mu$m – April 2017.

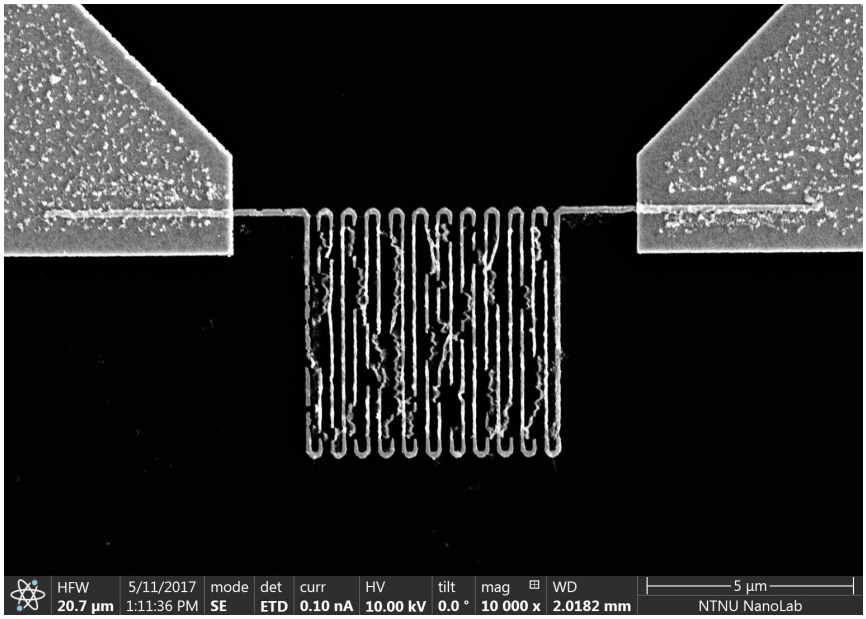

Figure A.17: S35 – $6\mu m \times 6\mu$m – April 2017.

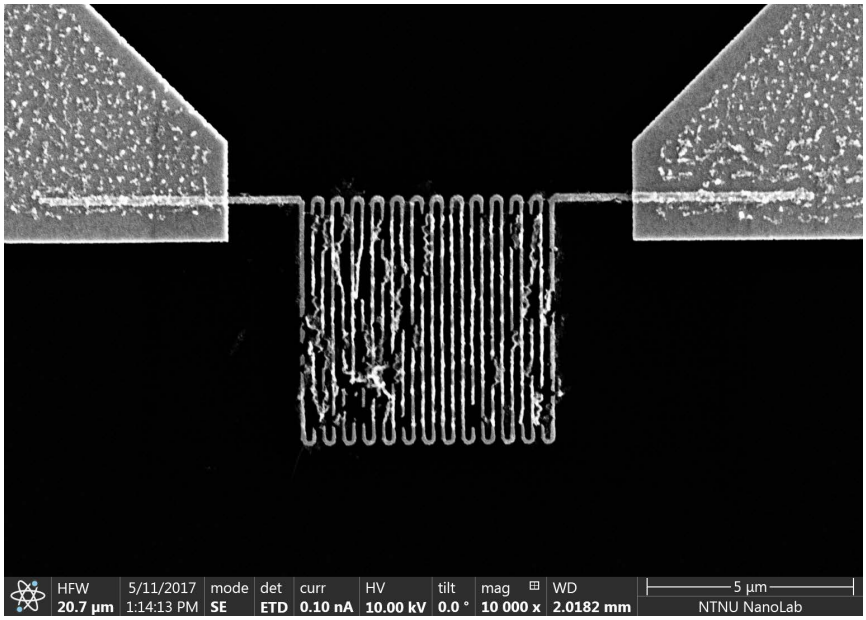

Figure A.18: S36 – $6\mu m \times 6\mu$m – April 2017.

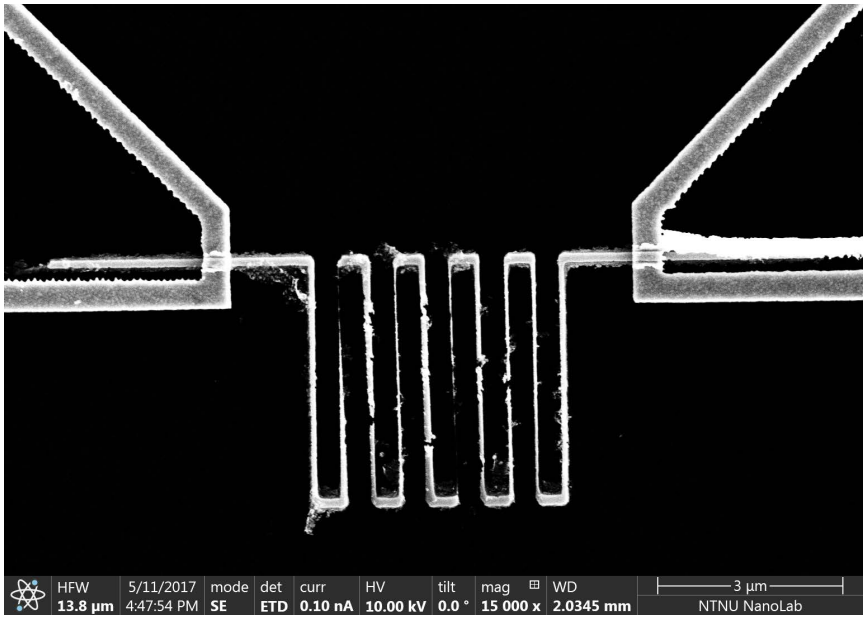

Figure A.19: S20 – $4\mu m \times 4\mu$m – May 2017.

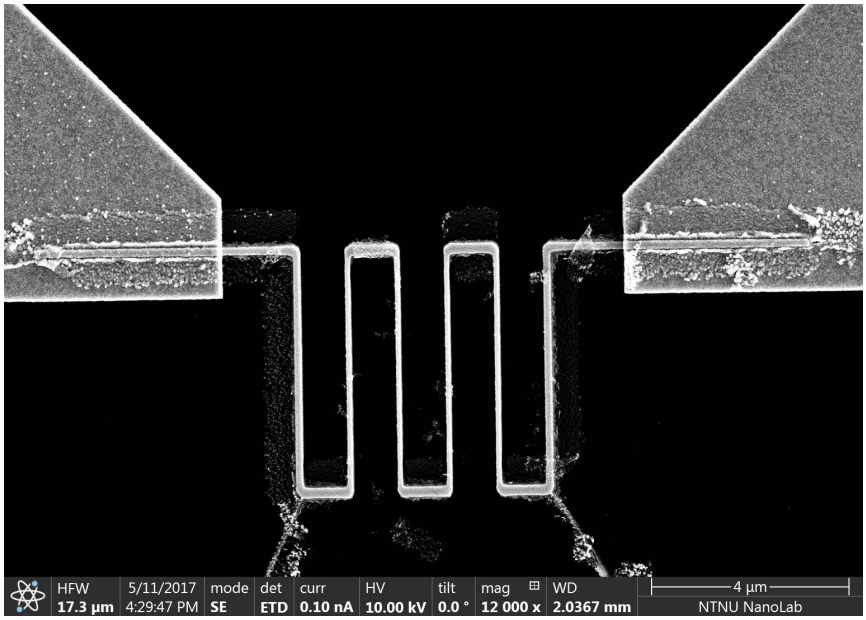

Figure A.20: S25 – $5\mu m \times 5\mu$m – May 2017.

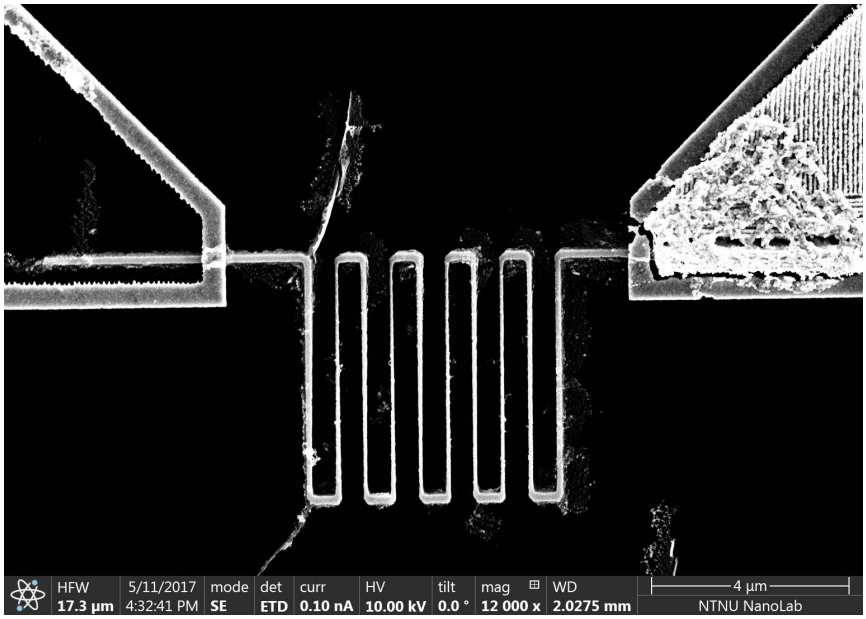

Figure A.21: S26 – $5\mu m \times 5\mu$m – May 2017.

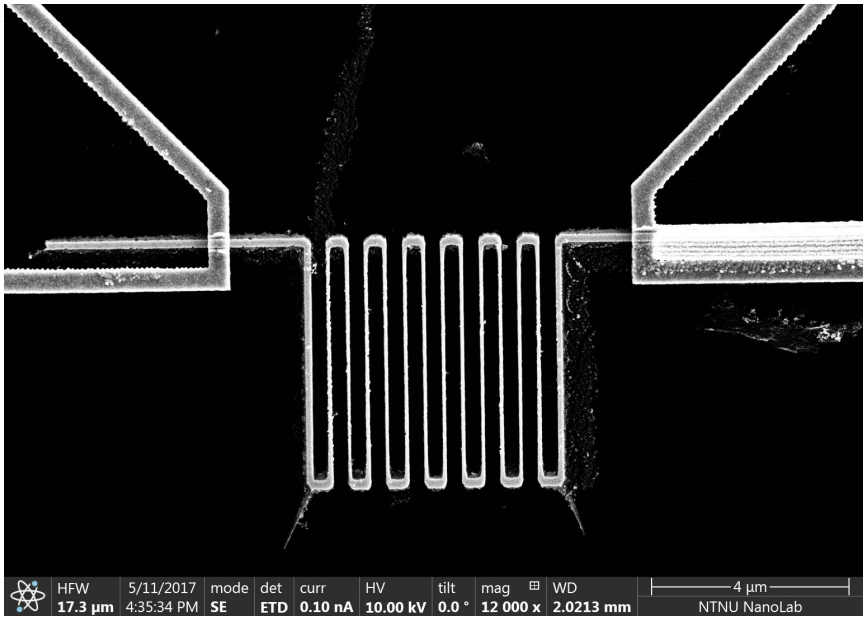

Figure A.22: S27 – $5\mu m \times 5\mu$m – May 2017.

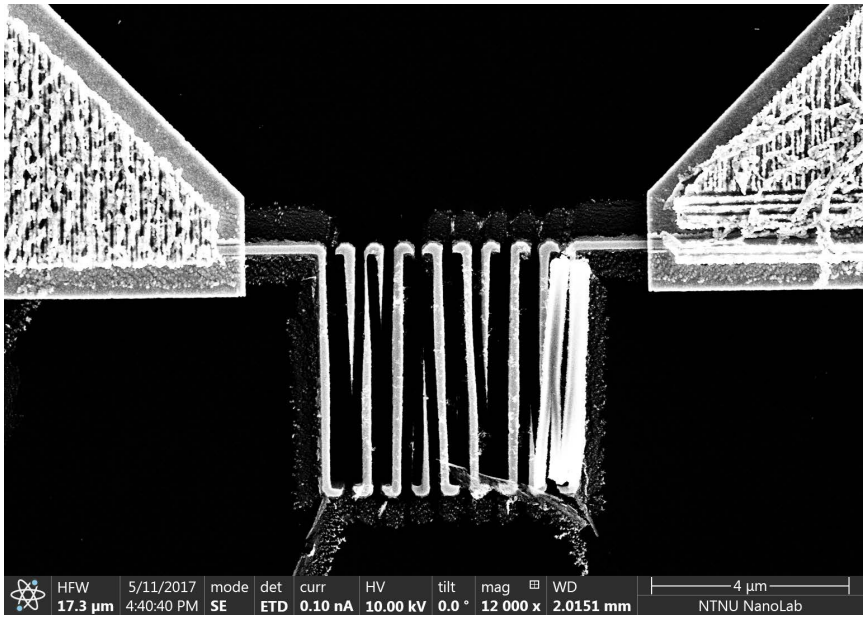

Figure A.23: S28 – $5\mu m \times 5\mu$m – May 2017.

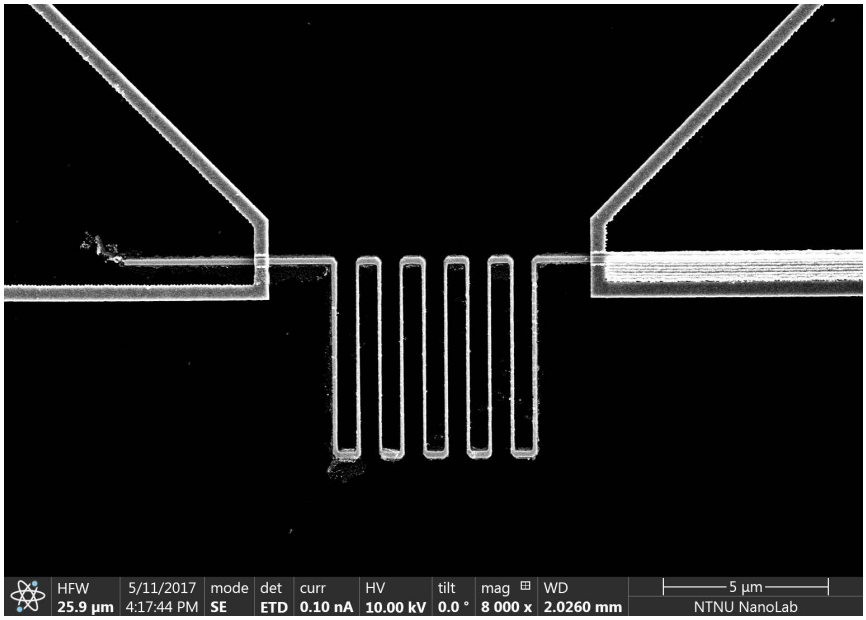

Figure A.24: S32 – $6\mu m \times 6\mu$m – May 2017.

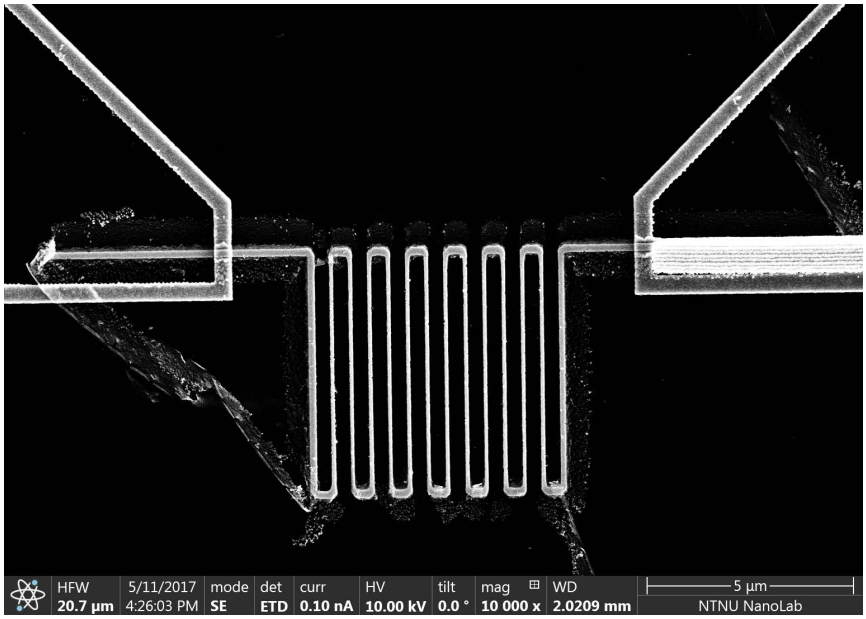

Figure A.25: S33 – 6μm × 6μm – May 2017.

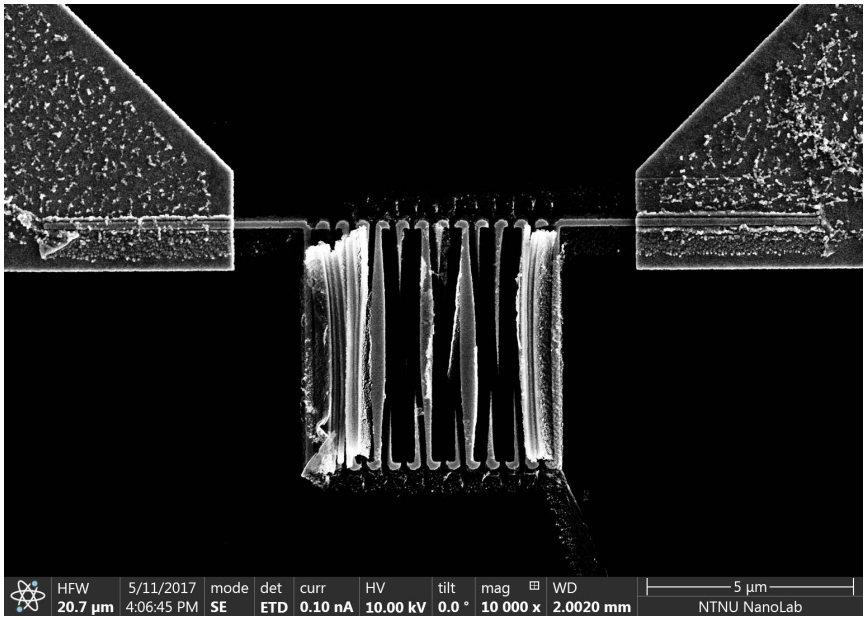

Figure A.26: S36 – 6μm × 6μm – May 2017.

Appendix B

TRACER Simulations

B.1 Electron Trajectories at 100kV and 25kV

In this appendix TRACER simulations displaying the electron trajectories in PMMA on 250μm Si are presented. The resist thicknesses are 100 nm and 410nm according to the layers used in this work. The aim for these simulations was to determine how the resist thickness, acceleration voltage and beam diameter affected the forward- and backscattering. However, the effects were not quantified, and the results are only indicative by visual inspection. The most profound results are found by comparison of the 25kV and 100kV acelleration voltage. In the 25kV simulation, the backscattering is significantly reduced compared to the 100kV. However, the forward-scattering is proportionally increased. Thus, for the usage of 25kV systems, beam currents significantly lower than 100pA is expected to be needed, in order to compensate for the increase in forward-scattering.

Even for 100kV systems, where the forward-scattering is negligible compared to backscattering, the impacts may be significant for various resist thicknesses if very small, and dense, patterns are intended. The resist thickness is limited by the metalization process, and using even thinner layers than 100 nm increases the risk of an unsuccessful Lift-Off procedure.

B.1.1 100nm PMMA using 100pA Beam Current and 100kV

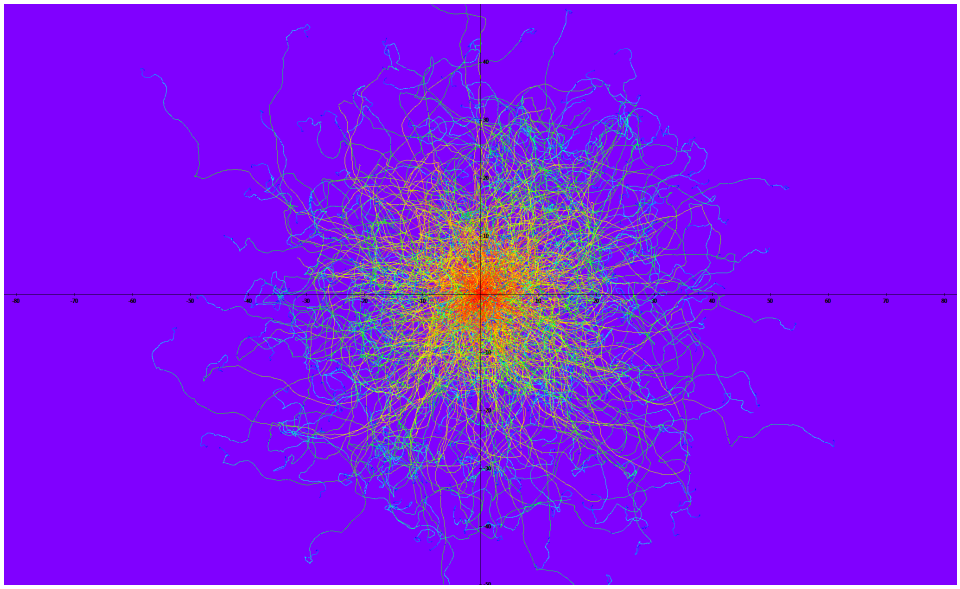

Figure B.1: Top view of the electron trajectories.

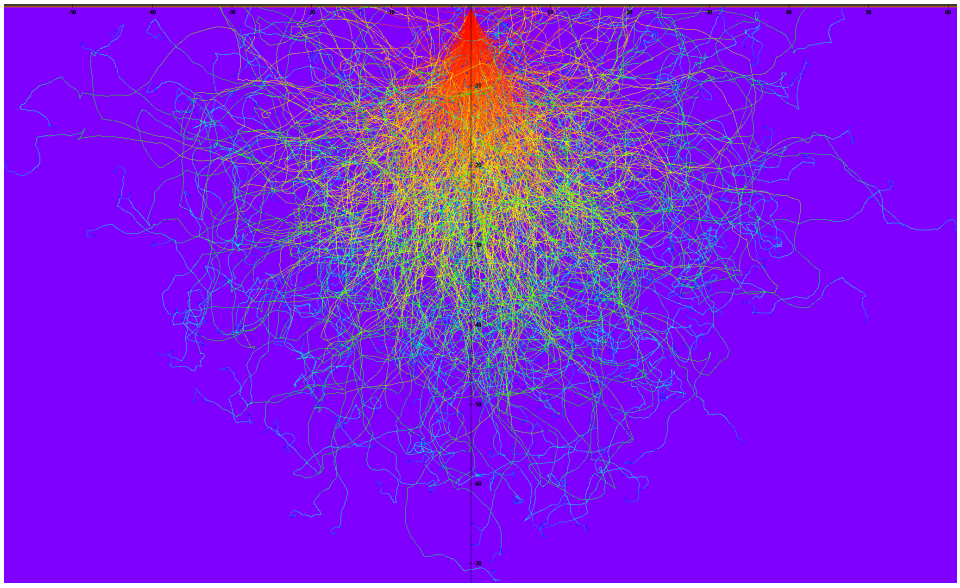

Figure B.2: Side view of the electron trajectories.

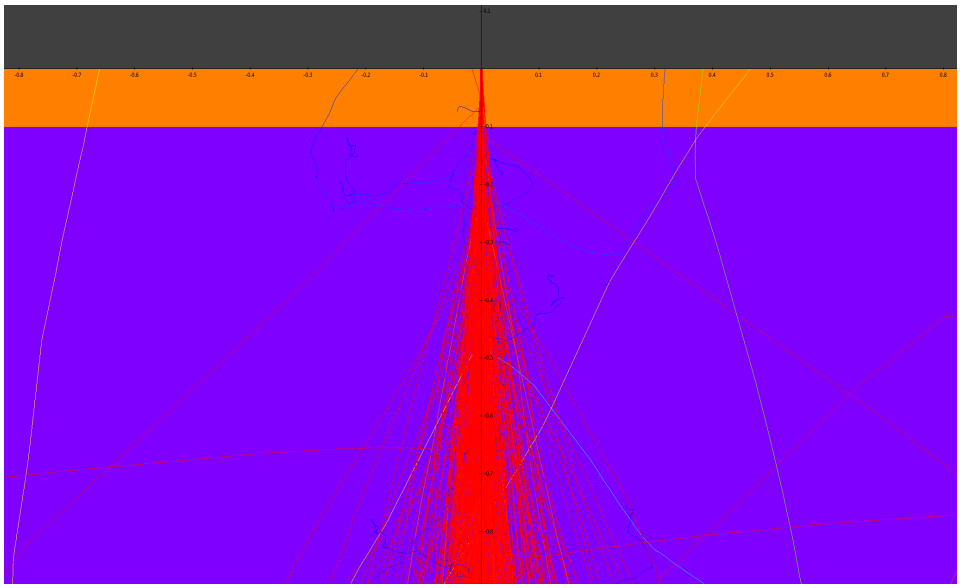

Figure B.3: Detailed view of the electron trajectories in the substrate boundary.

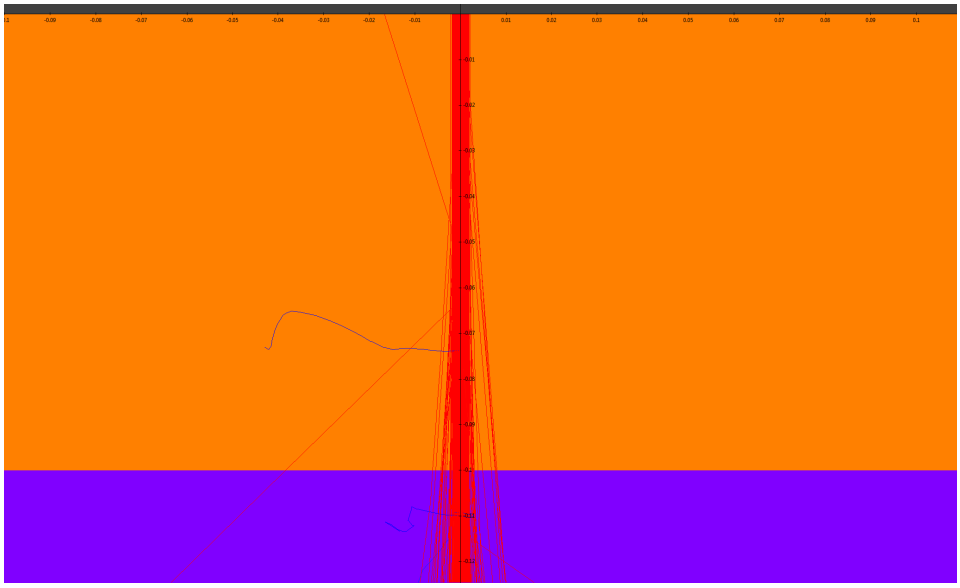

Figure B.4: Detailed view of the forward scattering effects in the resist layer.

B.1.2 410nm PMMA using 100pA Beam Current and 100kV

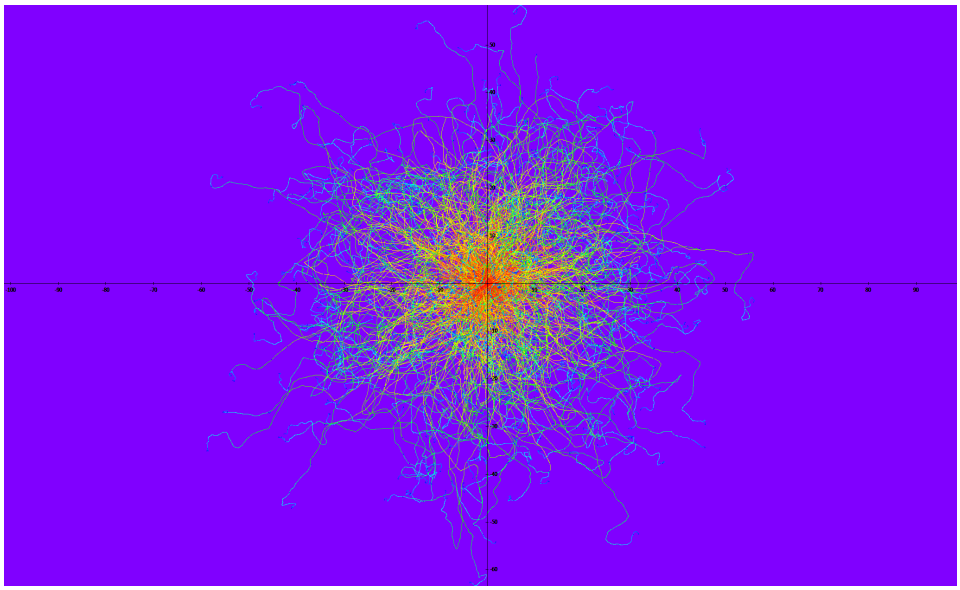

Figure B.5: Top view of the electron trajectories.

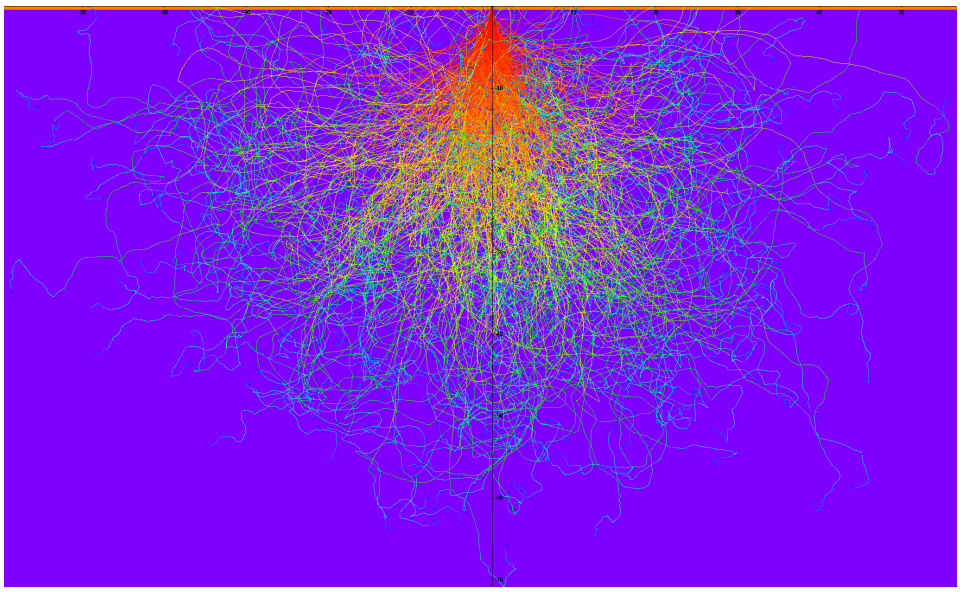

Figure B.6: Side view of the electron trajectories.

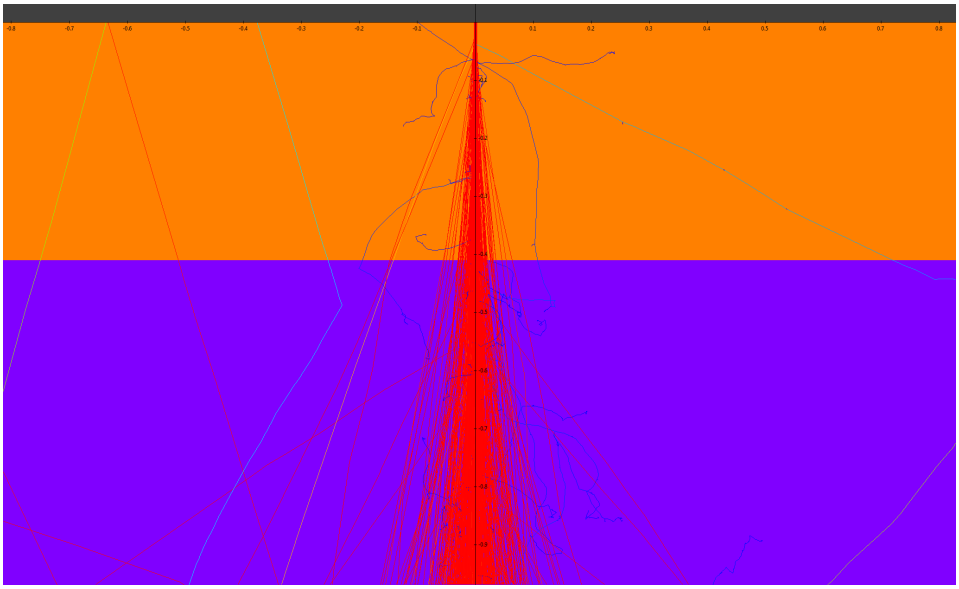

Figure B.7: Detailed view of the electron trajectories in the substrate boundary.

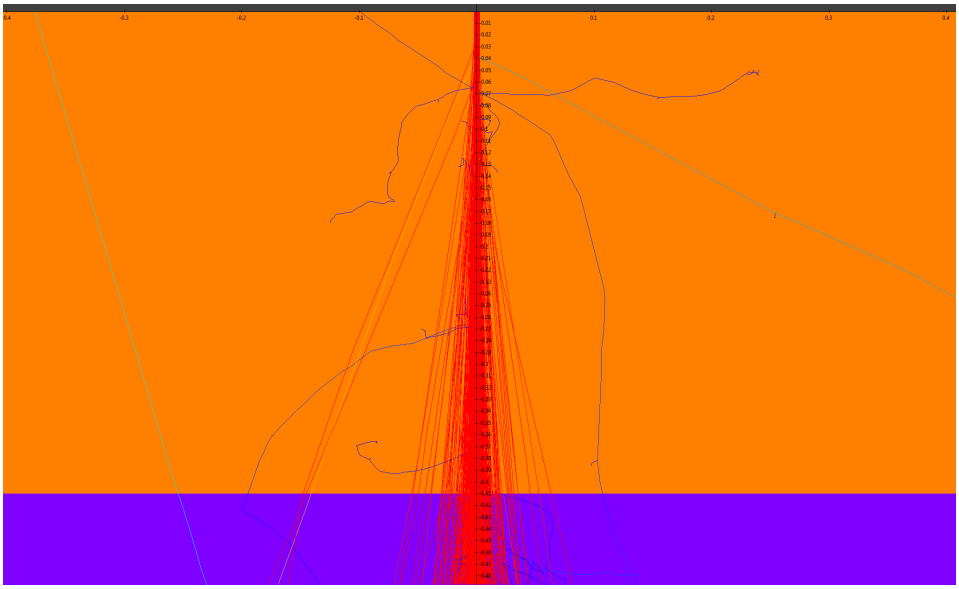

Figure B.8: Detailed view of the forward scattering effects in the resist layer.

B.1.3 100nm PMMA using 5nA Beam Current and 100kV

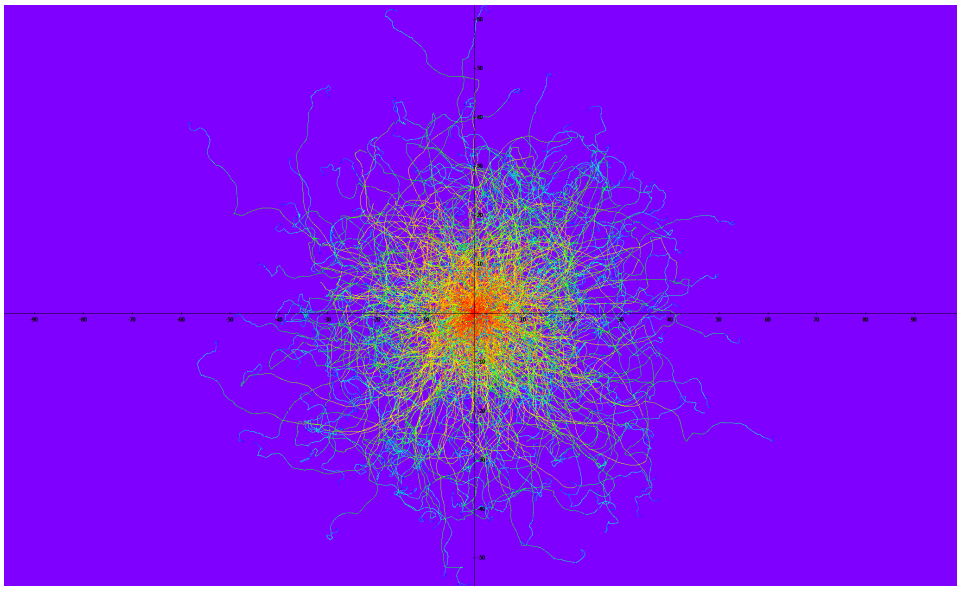

Figure B.9: Top view of the electron trajectories.

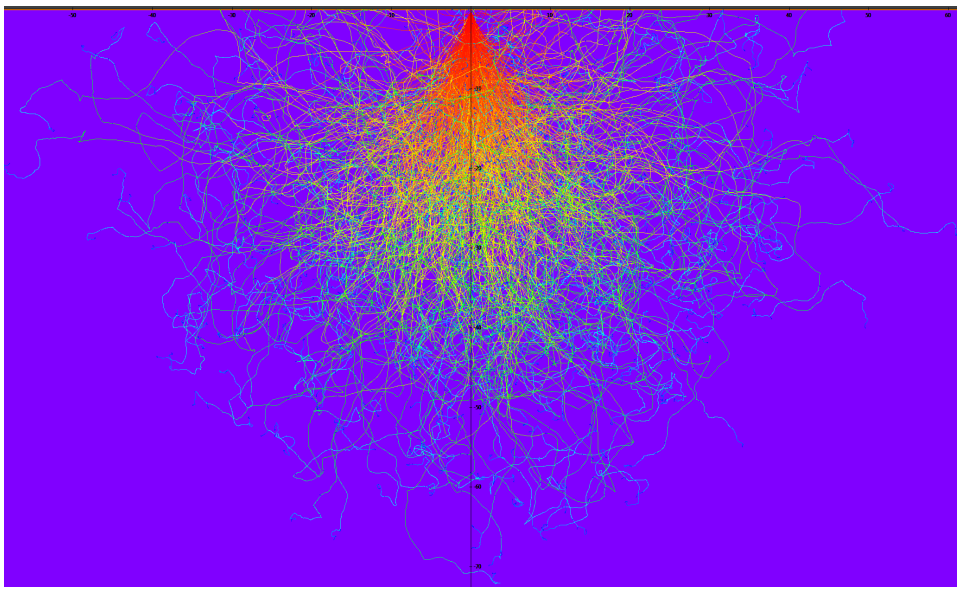

Figure B.10: Side view of the electron trajectories.

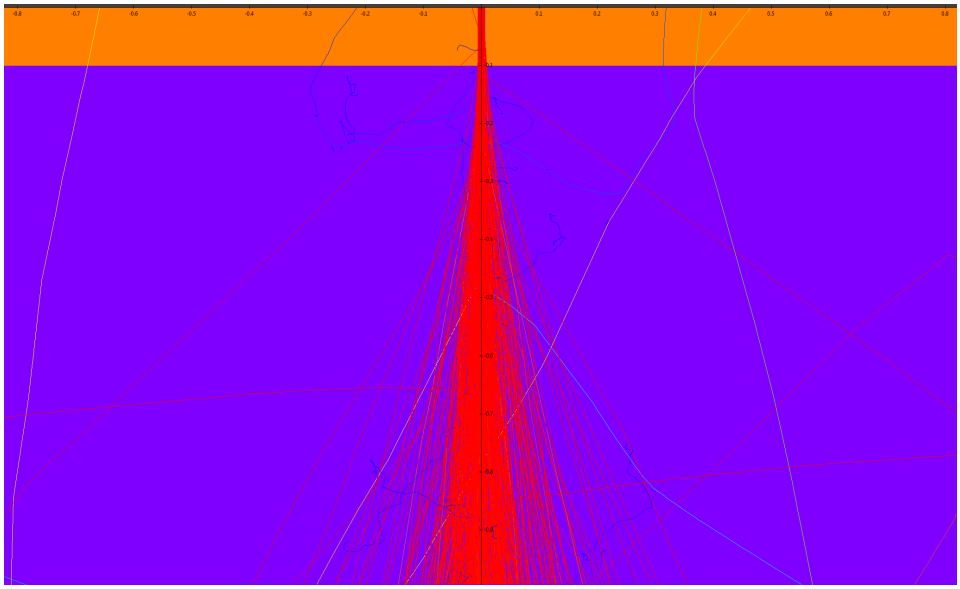

Figure B.11: Detailed view of the electron trajectories in the substrate boundary.

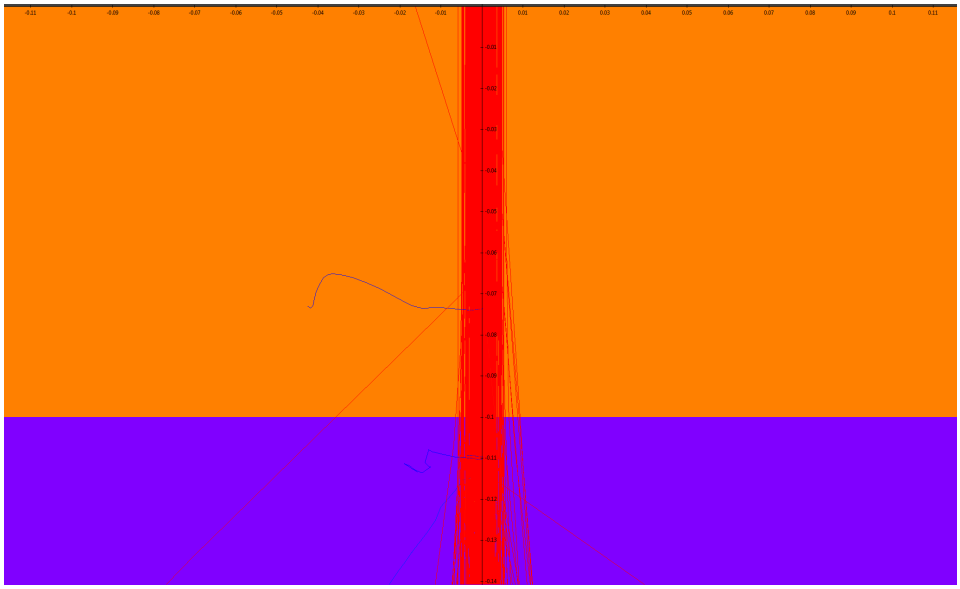

Figure B.12: Detailed view of the forward scattering effects in the resist layer.

B.1.4 410nm PMMA using 5nA Beam Current and 100kV

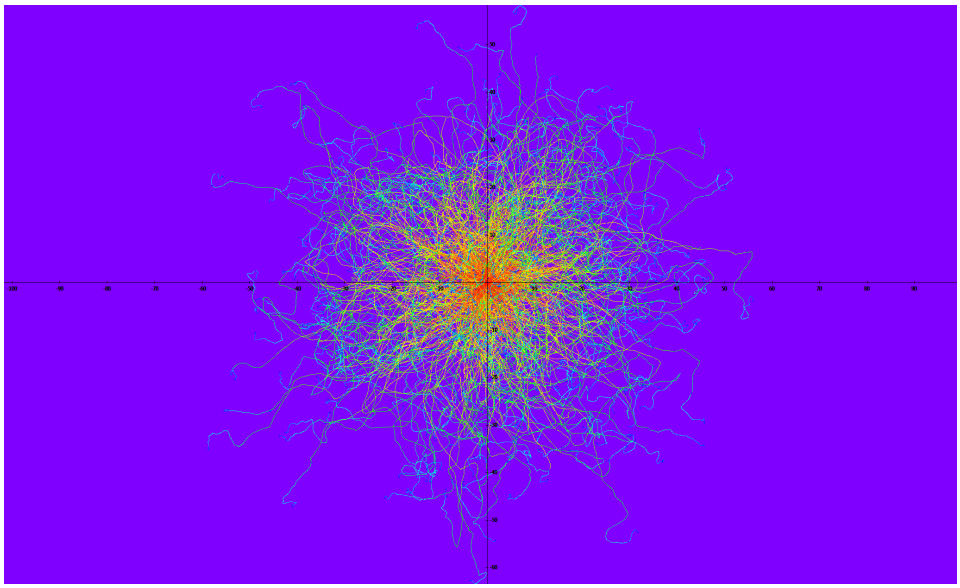

Figure B.13: Top view of the electron trajectories.

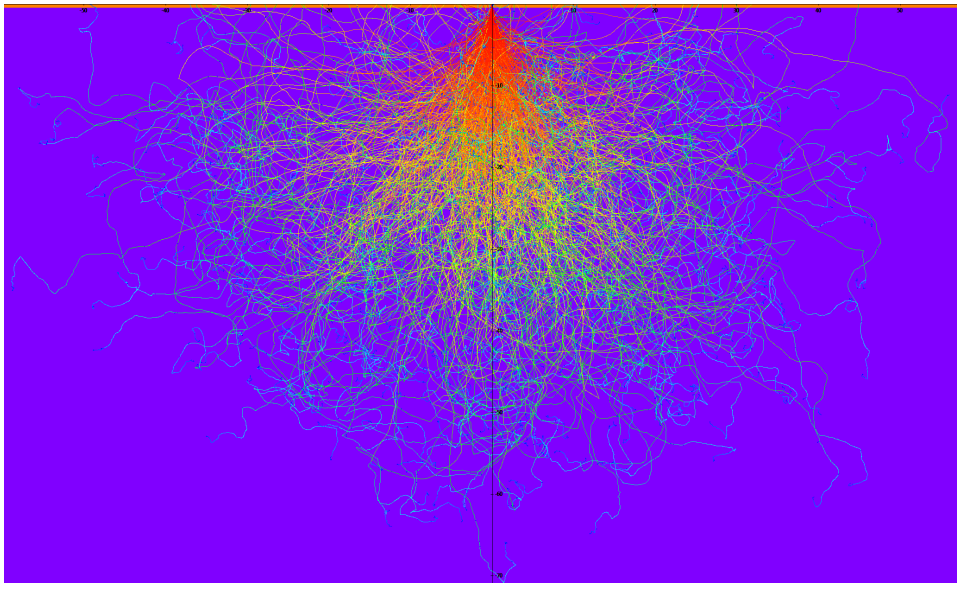

Figure B.14: Side view of the electron trajectories.

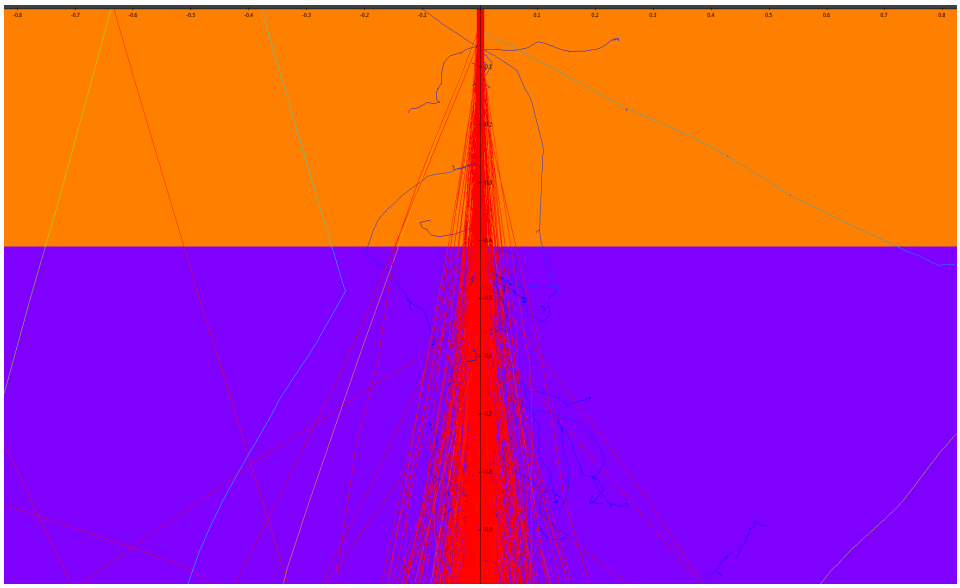

Figure B.15: Detailed view of the electron trajectories in the substrate boundary.

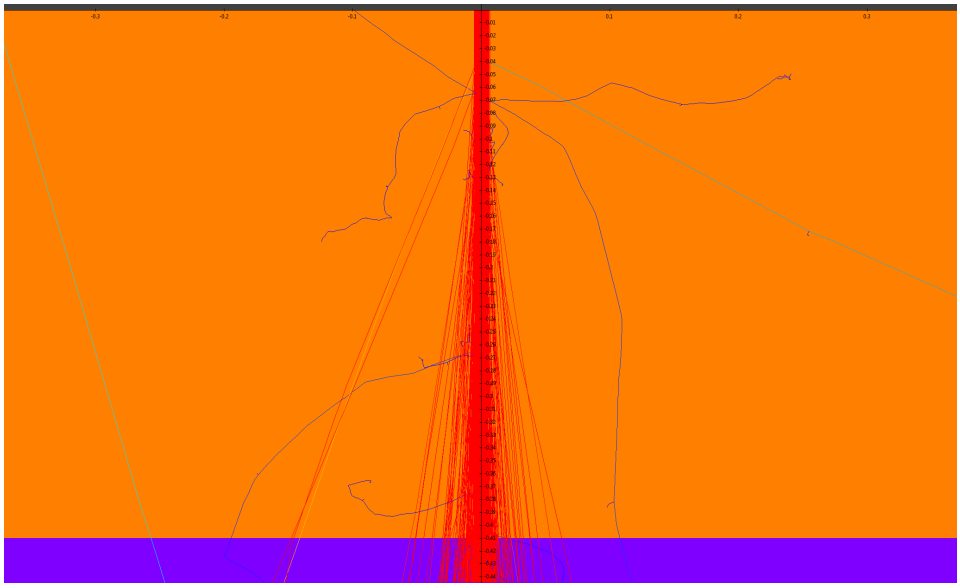

Figure B.16: Detailed view of the forward scattering effects in the resist layer.

B.1.5 410nm PMMA using 50nA Beam Current and 100kV

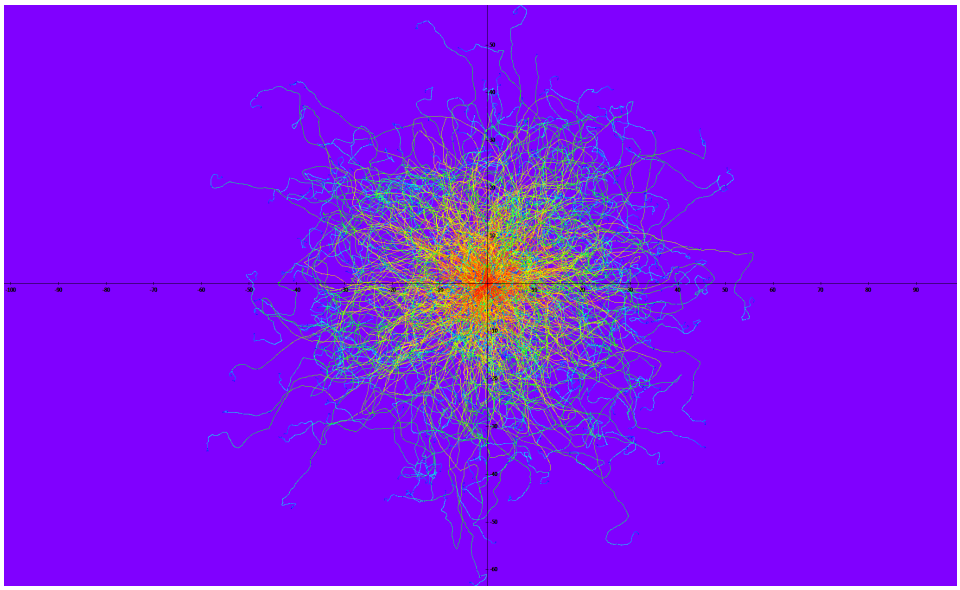

Figure B.17: Top view of the electron trajectories.

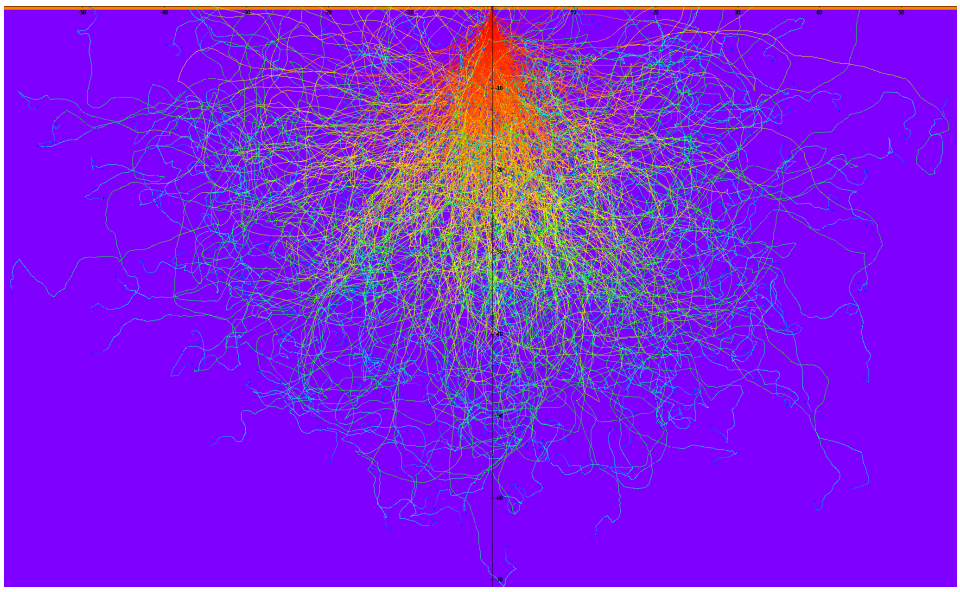

Figure B.18: Side view of the electron trajectories.

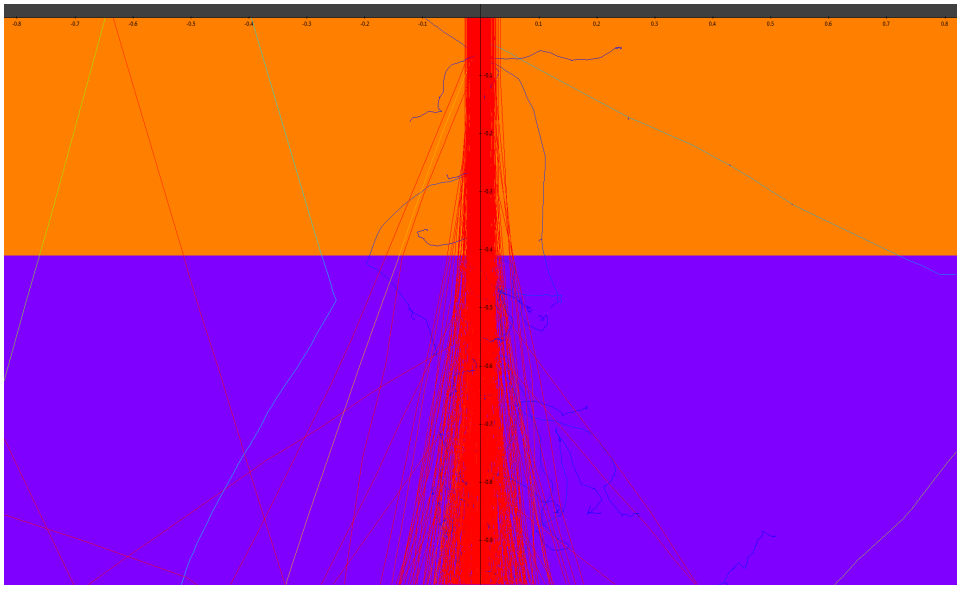

Figure B.19: Detailed view of the electron trajectories in the substrate boundary.

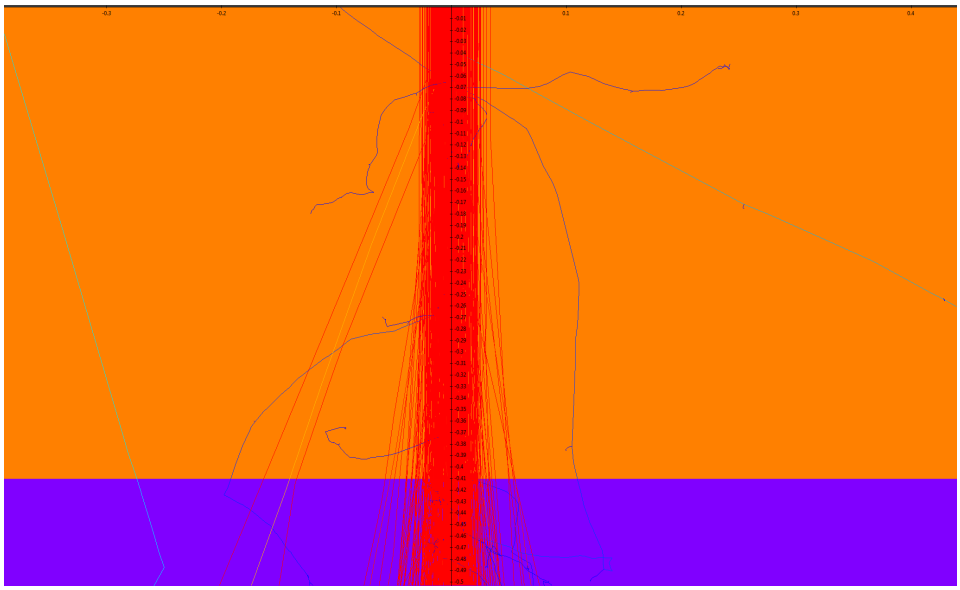

Figure B.20: Detailed view of the forward scattering effects in the resist layer.

B.1.6 410nm PMMA using 100pA Beam Current and 25kV

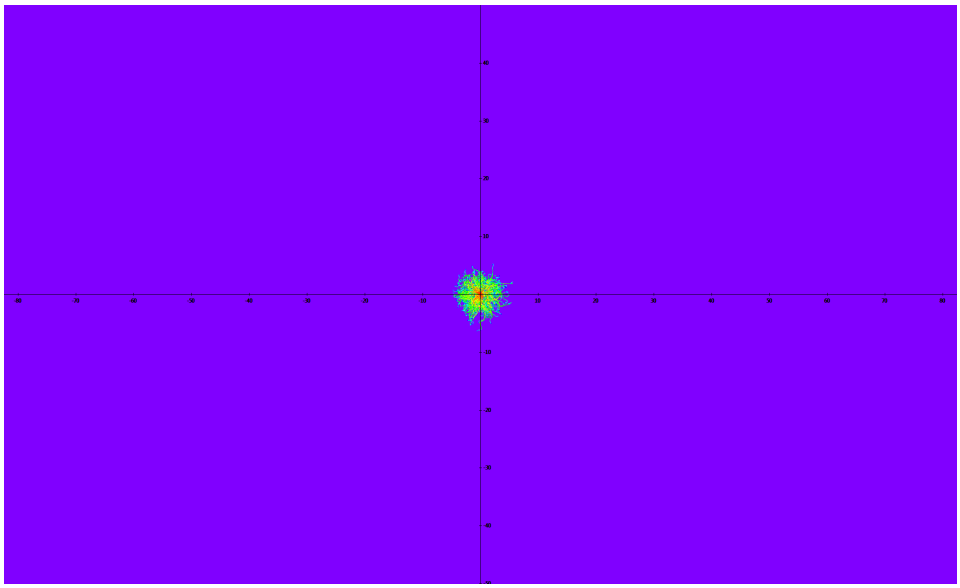

Figure B.21: Top view of the electron trajectories.

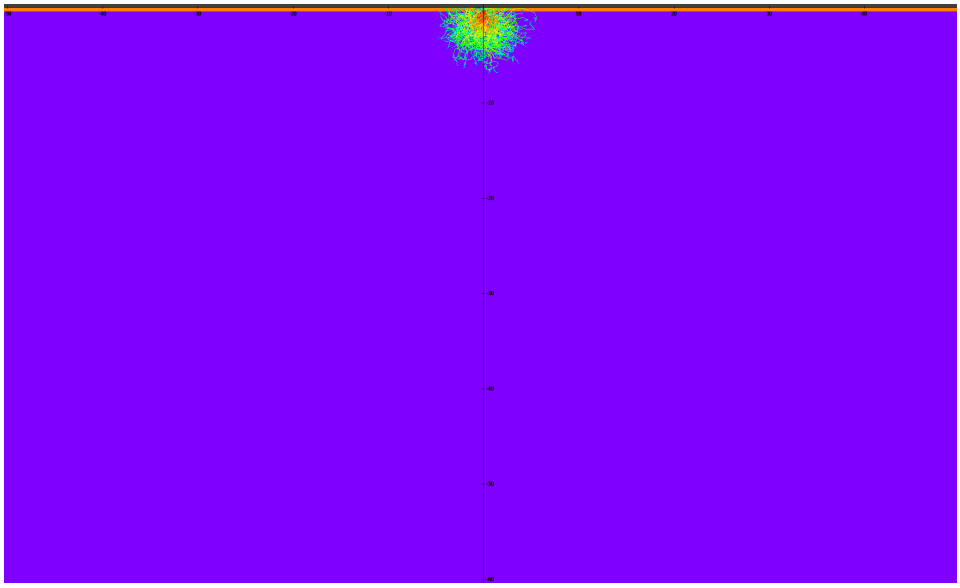

Figure B.22: Side view of the electron trajectories.

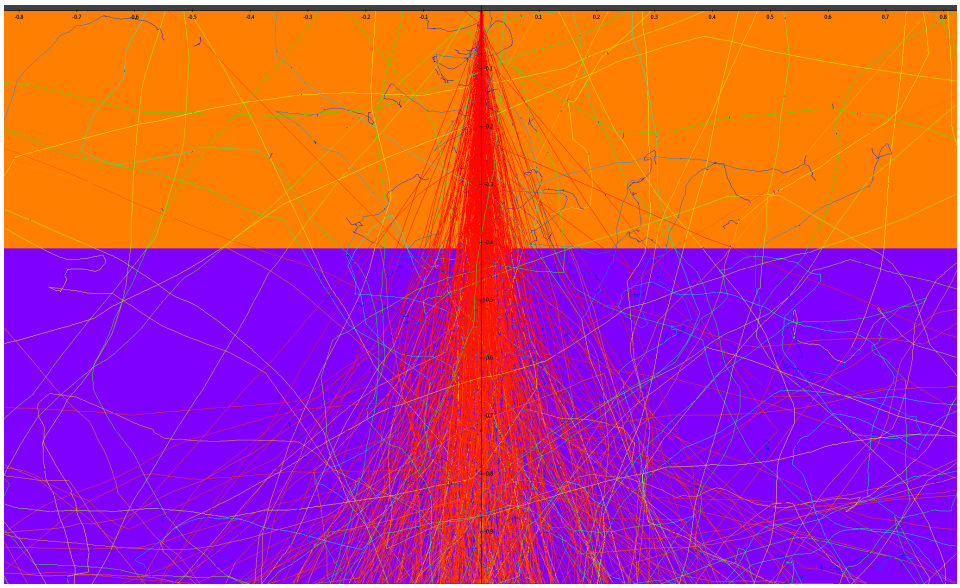

Figure B.23: Detailed view of the electron trajectories in the substrate boundary.

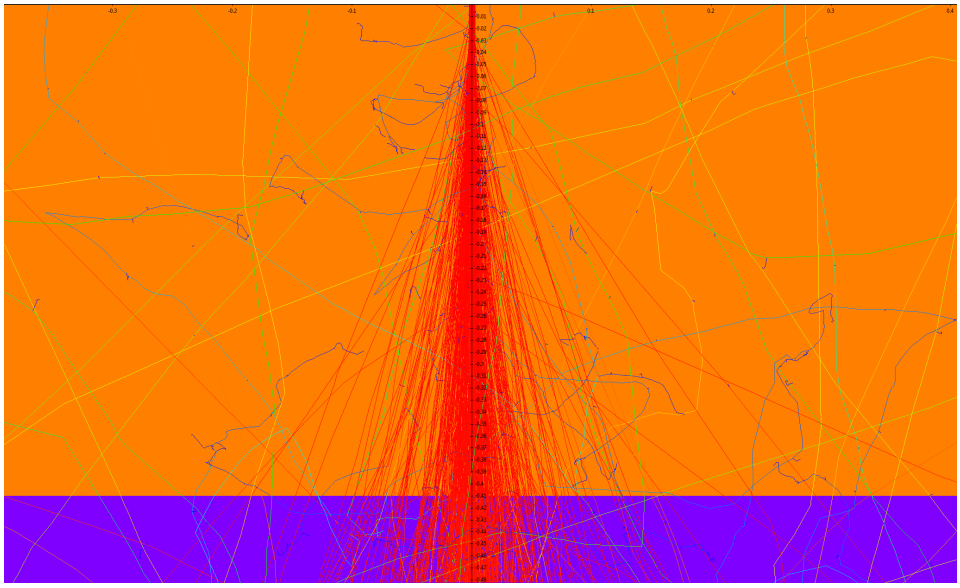

Figure B.24: Detailed view of the forward scattering effects in the resist layer.

Appendix C

Receipe Iterations

C.1 Receipe 1

1. Cleaning of 2" Silicon Wafer
    - Acetone, rinse.
    - Ethanol, rinse.
    - Isopropanol, rinse.
    - DI Water, rinse.
    - Dry with N_2 gas until droplets are no longer visible.
    - Plasma cleaner, O_2 gas, 50/50, 2 min.
2. Soft bake on hot plate, 180°C, 3 min.
3. Spin coating of EBL resist - CSAR62
    - TK rpm - TK sec - TK rpm/sec.
    - TK rpm - TK sec - TK rpm/sec.
4. Bake on hot plate, 150°C, 1 min.
5. EBL Exposure, RTD layer.
    - Beam Current: 5 nA

6. Development
    - 1 min soak in developer TK
    - 10 sec dip in MIBK:IPA
    - 1 min soak in IPA
    - Dry with N_2 gas until droplets are no longer visible.
7. e-beam deposition of Ti adhesion layer.
    - Final thickness: 10 nm.
    - Deposition rate: 5 Å/s.
8. e-beam deposition of Pt layer.
    - Final thickness: 40 nm.
    - Deposition rate: 5 Å/s.
9. Lift-off
    - Soak in EBL resist stripper, TK until all remaining resist is disolved.
    - Rinse with acetone.
    - Rinse with ethanol.
    - Rinse with IPA.
    - Rinse with DI Water.
    - Dry with N_2 gas until droplet are no longer visible.
10. Spin coating of EBL resist - CSAR62
    - TK rpm
    - TK rpm
11. Bake on hot plate, 150°C, 3 min.
12. EBL Exposure, Lead Wires and Bond Pads.

13. Development
    - 1 min soak in developer TK.
    - 10 sec dip in MIBK:IPA.
    - 1 min soak in IPA.
    - Rinse with DI Water.
    - Dry with N_2 gas until droplets are no longer visible.
14. e-beam deposition of Ti adhesion layer.
    - Final Thickness: 10 nm.
    - Deposition Rate: 5 Å/s.
15. e-beam deposition of Au layer.
    - Final Thickness: 100 nm.
    - Deposition rate: 5 Å/s.
16. Lift-Off
    - Soak in EBL resist stripper, TK until all remaining resist is disolved.
    - Rinse with acetone.
    - Rinse with ethanol.
    - Rinse with IPA.
    - Rinse with DI Water.
    - Dry with N_2 gas until droplet are no longer visible.

C.2 Receipe 2

1. Cleaning of 2" Silicon Wafer
    - Acetone, soak for 5 min.
    - Ethanol, soak for 5 min.
    - Isopropanol, rinse.
    - DI Water, rinse.
    - Dry with N_2 gas until droplets are no longer visible.
    - Plasma cleaner, O_2 gas, 50/50, 3 min.
2. Soft bake on hot plate, 180°C, 3 min.
3. Spin coating of EBL resist - CSAR62
    - TK rpm - TK sec - TK rpm/sec.
    - TK rpm - TK sec - TK rpm/sec.
4. Bake on hot plate, 150°C, 3 min.
5. EBL Exposure, RTD layer.
    - Beam Current: 5 nA
6. Development
    - 1 min soak in developer TK
    - 10 sec dip in MIBK:IPA
    - 1 min soak in IPA
    - Dry with N_2 gas until droplets are no longer visible.
7. e-beam deposition of Ti adhesion layer.
    - Final thickness: 10 nm.
    - Deposition rate: 5 Å/s.
8. e-beam deposition of Pt layer.
    - Final thickness: 40 nm.
    - Deposition rate: 5 Å/s.

9. Lift-off
    - Soak in EBL resist stripper, TK until all remaining resist is disolved.
    - Rinse with acetone.
    - Rinse with ethanol.
    - Rinse with IPA.
    - Rinse with DI Water.
    - Dry with N_2 gas until droplet are no longer visible.
10. Spin coating of EBL resist - CSAR62
    - TK rpm
    - TK rpm
11. Bake on hot plate, 150°C, 3 min.
12. EBL Exposure, Lead Wires and Bond Pads.
13. Development
    - 1 min soak in developer TK.
    - 10 sec dip in MIBK:IPA.
    - 1 min soak in IPA.
    - Rinse with DI Water.
    - Dry with N_2 gas until droplets are no longer visible.
14. e-beam deposition of Ti adhesion layer.
    - Final Thickness: 10 nm.
    - Deposition Rate: 5 Å/s.

15. e-beam deposition of Au layer.
    - Final Thickness: 100 nm.
    - Deposition rate: 5 Å/s.
16. Lift-Off
    - Soak in EBL resist stripper, TK until all remaining resist is disolved.
    - Rinse with acetone.
    - Rinse with ethanol.
    - Rinse with IPA.
    - Rinse with DI Water.
    - Dry with N_2 gas until droplet are no longer visible.

C.3 Receipe 3

1. Cleaning of 2" Silicon Wafer
    - Acetone, soak for 5 min.
    - Ethanol, soak for 5 min.
    - Isopropanol, rinse.
    - DI Water, rinse.
    - Dry with N_2 gas until droplets are no longer visible.
    - Plasma cleaner, O_2 gas, 50/50, 3 min.
2. Soft bake on hot plate, 180°C, 3 min.
3. Spin coating of EBL resist - CSAR62
    - TK rpm - TK sec - TK rpm/sec.
    - TK rpm - TK sec - TK rpm/sec.
4. Bake on hot plate, 150°C, 3 min.
5. EBL Exposure, RTD layer.
    - Beam Current: 5 nA
6. Development
    - 1 min soak in developer TK
    - 10 sec dip in MIBK:IPA
    - 1 min soak in IPA
    - Dry with N_2 gas until droplets are no longer visible.
7. e-beam deposition of Ti adhesion layer.
    - Final thickness: 10 nm.
    - Deposition rate: 5 Å/s.
8. e-beam deposition of Pt layer.
    - Final thickness: 60 nm.
    - Deposition rate: 5 Å/s.

9. Lift-off
    - Soak in EBL resist stripper, TK until all remaining resist is disolved.
    - Rinse with acetone.
    - Rinse with ethanol.
    - Rinse with IPA.
    - Rinse with DI Water.
    - Dry with N_2 gas until droplet are no longer visible.
10. Spin coating of EBL resist - CSAR62
    - TK rpm
    - TK rpm
11. Bake on hot plate, 150°C, 3 min.
12. EBL Exposure, Lead Wires and Bond Pads.
13. Development
    - 1 min soak in developer TK.
    - 10 sec dip in MIBK:IPA.
    - 1 min soak in IPA.
    - Rinse with DI Water.
    - Dry with N_2 gas until droplets are no longer visible.
14. e-beam deposition of Ti adhesion layer.
    - Final Thickness: 10 nm.
    - Deposition Rate: 5 Å/s.

15. e-beam deposition of Au layer.
    - Final Thickness: 100 nm.
    - Deposition rate: 5 Å/s.
16. Lift-Off
    - Soak in EBL resist stripper, TK until all remaining resist is disolved.
    - Rinse with acetone.
    - Rinse with ethanol.
    - Rinse with IPA.
    - Rinse with DI Water.
    - Dry with N_2 gas until droplet are no longer visible.

Appendix D

Design and Drawings of Wafer Test Stage

In order to test the RTD's produced, they need to be connected with an external circuit. The bond pads, as presented in Chapter 6, are only 1 mm^2, and the most common way for a connection is to permanently bond the RTD circuit by wire bonding.

Two issues with this approach is summarized here:

1. Wire bonding is time consuming and tedious work, demanding many hours from an experienced person for successful connections.

2. The wire bonds are permanent, and would inhibit conventional storage of the wafers for future testing of operability measures such as drift and hysteresis, if not inhibit the retesting by destruction of the connection points.

To completely eliminate the need for wire bonding, a wafer test stage has been designed and fabricated using a 3D printer. The stage consists of a tray where the wafer is placed, and a lid, where pogo pins are mounted. Pogo pins are spring loaded electrical conductors, specifically used for connecting iC circuits.

D.1 Results: Wafer Test Stage – Lid

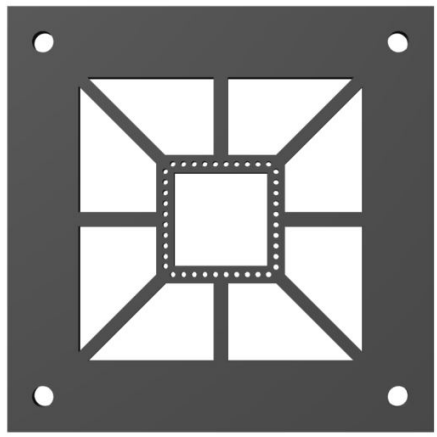

(a)

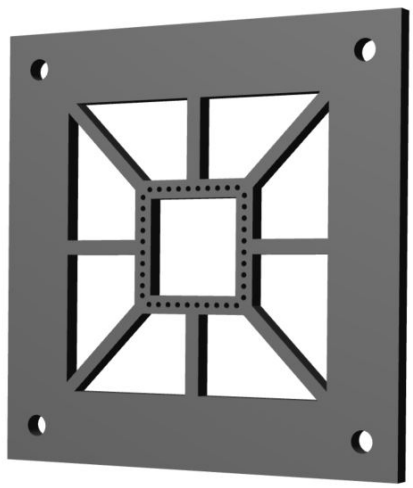

(b)

Figure D.1: Lid of wafer test stage. Integrated holes dedicated for pogo pin placements.

D.2 Results: Wafer Test Stage – Tray

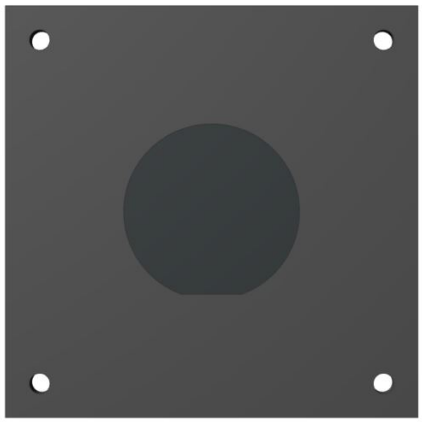

(a)

(b)

D.3 Technical Drawings: Lid

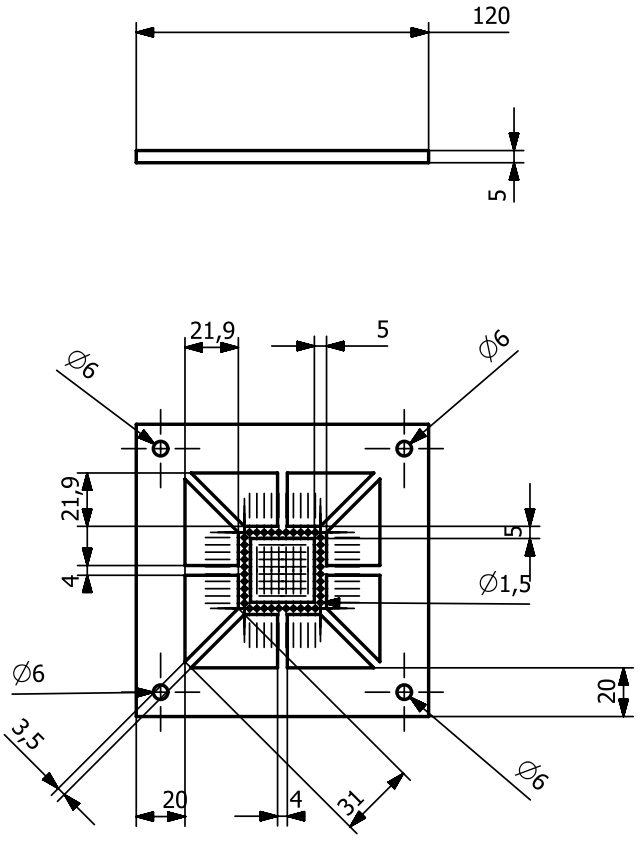

Figure D.3: Technical drawings – lid.

D.4 Technical Drawings: Tray

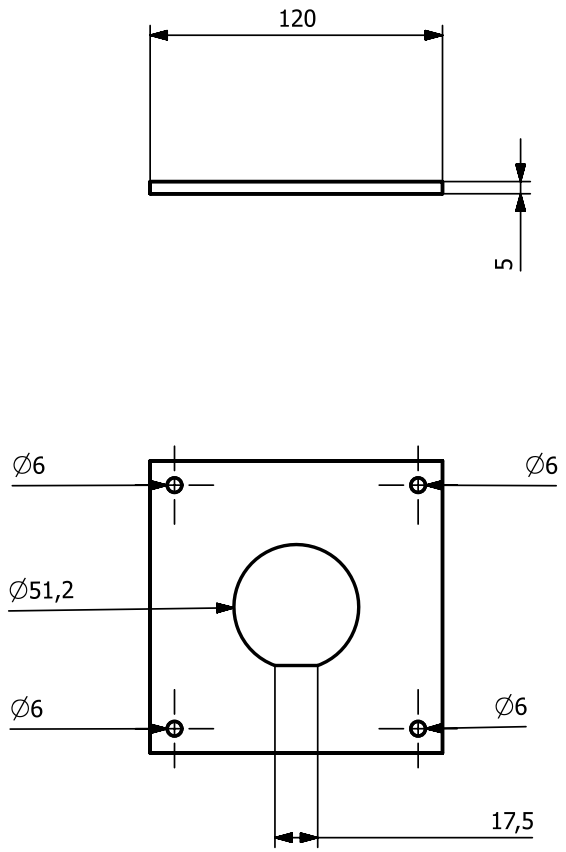

Figure D.4: Technical drawings – tray.

Appendix E

Resistance – Temperature of Ni, Cu and Pt

Platinum [34]

$$R(t) = R_0(1 + At + Bt^2 + C(t - 100)t^3) \tag{E.1}$$

$$R(t) = R_0(1 + \alpha t) \tag{E.2}$$

Copper [34]

$$R(t) = R_0(1 + \alpha t) \tag{E.3}$$

Nickel [34]

$$R(t) = R_0(1 + At + Bt^2 + Ct^4) \tag{E.4}$$

Table E.1: Tabulated values [34]. For platinum A[$\times 10^{-3\circ}C^{-1}$], B[$\times 10^{-7\circ}C^{-7}$] and C[$\times 10^{-12\circ}C^{-4}$], and C becomes zero for t>0°C. For Nickel A[$\times 10^{-3\circ}C^{-1}$], B[$\times 10^{-6\circ}C^{-2}$] and C[$\times 10^{-11\circ}C^{-4}$]. α [$\times 10^{-3\circ}C^{-1}$].

Material	Range [$^\circ C$]	A	B	C	α
Platinum	-260 – 960	3.985	-5.85	4.27	3.927
Copper	-80 – 260	-	-	-	4.27
Nickel	-60 – 180	5.45	6.65	2.605	6.18